DISSERTATION

A FOURTH-ORDER FINITE VOLUME ALGORITHM WITH ADAPTIVE MESH REFINEMENT IN SPACE AND TIME FOR MULTI-FLUID PLASMA MODELING

Submitted by

Scott E. Polak

Department of Mechanical Engineering

In partial fulfillment of the requirements

For the Degree of Doctor of Philosophy

Colorado State University

Fort Collins, Colorado

Spring 2022

Doctoral Committee:

Advisor: Xinfeng Gao

Stephen Guzik
Fernando Tomasel
Debojyoti Ghosh
Wolfgang Bangerth

ABSTRACT

A FOURTH-ORDER FINITE VOLUME ALGORITHM WITH ADAPTIVE MESH REFINEMENT IN SPACE AND TIME FOR MULTI-FLUID PLASMA MODELING

Improving our fundamental understanding of plasma physics using numerical methods is pivotal to the advancement of science and the continual development of cutting-edge technologies such as nuclear fusion reactions for energy production or the manufacturing of microelectronic devices. An elaborate and accurate approach to modeling plasmas using computational fluid dynamics (CFD) is the multi-fluid method, where the full set of fluid mechanics equations are solved for each species in the plasma simultaneously with Maxwell's equations in a coupled fashion. Nevertheless, multi-fluid plasma modeling is inherently multiscale and multiphysics, presenting significant numerical and mathematical stiffness. This research aims to develop an efficient and accurate multi-fluid plasma model using higher-order, finite-volume, solution-adaptive numerical methods. The algorithm developed herein is verified to be fourth-order accurate for electromagnetic simulations as well as those involving fully-coupled, multi-fluid plasma physics. The solutions to common plasma test problems obtained by the algorithm are validated against exact solutions and results from literature. The algorithm is shown to be robust and stable in the presence of complex solution topology and discontinuities, such as shocks and steep gradients. The optimizations in spatial discretization provided by the fourth-order algorithm and adaptive mesh refinement are demonstrated to improve the solution time by a factor of 10 compared to lower-order methods on fixed-grid meshes. This research produces an advanced, multi-fluid plasma modeling framework which allows for studying complex, realistic plasmas involving collisions and practical geometries.

ACKNOWLEDGEMENTS

I am very thankful to everyone who has served on my committee, both in the present and past: Dr. Gao, Dr. Guzik, Dr. Tomasel, Dr. Ghosh, Dr. Bangerth, Dr. Estep, and Dr. Williams. Your feedback and guidance have been invaluable. I have always wanted to pursue a PhD. There were various motivating factors that accumulated over the years, but I think Fernando's encouragement was the straw that finally broke my vacillating camel's back. I especially want to thank my advisor, Dr. Gao. Your classes on Computational Gas Dynamics were not only enlightening, but they also led to me joining the CFD and Propulsion Lab and provided the foundation I needed for my research. You have been unwavering in your support and encouragement, and I am very grateful for your understanding of my unique situation. I only hope my hectic schedule didn't interfere too much with *your* hectic schedule! I also want to thank all my colleagues in the CFD and Propulsion lab. I can say with confidence that I took more than I gave when it came to the exchange of knowledge within our group. It's a shame our schedules were interrupted by a pandemic the last couple years, because I enjoyed being on-site, in the lab, working with you all.

Throughout my career, various colleagues have referred to me as "Dr. Polak," despite the fact that I hadn't yet earned a doctorate degree. I think this title was given to me because of the effort and passion I tend to apply to my work. I suppose it's an accurate appellation, because it certainly takes an astounding effort to earn a PhD. Another thing I know for certain is that graduate school required even more effort at this point in my life than it would have before I had children and a career. To be clear, I am not more assiduous or capable now than I was in my 20's; instead, someone helped me make up the difference, kept our family happy and healthy, preserved my sanity and motivation, and "held down the fort." I share the achievement of this PhD with my hard-working, caring, and supportive wife, Rian. Thank you for your encouragement and help - I love you! To my parents, you have obviously bestowed upon me an appreciation for higher-education and the work-ethic to achieve it, and I am beholden to you for that gift. As a parent myself now, I realize how challenging

that is. Thank you to all the folks at Advanced Energy who have advocated and accommodated my academic pursuit. Finally, thank you to all my friends and family who supported me on this journey.

DEDICATION

To my children, Olivia and Hugh. I hope this work benefits everyone at some point, but most importantly, I hope it inspires you to embrace challenge and learning. Everything is attainable with hard work and perseverance. Don't fear the circuitous path; often the farther you stray from convenience and comfort, the bigger the reward.

TABLE OF CONTENTS

ABSTRACT ii
ACKNOWLEDGEMENTS iii
DEDICATION v
LIST OF TABLES viii
LIST OF FIGURES ix
LIST OF SYMBOLS xiv

Chapter 1 Introduction 1
1.1 Motivation 1
1.2 Models of Plasma 3
1.2.1 Kinetic Models 4
1.2.2 Fluid-Based Models 5
1.3 Objectives 9
1.4 Dissertation Organization 10

Chapter 2 The Multi-Fluid Plasma Model 11
2.1 Fluid Equations 11
2.2 Electromagnetic Equations 14
2.2.1 Classical Form 14
2.2.2 Hyperbolic-Only Formulation 14
2.3 Model Closure 15
2.3.1 Coupling of the Fluid and Electromagnetic Equations 16
2.3.2 Collisions 16
2.3.3 Equation of State 19

Chapter 3 Numerical Method 20
3.1 Conservative Form of the Governing Equations 20
3.2 Higher-Order Reconstruction 21
3.3 Flux Evaluation 23
3.3.1 Convolution and Deconvolution 23
3.3.2 Riemann Solvers 24
3.4 Boundary Conditions 27
3.4.1 Zero-Gradient 27
3.4.2 Perfect Electrical Conductor 27
3.4.3 Silver-Müller Absorbing Boundary Condition 29
3.5 Time Marching Method 29
3.6 Adaptive Mesh Refinement 30
3.7 Solution-Stabilizing Methods 32
3.7.1 Artificial Viscosity 33
3.7.2 High-Order Adaptive Clipping-and-Redistribution 33
3.7.3 Face Value Limiting 34

3.7.4 Face Construction Order Reduction . . . 35

Chapter 4 Verification . . . 36
4.1 Three Dimensional Plane-Polarized Electromagnetic Wave in Vacuum . . . 36
4.2 1D Electron Acoustic Wave, One-Harmonic . . . 40

Chapter 5 Validation . . . 45
5.1 Axisymmetric Plasma Kernel Expansion . . . 45
5.1.1 Axisymmetric Governing Equations . . . 46
5.1.2 Boundary Conditions and Initialization . . . 48
5.1.3 Transport and Thermodynamic Properties . . . 49
5.1.4 Solution Methodology . . . 51
5.1.5 Results and Discussion . . . 52
5.2 2D Transmagnetic Wave . . . 56
5.3 1D Electron Acoustic Wave, 10-Harmonics . . . 59

Chapter 6 Simulation Results and Discussion . . . 60
6.1 Refractive Scattering of an Electromagnetic Pulse . . . 60
6.1.1 Problem Setup . . . 60
6.1.2 Results and Discussion . . . 61
6.2 1D Magnetic Shock Tube . . . 64
6.2.1 Problem Setup . . . 64
6.2.2 Results and Discussion . . . 65
6.3 GEM Challenge Magnetic Reconnection Problem . . . 74
6.3.1 Nondimensionalization . . . 74
6.3.2 Domain & Boundary Conditions . . . 74
6.3.3 Initial Conditions . . . 74
6.3.4 Model Parameters . . . 77
6.3.5 Results and Discussion . . . 78
6.4 Plasma Blast Explosion . . . 86
6.4.1 Computational Configurations . . . 86
6.4.2 Model Parameters . . . 88
6.4.3 Results and Discussion . . . 88

Chapter 7 Conclusions and Future Work . . . 100
7.1 Conclusions . . . 100
7.2 Original Contributions . . . 101
7.3 Future Work . . . 101

Appendix A Numerical Algorithm Data Structure . . . 113
A.1 Conservation Equation Terms, Multi-Fluid Plasma Model . . . 114

LIST OF TABLES

4.1 L_p norms (where $p = 1, 2, \infty$) of the electromagnetic solution errors for the 3D plane-polarized electromagnetic wave test case at time 1.2 ns. The convergence rates are computed between consecutive grid resolutions, demonstrating the 4th-order accuracy of the algorithm. 39
4.2 L_p norms (where $p = 1, 2, \infty$) of pertinent solution errors for the single-harmonic electron acoustic wave test case at time 3. The convergence rates are computed between consecutive grid resolutions, demonstrating the 4th-order accuracy of the algorithm. . . 43

6.1 Comparing the computational efficiency of various solution methods in Chord. All rows represent minimum grids required for an accurate solution to the magnetic shock tube problem with $m_i = 1$. The simulations are run to a partial solution time of $t = 0.4$ to avoid interaction with the boundaries, for reasons discussed earlier. All cases are run with the same CFL number, 0.82. The AMR solutions use refinement criteria based on electron density relative gradients with a threshold of 0.01. The values reported in the Compute Time column represent normalized wall clock times for each solution. The absolute values of computational CPU-hours aren't currently germane because the algorithm has not yet been compiled in an optimized, production environment. 67
6.2 Comparing the computational efficiency of various solution methods by Chord. The simulations are run to a partial solution time of $t = 0.4$. All cases are run with the same CFL number, 0.4. The AMR solutions use refinement criteria based on relative gradients of the electron and ion energy densities, with a threshold of 0.5. The values reported in the Compute Time column represent normalized wall clock times for each solution. The absolute values of computational CPU-hours are not currently apropos because the algorithm has not yet been compiled in an optimized, production environment. 93

LIST OF FIGURES

3.1 Illustration of a finite-volume method on a 2D Cartesian control volume 22
3.2 Riemann fan diagram for the HLLC metohd 25
3.3 Illustration of adaptive mesh refinement on a 2D Cartesian mesh. The labels Ω_0, Ω_1, and Ω_2 represent the progressively higher-resolution meshes, applied selectively to subsets of the domain. In this illustration, the refinement ratio between each level is 2. The boxes outlined in thicker black borders represent the decomposition of the domain into a disjoint union of boxes for parallel computing. The dashed lines represent ghost cells in which the values are interpolated from the coarser mesh. 32
3.4 Subcycling allows finer grids to be integrated in time using interpolated data from the next coarser grid to fill ghost cells at the AMR boundaries, indicated by the dashed gray lines. In this example, there are two levels of grid refinement, with a refinement ratio of 2 between each level; thus, the timestep is halved as each successfully refined level is subcycled. 32
3.5 1D interpolation showing the HO-ACR method on Cartesian grids. The interpolation is 4th-order and conservative using a 5-point centered stencil. The x axis shows the coarse cells, and y axis the 4th-order cell-averaged values of the solution. Yellow lines indicate coarse solution values, green lines the coarse to fine interpolation, and blue lines the interpolation with addition of the HO-ACR method. Gray lines show the bounding envelope used by the HO-ACR method for non-smooth regions. 34

4.1 Three plane contour plot of variable E_z from the 3D electromagnetic wave test case, at time 1.2 ns. 37
4.2 Grid convergence rate of L_1, L_2, and L_∞ for variables E_z and B_z from the electromagnetic wave test case, at time 1.2 ns. 38
4.3 Electron acoustic wave problem, initial perturbation to the electron velocity for various numbers of odd harmonics, N 42
4.4 Grid convergence rate of L_1, L_2, and L_∞ for variables E_x and ρu_e from a 1-harmonic electron acoustic wave test case at a normalized time of 3. Reference lines with slopes of -4 and -5 are shown adjacent to the error plots to illustrate the 4th-order accurate convergence rate. The x-axis represents mesh size (cell count), M, for each solution. . 44

5.1 An illustration of the laser-initiated plasma kernel problem domain for the test case . . 46
5.2 Initial conditions for the high-energy laser-initiated plasma kernel. Spatial scaled is zoomed in relative to the problem domain. 49
5.3 Extrapolation model for ultra-high temperature transport properties 50
5.4 Extrapolation model for ultra-high temperature thermodynamic properties 51
5.5 Example of solution-adaptive mesh refinement, with tagging thresholds of 0.2 for both pressure and density and 5 levels of AMR. Contour plots show pressure at 0.1 $\mu\mathrm{s}$. Only one in four actual mesh lines are shown in subfigure (a) to enhance clarity in the figure. 53
5.6 Temporal evolution of high-energy kernel. Spatial scaled is zoomed in for temperature plot. 53

5.7 Simulation results at four steps. Spatial scale is zoomed in for temperature plots. . . . 54
5.8 Comparing thermodynamic kernel evolution between the current work and results from literature 55
5.9 Transverse magnetic wave solution for scalar electric field E_z with $m = 8$ and $n = 5$, at solution time 75 ns on a 64×32 mesh. 57
5.10 Comparison of numerical results for the TM wave calculation on a 64×32 mesh, with $m = 8$ and $n = 5$, at solution time 75 ns. Left plot shows E_z at $y = 20$ m and right plot shows E_z at $x = 25$ m. The numerical results (black marks) show good agreement with the exact solution (solid lines). 58
5.11 Transverse magnetic wave solution for magnetic field $\vec{B}$ with $m = 8$ and $n = 5$, at solution time 75 ns on a 64×32 mesh. 58
5.12 Electron acoustic wave results, 10-harmonic case, at a normalized time of 3. The solution from Chord (lighter markers) is compared to the exact solution (darker, solid line). The plot on the left shows electron velocity and the plot on the right shows the x-component of the electric field. The Chord solution is using a 4th-order accurate algorithm with a fixed mesh size of 1024. The marker density for the Chord solution has been reduced by a factor of 1/4 to improve clarity. 59

6.1 Initialization of the z component of the magnetic field, B_z. Units are in T or $\mathrm{kg\,A^{-1}\,s^{-2}}$. A circle is superimposed on the plot to illustrate the refractive disk in the middle of the domain, with permittivity as defined by Equation (6.1). The initial mesh is shown, with refinement triggered by the amplitude of the B_z term. 62
6.2 Results from a Gaussian-tapered, electromagnetic pulse incident on a refractive disk, at various times as indicated (in units of ns). The left column of plots show the magnitude of the magnetic field in units of T or $\mathrm{kg\,A^{-1}\,s^{-2}}$, and the right column shows the magnitude of the divergence correction potential, Φ, also in units of T or $\mathrm{kg\,A^{-1}\,s^{-2}}$. . 63
6.3 Magnetic shock tube results at a normalized time of 0.2 for $m_i = 1$. The solutions from Chord (lighter markers) are compared to the reference solution (darker, dashed line). For these simulations, the speed of light was set to $c = 2$ in order to match the settings of the reference solution. Results are shown for both the 2nd-order and 4th-order accurate algorithms in Chord. The reference solution is 2nd-order. All solutions use a fixed grid, with grid spacing as specified in the legend. 68
6.4 Magnetic shock tube results at a normalized time of 0.2 for $m_i = 1$ and $c = 2$. The solution from Chord (lighter, circular markers) is compared to the reference solution (darker, dashed line). The reference solution uses a fixed mesh spacing of 1.0×10^{-4}. The Chord solution uses AMR with 3 levels of refinement and a coarse mesh spacing of 1×10^{-3}. Mesh refinement was determined based on the relative gradient values of the electron density, ρ_e, with a gradient threshold of 0.005. The adaptive mesh spacing in Chord is displayed on the plot as thin, vertical lines (the mesh line density has been reduced by a factor of $1/8$ to improve clarity). 69

6.5 Magnetic shock tube results at a normalized time of 10 for $m_i = 1$. The solution from Chord (lighter, solid line) is compared to the reference solution (darker, dashed line). The reference solution uses a fixed mesh spacing of 1.0×10^{-4}. The Chord solution uses AMR with 3 levels of refinement and a coarse mesh spacing of 3.9×10^{-3}. Mesh refinement was determined based on the relative gradient values of the electron density, ρ_e, with a gradient threshold of 0.005. The adaptive mesh spacing in Chord is displayed on the plot as thin, vertical lines (the mesh line density has been reduced by a factor of $1/8$ to improve clarity). 70
6.6 Magnetic shock tube results at a normalized time of 10 for $m_i = 1 \times 10^{-1}$. The solution from Chord (lighter, solid line) is compared to the reference solution (darker, dashed line). The reference solution uses a fixed mesh spacing of 1.0×10^{-4}. The Chord solution uses AMR with 3 levels of refinement and a coarse mesh spacing of 1.9×10^{-3}. Mesh refinement was determined based on the relative gradient values of the electron density, ρ_e, with a gradient threshold of 0.002. The adaptive mesh spacing in Chord is displayed on the plot as thin, vertical lines (the mesh line density has been reduced by a factor of $1/16$ to improve clarity). 71
6.7 Magnetic shock tube results at a normalized time of 10 for $m_i = 1 \times 10^{-3}$. The solution from Chord (lighter, solid line) is compared to the reference solution (darker, dashed line). The reference solution uses a fixed mesh spacing of 1.0×10^{-4}. The Chord solution uses AMR with 2 levels of refinement and a coarse mesh spacing of 2.4×10^{-4}. Mesh refinement was determined based on the relative gradient values of the electron density, ρ_e, with a gradient threshold of 0.002. The adaptive mesh spacing in Chord is displayed on the plot as thin, vertical lines (the mesh line density has been reduced by a factor of $1/48$ to improve clarity). 72
6.8 Magnetic shock tube results at a normalized time of 10 for $m_i = 1 \times 10^{-3}$. The solution from Chord is compared for four different mesh resolutions. Two levels of AMR refinement are used in all cases. Mesh refinement was determined based on the relative gradient values of the electron density, ρ_e, with a gradient threshold of 0.002. In all four cases, the plasma (electron) frequency drives the maximum time step, so the same time step value of $\Delta t = 2.5 \times 10^{-5}$ is used in each case. 73
6.9 Electron density, ρ_e, at $t = 5$, for the case without the HO-ACR algorithm and without FCOR. We see subtle oscillations beginning to develop near the center of the domain, originating at the horizontal boundary between the finest and next finest mesh patches; this is in contrast to the plot in Figure 6.10. The mesh shown here on half of the contour plot has been drawn with a $4\times$ reduced resolution, to improve clarity. On the right is a plot of ρ_e taken from a vertical line through the center of the domain, $x = 4\pi$. 79
6.10 Electron density, ρ_e, at $t = 5$, for the case with the HO-ACR algorithm and with FCOR. No unexpected oscillations are present and the solution evolution is stable. The mesh shown here on half of the contour plot has been drawn with a $4\times$ reduced resolution, to improve clarity. On the right is a plot of ρ_e taken from a vertical line through the center of the domain, $x = 4\pi$. 79

6.11 Electron density, ρ_e, at $t = 10$, for the case without the HO-ACR algorithm and without FCOR. The oscillations which were first noticed in Figure 6.9 have started to propagate, corrupting the solution away from the AMR boundaries; this is in contrast to the plot in Figure 6.12. The mesh shown here on half of the contour plot has been drawn with a $4\times$ reduced resolution, to improve clarity. On the right is a plot of ρ_e taken from a vertical line through the center of the domain, $x = 4\pi$. 80
6.12 Electron density, ρ_e, at $t = 10$, for the case with the HO-ACR algorithm and with FCOR. The solution continues to evolve without unexpected oscillations. The mesh shown here on half of the contour plot has been drawn with a $4\times$ reduced resolution, to improve clarity. On the right is a plot of ρ_e taken from a vertical line through the center of the domain, $x = 4\pi$. 80
6.13 Electron density, ρ_e, at $t = 15$, for the case without the HO-ACR algorithm and without FCOR. The oscillations in electron density have destabilized the solution, affecting other solution variables. The solution does not progress much further in time than this, eventually diverging. Clearly the numerical-stabilizing methods are required for this problem, as demonstrated in Figure 6.14. The mesh shown here on half of the contour plot has been drawn with a $4\times$ reduced resolution, to improve clarity. On the right is a plot of ρ_e taken from a vertical line through the center of the domain, $x = 4\pi$. 81
6.14 Electron density, ρ_e, at $t = 15$, for the case with the HO-ACR algorithm and with FCOR. The solution continues to evolve without unexpected oscillations. The mesh shown here on half of the contour plot has been drawn with a $4\times$ reduced resolution, to improve clarity. On the right is a plot of ρ_e taken from a vertical line through the center of the domain, $x = 4\pi$. 81
6.15 The solution evolution in time is shown for the case with the HO-ACR and FCOR algorithms enabled. This simulation uses two levels of AMR and a coarse grid of 144×72, with tagging based on the electron energy density, $\rho_e e_e$. The left column shows the ion density, ρ_i, and the magnetic field magnitude $|\vec{B}|$ is shown on the right. 83
6.16 Reconnected magnetic flux vs. time for the GEM Challenge case. For reference, the full particle and classical, single-fluid MHD solutions from the original GEM challenge publication are presented. The Chord solutions agree well with the full particle solution. As anticipated, there is little difference in reconnected magnetic flux between the fixed-grid and AMR solutions in Chord. 84
6.17 Chord solutions to the GEM reconnection problem, comparing the solution obtained with AMR (left column) to that with a fixed, uniform mesh (right column). The plots show nondimensionalized ion mass density ρ_i at various solution times. The AMR solution uses a coarse grid size of 144×72 cells with two levels of adaptive refinement and a refinement ratio of 2. The fixed mesh solution uses a grid size of 576×288. Both solutions use identical CFL numbers. The mesh at each time step is superimposed on the right half of each plot, and the mesh resolution is reduced by a factor of 4 for visualization clarity. The AMR solution uses refinement tagging based on the relative gradient of the electron energy density $\rho_e e_e$. 85

6.18 Plasma explosion results. The left column uses a mass ratio of $m_i/m_e = 1$ and is used to validate the Chord solution against the reference solution. The right column uses a dissimilar mass ratio of $m_i/m_e = 25$ and highlights some of the enhanced detail and fidelity afforded by the multi-fluid plasma model, compared to a traditional, single-fluid MHD model. Both simulations use uniform grids of 160×160 cells and a time step of $\Delta t = 5 \times 10^{-4}$. 90
6.19 Comparing the mesh convergence trends between the second-order and fourth-order spatial reconstruction algorithms by Chord. The left two columns show total mass density, and the right two show total fluid pressure. 92
6.20 Comparing the mesh convergence trends between the second-order and fourth-order spatial reconstruction algorithms by Chord. The data shown in these plots is extracted from a diagonal section through the solution domain between points $(0, 0)$ and (L_x, L_y). The top two plots show total mass density ($\rho_i + \rho_e$), and the bottom two show total fluid pressure ($p_i + p_e$). 94
6.21 Total fluid density, $\rho_i + \rho_e$. Comparing the results of the solution with AMR (left column) with the solution on a uniform-grid mesh of 640×640 (right column) at various times shown. Both solutions use a fixed time step and the same CFL number based on the electromagnetic wave propagation speed. The AMR solutions use refinement criteria based on relative gradients of the electron and ion energy densities, with a threshold of 0.5. The mesh is shown on the right side of the domain in each plot, but the mesh resolution is reduced by a factor of $4\times$ to improve clarity. 95
6.22 Total fluid pressure, $p_i + p_e$. Comparing the results of the solution with AMR (left column) with the solution on a uniform-grid mesh of 640×640 (right column) at various times shown. Both solutions use a fixed time step and the same CFL number based on the electromagnetic wave propagation speed. The AMR solutions use refinement criteria based on relative gradients of the electron and ion energy densities, with a threshold of 0.5. The mesh is shown on the right side of the domain in each plot, but the mesh resolution is reduced by a factor of $4\times$ to improve clarity. 96
6.23 Magnetic pressure. Comparing the results of the solution with AMR (left column) with the solution on a uniform-grid mesh of 640×640 (right column) at various times shown. Both solutions use a fixed time step and the same CFL number based on the electromagnetic wave propagation speed. The AMR solutions use refinement criteria based on relative gradients of the electron and ion energy densities, with a threshold of 0.5. The mesh is shown on the right side of the domain in each plot, but the mesh resolution is reduced by a factor of $4\times$ to improve clarity. 97
6.24 Plots of the relative difference between the solution with AMR and the solution on a uniform-grid, at various times. The left column shows the relative difference in total mass density, and the relative difference in total fluid pressure is plotted on the right. Both solutions use a fixed time step and the same CFL number. The AMR solutions use refinement criteria based on relative gradients of the electron and ion energy densities, with a threshold of 0.5. The AMR mesh is shown on the right side of the domain in each plot, but the mesh resolution is reduced by a factor of $4\times$ to improve clarity. . . . 98
6.25 Plots of various electromagnetic parameters from the solution at $t = 0.4$ with AMR. . . 99

LIST OF SYMBOLS

For convenience, the more prevalent variables and symbols used throughout this dissertation are defined or described below.

N	number plasma species (fluids)
ρ_α	mass density of species α
n_α	number density of species α
m_α	particle mass of species α
q_α	particle charge of species α
$\rho_\alpha \vec{u}_\alpha$	flux vector of species α
$p_\alpha \vec{\vec{I}}$	static pressure tensor, species α
$\vec{\vec{\tau}}_\alpha$	viscous tensor, species α
p_α	scalar pressure, species α
$\rho_\alpha e_\alpha$	energy density, species α
$\vec{u}_\alpha$	average velocity, species α
$\vec{\phi}_\alpha$	heat flux vector, species α
t	time
$\vec{\vec{I}}$	identity tensor
∇	gradient operator
$\vec{\nabla}\cdot$	divergence operator
$\vec{\nabla}\times$	curl operator
$\vec{E}$	electric field
$\vec{B}$	magnetic field
$\vec{j}$	electric current density
ρ_q	electric charge density
ϵ_0	permittivity of free space
μ_0	permeability of free space

$\mathbf{U}$	vector of solution variables
$\vec{\mathbf{F}}$	inviscid flux dyad
$\vec{\mathbf{G}}$	viscous flux dyad
$\mathbf{S}$	vector of source terms

Chapter 1

Introduction

Plasma is the most common form of visible matter in the Universe. Throughout the cosmos, vast clouds of plasma form in the medium that exists between stars and galaxies. Nuclear fusion reactions within stars sustain hot, dense plasmas. Our planet is encircled by a region of dense, cold plasma within the magnetosphere. All modern electronic and micro-electromechanical devices are dependent on low-temperature, industrial plasmas and the nanometer-scale manufacturing processes they enable. And, in the near future, it is likely that magnetically-confined, high-temperature plasmas will enable nuclear fusion to become a sustainable, long-term source of energy and electricity on planet Earth. Yet, despite its prevalence, plasma is also the least understood state of matter.

1.1 Motivation

Often, plasma based technology is exceedingly complex and expensive; fusion reactors and semiconductor processing tools are two examples. In these situations, a trial and error or iterative approach to development is not time-efficient or economically viable. The ability to use computational methods to predict the characteristics of plasmas holds the potential to rapidly and cost-effectively converge upon an optimized solution of operating parameters or configurations of equipment. Indeed, advancing predictive method capabilities for plasma has been identified as one of the topics crucial to speeding advancements in low-temperature plasma science that so greatly benefits society[1]. However, the idiosyncrasies which make plasma so compelling and unique also confound its simulation.

Plasmas span nearly inconceivable ranges of densities, temperatures, and length scales. Clouds of interstellar plasma cover millions of light-years in length ($10^{22}\,\mathrm{m}$), and here on Earth, micro-arc plasmas created in labs are measured on the micron length scale ($10^{-6}\,\mathrm{m}$). The number densities of plasmas in the cores of stars and in confined fusion reactions can reach values of $10^{30}\,\mathrm{m}^{-3}$, while

some interstellar and magnetosphere plasmas have number densities as low as $10^3\,\mathrm{m}^{-3}$. Within this prodigious breadth, there is a surprisingly large collection of plasmas which adhere to the requirements of continuum mechanics, and models based on fluid mechanics are an effective method of simulating these plasmas.

The magnetohydrodynamics (MHD) approach is a common, fluid-based approximation of plasmas and has been studied extensively for more than half a century[2]. The classic, Ideal MHD model assumes that the plasma behaves as a single fluid, which simplifies the computations, but also fails to capture some of the more complex physics that occur in plasmas such as the Hall and diamagnetic effects. More complex formulations of MHD have been developed, including the resistive MHD and two fluid MHD methods[3], which increase the accuracy and complexity of the models. Another approach to modeling plasmas as fluids is the multi-fluid model, which is becoming increasingly popular in recent years as computing hardware improvements are enabling more complex algorithms. In the multi-fluid plasma model, each species within the plasma is modeled separately. The full set of fluid mechanics equations are solved for each fluid simultaneously along with the governing equations of electromagnetism (Maxwell's equations). The fluids interact with each other through collisions and with the electric and magnetic fields through source terms in the fluid and electromagnetic equations.

The complexity and increased physical accuracy of the multi-fluid approach further exacerbates the mathematical and numerical stiffness inherent in plasma simulations due to vast disparities in length and time scales. One technique in numerical modeling that very effectively mitigates stiffness is adaptive mesh refinement (AMR). AMR has been applied to MHD models of plasmas with great success[4–10]. However, there is currently a scarcity of research on applying AMR to the multi-fluid model; arguably where AMR would provide the most benefit.

In addition, the use of a high-order method can reduce the numerical error compared to a solution obtained using a low-order method with the same mesh resolution. Increasing the order of accuracy for a finite-volume algorithm is complex and requires more computations per time step compared to a lower-order method. However, this additional computational cost is offset by the

increase in computation per unit memory. Increasing the order of accuracy improves the accuracy per unit memory and makes better use of modern computer architectures. The present research is motivated by the development of an efficient and accurate numerical algorithm for multi-fluid plasma modeling.

1.2 Models of Plasma

Plasma is a state of matter, similar in some ways to a mixture of multiple gases, but plasmas are typically hotter than gases. In plasmas, each component of the mixture is referred to as a "species," much like in studies involving gaseous reactions or combustion. One of the defining properties of plasmas is that one or more of these species are comprised of electrically charged particles, such as electrons or ions. However, having clouds of charged particles does not alone define a plasma. To be considered a plasma, the charged particles must be close enough, spatially, that any one particle influences many nearby charged particles; this interaction is referred to as "collective behavior." The Debye length is a fundamental parameter of plasmas, and it is a function of the electron number density, n_e, and temperature, T_e,

$$\lambda_D = \left(\frac{\epsilon_0 k_B T_e}{q_e^2 n_e} \right)^{\frac{1}{2}}, \tag{1.1}$$

where ϵ_0 is the permittivity of free space, k_B is the Boltzmann constant, and q_e is the electron charge. A requirement for plasma to exhibit collective behavior is that the number of particles in a sphere with radius λ_D must be significantly greater than unity:

$$N_D \equiv n_e \frac{4\pi}{3} \lambda_D^3 \gg 1. \tag{1.2}$$

A plasma is also quasi-neutral, meaning it has approximately the same number of positively-charged as negatively-charged particles, thus a near-zero net charge (with the rare exception of non-neutral plasmas[11] created in laboratory settings). Quasi-neutrality occurs when the Debye length is much smaller than the plasma bulk geometry. Finally, the mean time between electron-

neutral collisions must be long compared to the oscillations of electron density within the plasma (commonly referred to as the plasma frequency). When selecting a model approach for plasma, one must consider the goals and limitations of the simulation — such as accuracy or computing resources — but also the physics of the problem.

The Knudsen number, $Kn = \lambda/L$, is a dimensionless parameter used to characterize a gaseous system. It is the ratio between the gas particle mean free path (λ) and a representative length scale of the system (L). The Knudsen number is used to determine whether a plasma can be modeled using a fluid-based method or if a kinetic (statistical) method is required. When the mean free path is on the same scale as or larger than the representative size of the plasma ($Kn \geq 1$), the particles in the system are unable to attain thermodynamic equilibrium and models of these plasmas require methods involving kinetic theory. However, when the mean free path is much smaller than the characteristic size of the system ($Kn \ll 1$), the particles in the plasma will experience sufficient collisions to reach a state near thermodynamic equilibrium. In these situations, the continuum assumptions are valid and the plasma can be modeled using a fluid-based method.

1.2.1 Kinetic Models

In general, models which account for particle positions and velocities in a plasma are referred to as kinetic models. While it is technically possible to compute the evolution of and interaction between individual particles, these types of models quickly become infeasible for any practical, macroscopic size domain, even on the most powerful computing hardware, where the number of particles $n \gg 10^{20}$. A popular compromise to a full particle model is a technique referred to as particle in cell (PIC), where many like-particles are lumped together in an attempt to reduce the total particle count without adversely changing the macroscopic properties of the plasma. As an alternative to particle models, a statistical accounting of the particles in the system can be considered, solving instead for the particles' distribution function. The fundamental equation describing the time-evolution of a plasma species distribution in 6-dimensional phase space ($\vec{x}, \vec{v}$) is the Boltz-

mann equation:

$$\frac{\partial f_\alpha}{\partial t} + \vec{v}_\alpha \cdot \vec{\nabla}_x f_\alpha + \frac{\vec{F}}{m_\alpha} \cdot \vec{\nabla}_v f_\alpha = \left(\frac{\partial f_\alpha}{\partial t}\right)_c, \tag{1.3}$$

where $f_\alpha(\vec{x}, \vec{v})$ is the particle distribution for each plasma species α, $\vec{F}$ is the force acting on the particles, $\vec{\nabla}_x$ is the gradient in $\vec{x}$ space, $\vec{\nabla}_v$ is the gradient in $\vec{v}$ (velocity) space, and the subscript c in $(\partial f_\alpha/\partial t)_c$ indicates that this term accounts changes to f_α due to collisions. If the body force $\vec{F}$ is entirely electromagnetic (i.e. Lorentz force), then the Boltzmann equation can be written as:

$$\frac{\partial f_\alpha}{\partial t} + \vec{v}_\alpha \cdot \vec{\nabla}_x f_\alpha + \frac{q_\alpha}{m_\alpha}\left(\vec{E} + \vec{v}_\alpha \times \vec{B}\right) \cdot \vec{\nabla}_v f_\alpha = \left(\frac{\partial f_\alpha}{\partial t}\right)_c. \tag{1.4}$$

Even simplified kinetic models such as PIC or solutions to the Boltzmann equation carry a significant computational expense. Thus, when the properties of the plasma allow, there is a strong motivation to develop and use continuum, fluids-based models.

1.2.2 Fluid-Based Models

Magnetohydrodynamics (MHD) studies the dynamics of fluids which are electrically conductive. The original, classical model of magnetohydrodynamics is referred to as Ideal MHD and it models the plasma as a single fluid. The Ideal MHD model solves the continuity equation (1.5),

the momentum equation (1.6) and Ampere's Law assuming no electric fields (1.7):

$$\frac{\partial \rho}{\partial t} + \vec{\nabla} \cdot (\rho \vec{u}) = 0, \tag{1.5}$$

$$\frac{\partial \rho \vec{u}}{\partial t} + \vec{\nabla} \cdot \left(\rho \vec{u} \otimes \vec{u} + p \vec{\vec{I}} \right) = -\frac{1}{\mu_0} \vec{B} \times \left(\vec{\nabla} \times \vec{B} \right), \tag{1.6}$$

$$\frac{\partial \vec{B}}{\partial t} = \vec{\nabla} \times \left(\vec{u} \times \vec{B} \right), \tag{1.7}$$

$$\frac{d}{dt} \left(\frac{p}{\rho^\gamma} \right) = 0, \tag{1.8}$$

$$\vec{\nabla} \cdot \vec{B} = 0. \tag{1.9}$$

The model is closed by assuming an equation of state, typically a adiabatic ideal gas is assumed (1.8), and measures are taken to ensure the preservation of Gauss's law (1.9). The relative simplicity of the Ideal MHD model has enabled the successful and efficient simulation of many important plasmas, such as solar wind and magnetosphere; however, there are some limitations to the single-fluid, Ideal MHD model. Strictly speaking, the Ideal MHD model is only applicable when the plasma is strongly collisional and the particle distributions are Maxwellian. Ideal MHD does not allow for electric fields and therefore the plasma is considered to have zero resistance. Due to the infinite electric conductivity of the plasma, the magnetic field topology is frozen into the fluid and is forced to move along with it[12]. Because of the simplifying assumptions of this model, it only applies to smooth, slowly-evolving plasmas and does not resolve spatial detail on the level of the Debye length or skin depth, nor does it resolve temporal detail on the scale of the ion gyration or plasma frequency. Ideal MHD is unable to reproduce plasma phenomenon such as magnetic reconnection, the Hall effect (or more generally, charge separation and the resulting electric fields that develop), and the diamagnetic effect[3,13].

A number of improvements to the Ideal MHD model have been proposed. The resistive or dissipative MHD approach allows for non-zero electron diffusivity by accounting for friction between the electron and ion fluids, which allows the magnetic field topology to break from the fluid

flow[3,14]. Various approaches of an "extended" MHD have been developed to include higher-order terms in the equations to account for effects such as electron pressure gradients, finite Larmor radii, or separate electron inertia[15]. Hall MHD is an extension of classical MHD which includes a Hall current term and is able to account for electric fields[16]. Two-fluid MHD takes traditional, single-fluid MHD a step closer to a full, multi-fluid model by considering separately the inertia of electrons, therefore allowing for the evolution of electric fields and a more complete set of electromagnetic equations[4]. However, as the modeled physics trend towards realism, there is a growing disparity in length and time scales in the model and a resulting increase in the numerical and mathematical stiffness of the problem. When separate equations are solved for electrons and ions, the inertial timescales differ by three or more orders of magnitude due to the differences in particle mass.

One method — used in both academic and commercial codes — to handle the timescale disparity is referred to as the hybrid modeling (HM) approach. The physical processes are compartmentalized into modules, each with their own inputs, outputs, and algorithms. The modules are then combined using time-slicing techniques, where one module is executed while either holding inputs from other modules constant or varying the inputs in a prescribed manner. HM often addresses the high spatial gradient and boundary condition complexity from the plasma sheath by including a separate, analytical sheath model; this allows the remaining spatial domain to be comprised of a more uniform, lower-density grid or mesh[4,17]. HM trades accuracy in order to achieve efficient computation on individual computers. Most existing, HM-type plasma codes are developed to run on individual computer nodes or cores, and are limited to fixed, predefined spatial discretization grids.

In contrast to the methods of magnetohydrodynamics and hybrid models, the multi-fluid method of plasma modeling requires solving the equations of fluid motion, for each species in the plasma, self-consistently with Maxwell's equations; the fluid and electromagnetic equations are coupled through their source terms. Clearly this approach adds complexity and requires more computational resources than the aforementioned MHD models, but the advantages are numerous. The multi-fluid model allows separate motion for all species in the plasma, and therefore captures local disruptions

in neutrality which result in electric fields and complex, high frequency (both spatial and temporal) waves.

A five-moment formulation of the multi-fluid plasma model has been studied extensively by Shumlak, Loverich, and Hakim[18–20] on fixed grids with 2nd and 3rd-order accurate schemes; their work characterizes the multi-fluid approach to plasma modeling and demonstrates advantages over a more traditional MHD method. Authors Abgrall and Kumar[21] provide a similar, 5-moment, two-fluid plasma model, with an implicit treatment of the source terms and explicit treatment for fluxes. Balsara et al.[22] have proposed a two-fluid plasma model with a novel method of ensuring the divergence conditions in the electromagnetic equations (Gauss's laws) are maintained, along with a multidimensional Riemann solver for their plasma model. Huang, et al.[23] have applied a 6-moment derivation of the Boltzmann equation to the multi-fluid plasma model, with a point-implicit discretization of the source terms and anisotropic pressure terms. Recently, Ghosh et al.[24] have introduced a multi-fluid model called Euclid. In addition to solving the fluid and electromagnetic equations, Euclid also handles collisions between fluids, including neutral fluids.

There are few existing methods which focus on spatial discretization strategies to cope with this inherit stiffness. The present work introduces adaptive mesh refinement together with a high-order, finite-volume algorithm for multi-fluid plasma modeling, resulting in a new, adaptive, computational framework for future engineering applications. For plasma modeling with a fixed, structured, spatial grid, there are two compromises: either the grid is extremely fine in order to resolve the plasma sheath, or the grid is coarse to promote computational efficiency while relying on a less-accurate sheath model approximation for the material surface boundary conditions. On the other hand, adaptive mesh refinement (AMR) can achieve both computational efficiency as well as highly refined and accurate results in areas with high gradients. By putting more computational grid where the gradients are strongest and leaving the grid coarse where the solution is more quiescent, AMR improves numerical accuracy while simultaneously reducing memory and decreasing solution run-time.

1.3 Objectives

The principal goal of the present work is to apply cutting-edge, numerical algorithms in the development of a novel, multi-fluid type model of plasma physics. To achieve this goal, a multi-fluid plasma model is incorporated into Chord[25–30], the fluid dynamics solver developed by the CFD and Propulsion Laboratory at Colorado State University. Chord is a numerical solver for gaseous fluid flows based on a higher-order, finite-volume method with adaptive mesh refinement. The primary objectives are defined as follows:

- Expand Chord to allow for multiple fluids, each with their own thermodynamic, transport, and electromagnetic properties;
- Integrate an electromagnetic solver into Chord;
- Develop a separate Riemann solver to resolve and compute the electromagnetic flux;
- Extend the fluid physics and boundary conditions in Chord to allow for modeling of plasma;
- Study solution-stabilizing methods for the fourth-order spatial reconstruction algorithm and their application to plasma problems with complex physics such as shocks, discontinuities, and steep gradients;
- Verify and validate the multi-fluid algorithm using standard test cases from literature;
- Apply adaptive mesh refinement to plasma simulations and explore various refinement strategies and the result on computational performance.

Any new numerical algorithm should be verified to ensure the resulting error and order of accuracy match the intention and design of the algorithm. The electromagnetic solver is first verified independently to be fourth-order accurate, and then the full physics of the multi-fluid model is also verified to be fourth-order accurate for problems with smooth solutions. Furthermore, it is essential to validate the solutions produced by an algorithm. As such, the multi-fluid model in Chord is used to solve electromagnetic and plasma test cases with exact solutions, so the results can be compared.

Finally, the algorithm in Chord is applied to common plasma problems from the literature, such as a magnetic shock tube, a plasma explosion, and the GEM magnetic reconnection problem, in order to study the enhancements provided by adaptive mesh refinement and the higher-order spatial reconstruction scheme.

1.4 Dissertation Organization

The structure of this dissertation is as follows. Chapter 1 has provided some background on plasma and plasma modeling techniques, including the focus and objectives of the present work. In Chapter 2, the details of the multi-fluid plasma model are provided, including governing equations. The numerical method used to solve the multi-fluid model is presented in Chapter 3. Chapters 4 – 5 provide verification and validation evidence for the multi-fluid plasma model in Chord. Results of the multi-fluid algorithm in Chord applied to common plasma test problems are given in Chapter 6, with a discussion of solution-stabilizing methods as well as performance enhancements provided by AMR and the higher-order spatial reconstruction method. Finally, Chapter 7 wraps-up this dissertation with some concluding remarks, a summary of original contributions, and thoughts on future work and direction.

Chapter 2

The Multi-Fluid Plasma Model

The intent of this section is to lay the general mathematical framework for the development of a multi-fluid plasma model. The governing equations presented here are applicable to any plasma which can be described by continuum mechanics. To develop the mathematical model, the following assumptions are made:

- The gas density is low enough to ensure the mean free path is large compared to the distance of effective intermolecular forces. This assumption implies molecular chaos in the treatment of collisions — velocities of colliding particles are assumed to be statistically independent — and therefore assumes irreversibility of the Boltzmann equation.
- The mean free path is short compared to the dimensions of the spatial domain; that is, the Knudsen Number, $Kn = \frac{\lambda}{L}$, is less than unity.
- Time, location, and particle velocity are independent variables in the phase space distribution function.
- Body forces acting on the charged plasma species are entirely electromagnetic.

In the multi-fluid approach to plasma modeling, a separate set of fluid equations are solved for each fluid species in the plasma simultaneously with the equations of electromagnetism. Lorentz forces act upon charged fluid species, and the movement and density of these charged species affect the electric current and charge density. This interaction between the fluid and electromagnetic equations is ascribed to the source terms of the respective equations.

2.1 Fluid Equations

The governing equations of fluid mechanics in plasma are a set of partial differential equations (PDEs) describing the conservation of mass, momentum, and energy. These equations correspond

to moments of the Boltzmann equation. The lowest, or zeroth, moment is obtained by integrating equation the Boltzmann equation (1.4) over velocity space[31–34]. The result is the continuity equation,

$$\frac{\partial \rho_\alpha}{\partial t} + \vec{\nabla} \cdot (\rho_\alpha \vec{u}_\alpha) = \left(\frac{\partial \rho_\alpha}{\partial t} \right)_c , \tag{2.1}$$

expressed in terms of mass density ρ_α and mass flux (or momentum density) $\rho_\alpha \vec{u_\alpha}$, where the subscript α represents a specific fluid species. The right side of the continuity equation, $(\partial \rho_\alpha / \partial t)_c$, represents contributions to the species density due to collisions (reactions) within the plasma. The collisional terms will be discussed subsequently. Plasmas are often characterized by the species number density, n_α. Number density is related to the mass density by $\rho_\alpha = m_\alpha n_\alpha$, where m_α is the particle mass of species α.

To obtain an equation for $\rho_\alpha \vec{u_\alpha}$, the first moment of the Boltzmann equation is found by multiplying (1.4) by $m_\alpha \vec{u}_\alpha$ and integrating over velocity space[31]. The result is the fluid momentum equation,

$$\frac{\partial \rho_\alpha \vec{u}_\alpha}{\partial t} + \vec{\nabla} \cdot \left(\rho_\alpha \vec{u}_\alpha \otimes \vec{u}_\alpha + p_\alpha \vec{\vec{I}} \right) = \vec{\nabla} \cdot \vec{\vec{\tau}} + q_\alpha \frac{\rho_\alpha}{m_\alpha} \left(\vec{E} + \vec{u}_\alpha \times \vec{B} \right) - \sum_\beta \vec{R}_{\alpha\beta} + \left(\frac{\partial \rho_\alpha \vec{u}_\alpha}{\partial t} \right)_c , \tag{2.2}$$

where $\vec{E}$ and $\vec{B}$ are the electric and magnetic fields, respectively, $p_\alpha \vec{\vec{I}}$ is the static pressure tensor, $\vec{\vec{\tau}}_\alpha$ is the viscous stress tensor, q_α is the particle charge of species α, m_α is the particle mass of species α, and $\vec{R}_{\alpha\beta}$ represents the momentum transfer due to elastic collisions between species α and each of the other species in the plasma, β. The term $\vec{u}_\alpha \otimes \vec{u}_\alpha$ represents a dyadic product, and the operation results in a dyad or second-rank tensor. The last term on the right side of the momentum equation, $(\partial \rho_\alpha \vec{u}_\alpha / \partial t)_c$, describes contributions to the momentum change of species α from inelastic collisions with other species in the plasma.

The second moment of the Boltzmann equation is obtained by multiplying the Boltzmann equation (1.4) by $\frac{1}{2}m_\alpha u_\alpha^2$ and integrating over velocity space. The integration and some rearrangement yield the fluid energy equation for plasma species α, expressed in divergence form:

$$\frac{\partial \rho_\alpha e_\alpha}{\partial t} + \vec{\nabla} \cdot \left[\rho_\alpha \vec{u_\alpha} \left(e_\alpha + \frac{p_\alpha}{\rho_\alpha} \right) \right] =$$

$$\vec{\nabla} \cdot \left(\vec{\tau} \cdot \vec{u}_\alpha \right) - \vec{\nabla} \cdot \vec{\phi}_\alpha + q_\alpha \frac{\rho_\alpha}{m_\alpha} \left(\vec{u}_\alpha \cdot \vec{E} \right) + \vec{u}_\alpha \cdot \left(\sum_\beta \vec{R}_{\alpha\beta} \right) + \left(\frac{\partial \rho_\alpha e_\alpha}{\partial t} \right)_c, \quad (2.3)$$

where the total specific energy for a thermally-perfect fluid is defined by:

$$e_\alpha \equiv h_\alpha - \frac{p_\alpha}{\rho_\alpha} + \frac{1}{2} \vec{u_\alpha} \cdot \vec{u_\alpha}. \quad (2.4)$$

In the energy equation (2.3), the term p_α is the static pressure, $\vec{\phi}_\alpha$ is the heat flux vector, and h_α is the enthalpy. The energy density addition rate for species α due to reactions within the plasma, $\left(\partial \rho_\alpha e_\alpha / \partial t\right)_c$ will be described in Section 2.3.2.

Equations (2.1) – (2.3) represent the full, fundamental equations of fluid motion in the multi-fluid plasma model. These equations are retained for future use and reference; however, most of the present work focuses on a subset of these equations. Specifically, the equations are simplified to handle collisionless, inviscid plasma fluids. As a result, the simplified subset of fluid equations used throughout most of this dissertation are as follows,

$$\frac{\partial \rho_\alpha}{\partial t} + \vec{\nabla} \cdot \left(\rho_\alpha \vec{u}_\alpha \right) = 0, \quad (2.5)$$

$$\frac{\partial \rho_\alpha \vec{u}_\alpha}{\partial t} + \vec{\nabla} \cdot \left(\rho_\alpha \vec{u}_\alpha \otimes \vec{u}_\alpha + p_\alpha \vec{\vec{I}} \right) = q_\alpha \frac{\rho_\alpha}{m_\alpha} \left(\vec{E} + \vec{u}_\alpha \times \vec{B} \right), \quad (2.6)$$

$$\frac{\partial \rho_\alpha e_\alpha}{\partial t} + \vec{\nabla} \cdot \left[\rho_\alpha \vec{u_\alpha} \left(e_\alpha + \frac{p_\alpha}{\rho_\alpha} \right) \right] = q_\alpha \frac{\rho_\alpha}{m_\alpha} \left(\vec{u}_\alpha \cdot \vec{E} \right). \quad (2.7)$$

2.2 Electromagnetic Equations

Electromagnetic (EM) fields influence the motion of charged fluid species in the plasma through the Lorentz force terms in the momentum equation (2.2). In the energy equation (2.3) the electric field contributes work to charged species. Simultaneously, movement of charged fluids within the plasma affects the distribution of charge and current density, changing the evolution of the electromagnetic fields. This collective behavior of plasmas is described by Maxwell's equations.

2.2.1 Classical Form

A classical representation of Maxwell's equations is as follows:

$$\epsilon_0 \mu_0 \frac{\partial \vec{E}}{\partial t} = \vec{\nabla} \times \vec{B} - \mu_0 \vec{j}, \tag{2.8}$$

$$\vec{\nabla} \cdot \vec{B} = 0, \tag{2.9}$$

$$\frac{\partial \vec{B}}{\partial t} = -\vec{\nabla} \times \vec{E}, \tag{2.10}$$

$$\vec{\nabla} \cdot \vec{E} = \frac{1}{\epsilon_0} \rho_q, \tag{2.11}$$

where $\vec{B}$ is the magnetic field, $\vec{E}$ is the electric field, $\vec{j}$ is the electric current density, and ρ_q is the electric charge density.

2.2.2 Hyperbolic-Only Formulation

The divergence relations imposed by equations (2.9) and (2.11) overconstrain the problem and can result in numerical error or instability. There are multiple approaches to handling this overconstraint. The method used in the present work involves introducing divergence correction potentials

to form purely hyperbolic equations[23,33–38], which take the following form

$$\epsilon_0\mu_0\frac{\partial\vec{E}}{\partial t} - \vec{\nabla}\times\vec{B} + \chi_E\nabla\Phi = -\mu_0\vec{j}, \tag{2.12}$$

$$\frac{\epsilon_0\mu_0}{\chi_B}\frac{\partial\Psi}{\partial t} + \vec{\nabla}\cdot\vec{B} = 0, \tag{2.13}$$

$$\frac{\partial\vec{B}}{\partial t} + \vec{\nabla}\times\vec{E} + \chi_B\nabla\Psi = 0, \tag{2.14}$$

$$\frac{1}{\chi_E}\frac{\partial\Phi}{\partial t} + \vec{\nabla}\cdot\vec{E} = \frac{1}{\epsilon_0}\rho_q, \tag{2.15}$$

where Ψ and Φ are included as correction potentials, used to absorb any divergence errors. The dimensionless, positive, constants χ_B and χ_E determine the speed at which the divergence errors propagate out of the problem domain; they are scalar multipliers on the wave speed of the electromagnetic wave propagation (i.e. the speed of light, $c = 1/\sqrt{\epsilon_0\mu_0}$). These constants are typically set to values slightly greater than one in order to convect error out of the domain faster than the information wave speed without significantly increasing numerical stiffness[34,36,38].

2.3 Model Closure

To close the more general, mathematical model of a multi-fluid plasma, the collision terms in the system of governing equations must be modeled, an equation of state for the fluid equations must be assumed, and the coupling between fluid and electromagnetic equations needs to be closed by defining the EM source terms. In addition, the following assumptions are applied in order to simplify the system and allow the present work to focus on enabling the high-order, solution-adaptive, finite-volume, computational framework for plasma modeling. Specifically, the assumptions are:

- A Maxwellian electron energy distribution is assumed for each fluid.
- Local thermodynamic equilibrium is assumed within each fluid.
- Each plasma species (fluid) is treated as a thermally perfect, ideal gas.

- The hyperbolic-only formulation of Maxwell's equations will be used; this simplifies the system of governing equations and facilitates adaptation into the numerical model.

2.3.1 Coupling of the Fluid and Electromagnetic Equations

In the multi-fluid plasma model, electric current density and charge density are related to the fluid terms as follows:

$$\vec{j} = \sum_{\alpha} q_\alpha \frac{\rho_\alpha \vec{u}_\alpha}{m_\alpha} \tag{2.16}$$

$$\rho_q = \sum_{\alpha} q_\alpha \frac{\rho_\alpha}{m_\alpha}. \tag{2.17}$$

Electric and magnetic fields in the plasma modify the motion of charged fluid species through the Lorentz force terms in the momentum equation (2.2). In the fluid energy equation (2.3), the electric field supplies work to charged species. Concurrently within the plasma, movement of charged fluids affect the distribution of electric charge and current density, influencing the evolution of the electromagnetic fields

2.3.2 Collisions

As previously discussed, electromagnetic fields can provide a strong, long-range influence to the motion and energy transport of charged, plasma species. However, shorter-range interactions (collisions) with other plasma constituents can also have a significant effect on the evolution of a plasma: particles may exchange momentum or energy, neutral particles may become ionized, ionized particles may become neutral, and particles may transfer charge. Furthermore, in more complex and/or molecular gases, collisions may result in molecular dissociation, recombination, negative ions, vibrational and rotational excitation, and more.

Total momentum and energy are both conserved during collision events. Electrons and fully-stripped ions carry only kinetic energy. Atoms and partially-stripped ions have internal energy levels which can be excited, quenched, or ionized; these events correspond to changes in the parti-

cle's potential energy. It is the total energy — the sum of potential and kinetic fractions — that is conserved in a collision.

Collisions that do not result in an exchange of internal energy are referred to as "elastic". In these cases, the sum of kinetic energies is conserved. The transfer of momentum from elastic collisions manifests as a frictional drag term, $\sum_\beta \vec{R}_{\alpha\beta}$, in Equations (2.2) and (2.3). The rate of momentum transfer between species α and β is modeled as:

$$\vec{R}_{\alpha\beta} = \frac{m_\alpha m_\beta}{m_\alpha + m_\beta} n_\alpha \nu_{\alpha\beta} \left(\vec{u}_\alpha - \vec{u}_\beta\right), \tag{2.18}$$

where $\nu_{\alpha\beta}$ is the collision frequency between species α and β and $n_\alpha = \rho_\alpha / m_\alpha$. Because these momentum transfer collisions are purely elastic, the inverse reaction rate must be $\vec{R}_{\beta\alpha} = -\vec{R}_{\alpha\beta}$. The inter-species momentum transfer rate is $\vec{R}_{\alpha\alpha} = 0$. Instead, the frictional drag within a species is represented by the viscous stress tensor $\vec{\vec{\tau}}$ in the fluid Equations (2.2) and (2.3).

When kinetic energy is not conserved during a collision, then the potential energy of one or more of the species involved must change. These processes are referred to as "inelastic," and result in ionization, recombination, excitation, quenching, dissociation, or charge exchange. The transfer of momentum and energy between species due to inelastic collisions is accounted for by the $\left(\partial \rho_\alpha \vec{u}_\alpha / \partial t\right)_c$ and $\left(\partial \rho_\alpha e_\alpha / \partial t\right)_c$ source terms in Equations (2.2) and (2.3), respectfully. The production and destruction of species from inelastic collisions is represented in the continuity equation (2.1), as $\left(\partial \rho_\alpha / \partial t\right)_c$

The inelastic collision reaction rates are calculated by utilizing the Bhatnagar–Gross–Krook (BGK) collision operator to arrive at a discrete expression for the collisional source component of the Boltzmann equation (1.4)[39]. The corresponding source terms in the continuity, momentum,

and energy equations are as follows:

$$\left(\frac{\rho_\alpha}{\partial t}\right)_c = \sum_\beta m_\alpha r_{\alpha\beta}, \tag{2.19}$$

$$\left(\frac{\rho_\alpha \vec{u}_\alpha}{\partial t}\right)_c = \sum_{\beta|r_{\alpha\beta}<0} m_\alpha u_\alpha r_{\alpha\beta} + \sum_{\beta|r_{\alpha\beta}>0} m_\alpha u_\beta r_{\alpha\beta}, \tag{2.20}$$

$$\left(\frac{\rho_\alpha e_\alpha}{\partial t}\right)_c = \sum_{\beta|r_{\alpha\beta}<0} e_\alpha r_{\alpha\beta} + \sum_{\beta|r_{\alpha\beta}>0} e_\beta r_{\alpha\beta}, \tag{2.21}$$

Each individual $r_{\alpha\beta}$ term has a positive sign if the reaction results in a production of species α or a negative sign if the reaction destroys particles of species α. For each reaction (collisional process), the reaction rate is calculated as the product of the reaction rate coefficient $k_{\alpha\beta}$ and the densities of the reactants. For a simple model involving only 2-body collisions, the reaction rates are determined by:

$$r_{\alpha\beta} = k_{\alpha\beta} n_\alpha n_\beta. \tag{2.22}$$

The reaction rate coefficients, $k_{\alpha\beta}$, for many plasma reactions can be found in literature. Or, if the temperature (energy) dependent collision cross sections are known, and the electron energy distribution function is known or assumed, one can integrate the product of the collision cross section, $\sigma_{\alpha\beta}$ and the electron velocity over the electron energy distribution function to determine the reaction rate coefficient for electron scattering events:

$$k_{\alpha\beta} = \langle \sigma_{\alpha\beta} u_\beta \rangle = \frac{\int_0^\infty \sigma_{\alpha\beta} u_\beta f_\beta de_\beta}{\int_0^\infty f_\beta de_\beta}, \tag{2.23}$$

where, in this case, β represents the electron species, and f_β is the electron energy distribution function.

In the present work, only a preliminary, rudimentary treatment of collisions has been developed, requiring predetermined reactions and rate coefficients to be supplied by the user. Furthermore, all of the test cases presented in this dissertation assume a collisionless plasma, so it is not necessary to consider the contribution of collisions in the source terms of the governing equations. However, long-term, beyond the scope of the present work, it is our intention to incorporate a routine into Chord for calculating collision rate coefficients dynamically, based on the species energy and collision cross section tables.

2.3.3 Equation of State

The definition of total energy depends on the equation of state. In most of the present work, we assume a compressible, calorically-perfect ideal gas, with total energy density modeled as

$$\rho_\alpha e_\alpha \equiv \frac{1}{2}\rho_\alpha \left(\vec{u_\alpha} \cdot \vec{u_\alpha}\right) + \frac{p_\alpha}{\gamma_\alpha - 1}, \tag{2.24}$$

where γ_α is the ratio of specific heats for fluid α. However, when exploring higher-temperature extensions to the thermophysical gas models in Chord, the fluids are assumed to behave as thermally perfect, ideal gases, where the relationship between fluid species pressure and temperature are described by the Ideal Gas Law

$$p_\alpha = R_\alpha \rho_\alpha T_\alpha, \tag{2.25}$$

where R_α represents the specific gas constant. Furthermore, in a thermally-perfect gas, the specific heat and enthalpy are temperature-dependent properties.

$$h_\alpha = h_\alpha \left(T_\alpha\right) \qquad C_{p_\alpha} = \left(\frac{dh}{dT}\right)_\alpha \tag{2.26}$$

Chapter 3

Numerical Method

The multi-fluid plasma model presented here is built upon the computational framework Chord[25–30], our in-house computational fluid dynamics (CFD) code. This framework provides a highly parallel, fourth-order accurate, solution-adaptive, finite-volume CFD algorithm. Currently, Chord solves transient, compressible, viscous, gaseous fluid flows, with or without chemical reactions. Chord achieves superior accuracy and parallel performance for simulations of fluid physics where flows exhibit multi-scale behavior, such as turbulence, combustion, shock, or plasma. Adaptive mesh refinement allows for under-resolved gradients in the solution to be identified and the mesh to be locally refined in these zones, without needless and inefficient refinement in smooth regions of the domain. These refined mesh patches are subcycled relative to the coarser patches in order to preserve time synchronization and stability at the refined level(s). Higher-order spatial reconstruction methods are inherently prone to oscillations near discontinuities. To mitigate this risk, Chord employs a number of numerical stabilization methods, which will be discussed below.

The high-order, finite-volume method (FVM) can produce solutions to smooth flows much faster than low-order schemes, to the same level of accuracy. Finite-volume methods are well-suited for problems with discontinuities and naturally satisfy the conservation property. The solution-stabilizing and conservation-preserving nature of the FVM has also been shown to be an accurate and efficient tool for solving the electromagnetic field equations[35–37,40,41].

3.1 Conservative Form of the Governing Equations

For the convenience of algorithm implementation, the aforementioned governing equations of the multi-fluid plasma model — fluid Equations (2.5) – 2.7 and electromagnetic Equations (2.12)

– 2.15 — can be written in conservative form, arranged in the following convention:

$$\frac{\partial \mathbf{U}}{\partial t} + \vec{\nabla} \cdot \vec{\mathbf{F}} = \vec{\nabla} \cdot \vec{\mathbf{G}} + \mathbf{S}. \tag{3.1}$$

In this equation, **U** is the vector of solution variables: an amalgamation of the conserved terms from the fluid equations for each species and the conserved terms from the electromagnetic equations. $\vec{\mathbf{F}}$ is a dyadic tensor of inviscid (hyperbolic) flux terms, $\vec{\mathbf{G}}$ is a dyadic tensor of viscous (elliptic) flux terms and **S** is a vector of source terms. The number of fluid species in the model determines the length of the vectors. In Cartesian coordinates, for two species, i (ions) and e (electrons), using the hyperbolic-only formation of Maxwell's equations, the solution vector **U** is arranged as follows:

$$\mathbf{U} = [\rho_i, \rho_i u_{i\,x}, \rho_i u_{i\,y}, \rho_i u_{i\,z}, \rho_i e_i, \rho_e, \rho_e u_{e\,x}, \rho_e u_{e\,y}, \rho_e u_{e\,z}, \rho_e e_e,$$

$$E_x, E_y, E_z, \Psi, B_x, B_y, B_z, \Phi]^T \,. \tag{3.2}$$

It is worth noting that the above solution vector applies regardless of the number of spatial dimensions modeled. This treatment is used because of the cross-product operations in the momentum equation (2.2) and Maxwell's equations (2.12) and (2.14) reference perpendicular vector components. In three dimensions, flux is computed in each direction, x, y, and z. In two dimensions, flux is only computed in the x and y directions; the z-components of the vector-based solution terms may still evolve due to influence from their source terms, but there is no flux computed in the z-direction. Finally, in one dimension, flux is computed in the x direction only, and the y and z components of the vector based solution terms are influenced only by their source terms. Examples of the full vectors and tensors in Equation (3.1) are provided in Appendix A.

3.2 Higher-Order Reconstruction

The finite-volume method of solving a partial differential equation is based on discrete approximation to the integral equation over control volumes. Essentially, the divergence theorem is applied

to replace the volume integrals by surface integrals over the control volume boundaries, and then the boundary integrals are approximated using quadratures. The discretized solution in space is an average of the solution, **U**, over a control volume $\boldsymbol{i}$.

Our finite-volume method is based on cell-centers. The computational grid is Cartesian, which facilitates the use of adaptive mesh refinement. Cells are indexed by an integer vector $(i_0, ..., i_{D-1}) = \boldsymbol{i} \in \mathbb{Z}^D$ and the faces by $\boldsymbol{i} \pm \frac{1}{2}\boldsymbol{e}^d$, where $\mathbf{e}^d$ is a unit vector in direction d. Integrating Equation (3.1) (neglecting the viscous terms, $\vec{\mathbf{G}}$, for simplicity) over a control volume, V_i, gives

$$\frac{\partial}{\partial t}\int_V \mathbf{U}\,\mathrm{d}V + \int_V \left(\vec{\nabla}\cdot\vec{\mathbf{F}} - \mathbf{S}\right)\mathrm{d}V = 0\,. \tag{3.3}$$

Applying Gauss's divergence theorem to Equation (3.3) over the control volume of cell $\boldsymbol{i}$, as shown in Figure 3.1, results in the semi-discrete form as

$$\frac{\mathrm{d}\langle\mathbf{U}\rangle_{\boldsymbol{i}}}{\mathrm{d}t} = -\frac{1}{V}\sum_{d=0}^{D-1}\left(\langle\vec{\mathbf{F}}\rangle_{\boldsymbol{i}+\frac{1}{2}\boldsymbol{e}^d} - \langle\vec{\mathbf{F}}\rangle_{\boldsymbol{i}-\frac{1}{2}\boldsymbol{e}^d}\right) + \langle\mathbf{S}\rangle_{\boldsymbol{i}}, \tag{3.4}$$

where the integral quantity in a cell is defined by $\langle\mathbf{U}\rangle \equiv \frac{1}{V}\int_V \mathbf{U}dV$.

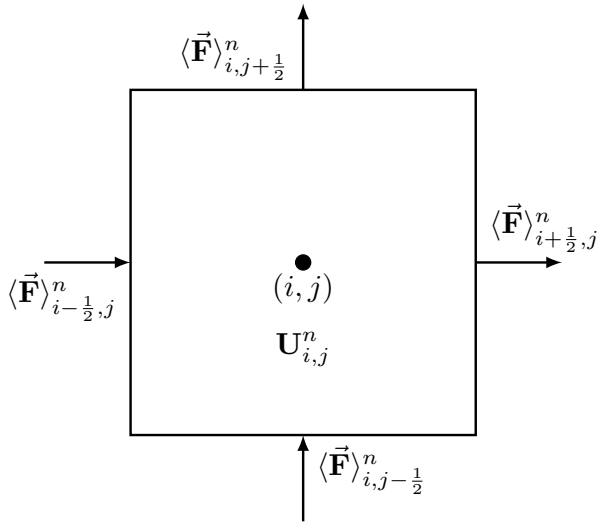

Figure 3.1: Illustration of a finite-volume method on a 2D Cartesian control volume

The order of accuracy for a FVM is dependent on the spatial discretization scheme used to compute fluxes on the bounding surfaces of the control volume. Chord uses a fourth-order, center-differencing method for reconstructing the face-averaged quantities and the face-averaged gradients, which are subsequently used for hyperbolic and elliptic flux evaluation. However, where strong discontinuities or shock waves are present, the hyperbolic flux is then evaluated based on the upwind scheme by solving a Riemann problem at each cell face. A piecewise parabolic method (PPM) limiter, as modified by McCorquodale and Colella[42], is used in the present implementation of Chord. Additionally, a slope flattening algorithm and optional, artificial viscosity can be added to the solution procedure to further stabilize problems with sharp discontinuities or when only inertial (hyperbolic) physics are being solved for. For more detail on the spatial discretization, interested readers are referred to previous publications on Chord [25–30].

3.3 Flux Evaluation

As a result of the numerical quadrature, two different values of the flux for a solution quantity may be obtained at a cell-face in a given coordinate direction due to the use of two different stencils during the reconstruction process. To resolve the discontinuity, a Riemann problem at each face is solved.

3.3.1 Convolution and Deconvolution

The spatial terms on the right side of Equation (3.4), $\langle \vec{\mathbf{F}} \rangle_{\boldsymbol{i} \pm \frac{1}{2}\boldsymbol{e}^d}$, are evaluated using the cell-averaged conserved solution terms, $\langle \mathbf{U} \rangle_{\boldsymbol{i}}$. However, the exact computational process involves a sequence of operations, converting **U** to primitive variables, **W**, which are eventually used for the calculation of $\langle \vec{\mathbf{F}} \rangle_{\boldsymbol{i} \pm \frac{1}{2}\boldsymbol{e}^d}$. For the fluid equations, the conserved variables $\mathbf{U} = [\rho_\alpha, \rho_\alpha \vec{u_\alpha}, \rho_\alpha e_\alpha]$ are converted to primitive variables $\mathbf{W} = [\rho_\alpha, \vec{u_\alpha}, p_\alpha]$. Readers interested in the exact details of this process are referred to previous, in-depth publications[27,42]. For reference, a simple overview of the transformation between cell-averaged conserved variables and face-averaged primitive variables is as follows:

1. Convert the cell-averaged solution variables $\langle \mathbf{U} \rangle$ to cell-averaged primitive variables $\langle \mathbf{W} \rangle$;

2. Interpolate the cell-averaged primitive variables $\langle \mathbf{W} \rangle$ to face-averaged primitive variables $\langle \mathbf{W} \rangle_{\boldsymbol{i} \pm \frac{1}{2} \boldsymbol{e}^d}$ using a fourth-order accurate reconstruction;

3. Compute face-centered primitive variables $\mathbf{W}_{\boldsymbol{i} \pm \frac{1}{2} \boldsymbol{e}^d}$ from the face-averaged primitive variables $\langle \mathbf{W} \rangle_{\boldsymbol{i} \pm \frac{1}{2} \boldsymbol{e}^d}$;

4. Compute the face-average fluxes $\langle \vec{\mathbf{F}} \rangle_{\boldsymbol{i} \pm \frac{1}{2} \boldsymbol{e}^d}$ using both the face-average and face-centered primitive variables.

These convolution and deconvolution operations to switch between conservative and primitive variables are only performed for the fluid equations. The electromagnetic equation algorithm uses conservative variables $\mathbf{U} = \left[\vec{E}, \Psi, \vec{B}, \Phi \right]$ for the flux, limiter, and Riemann solution calculations, and therefore a transformation to primitive variables is unnecessary.

3.3.2 Riemann Solvers

In the multi-fluid plasma model, we consider a Harten-Lax-van Leer contact wave (HLLC) method[41,43–45] to approximate a solution to the Riemann problem (initial value problem). In an improvement to the HLL scheme, the HLLC method restores the full wave structure inside the Riemann "fan" by replacing the single averaged state of the HLL scheme with two approximate states, $\mathbf{U}_L^*$ and $\mathbf{U}_R^*$. These states are separated by a contact wave in the middle, which is assumed to have a constant speed. The waves and states in the HLLC method are depicted in the Riemann fan illustration in Figure 3.2.

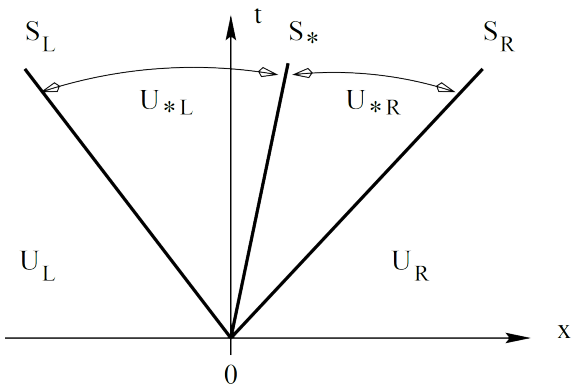

Figure 3.2: Riemann fan diagram for the HLLC metohd

The solution on the $x/t = 0$ axis is written as

$$\mathbf{U}(0,t) = \begin{cases} \mathbf{U}_L & \text{if } \lambda_L \geq 0, \\ \mathbf{U}_L^* & \text{if } \lambda_L \leq 0 \leq \lambda^*, \\ \mathbf{U}_R^* & \text{if } \lambda^* \leq 0 \leq \lambda_R, \\ \mathbf{U}_R & \text{if } \lambda_R \leq 0, \end{cases} \tag{3.5}$$

where λ_L is the minimum characteristic wave speed, λ_R is the maximum wave speed, and λ^* is the contact wave speed. Consequently, the corresponding fluxes are

$$\mathbf{F}(0,t) = \begin{cases} \mathbf{F}_L & \text{if } \lambda_L \geq 0, \\ \mathbf{F}_L^* & \text{if } \lambda_L \leq 0 \leq \lambda^*, \\ \mathbf{F}_R^* & \text{if } \lambda^* \leq 0 \leq \lambda_R, \\ \mathbf{F}_R & \text{if } \lambda_R \leq 0. \end{cases} \tag{3.6}$$

Resolving the full wave structure of the Riemann fan is necessary if using a single Riemann solver for the full, multi-fluid governing equations. However, in the work presented herein, separate Riemann solvers are used for the fluid equations and the electromagnetic equations. The fluid Riemann solver for non-reacting fluids is based on the method originally designed by Colella[46], while for

reacting flows the exact solution is solved for[47]. The HLLC method is applied only to the electromagnetic terms, which significantly simplifies the wave structure because the EM wave speeds are constant. The wave speeds for the electromagnetic physics are determined by solving for the eigenvalues of the flux Jacobian, $\partial\mathbf{F}/\partial\mathbf{U}$, and are written as

$$\mathbf{\Lambda} = \left[-\chi_B c, \chi_B c, -\chi_E c, \chi_E c, -c, -c, c, c\right]^T . \tag{3.7}$$

In a homogeneous medium, one can assume continuity of every conserved electromagnetic variable across the cell interface (contact wave). As previous authors[35,38,45] have noted, the assumption of interfacial continuity for all conserved variables results in the HLLC fluxes reverting into the Godunov flux equations. This simplified flux calculation, shown in Equation (3.8), is the method we have used in the present work because it suffices for the test cases considered in this paper. However, the full, HLLC Riemann solver algorithm is retained for future work involving domain discontinuities and heterogeneous medium. Also in future work, we may consider using a single Riemann solver for both fluid and EM equations.

$$\mathbf{F}^d = \begin{bmatrix} \frac{\chi_E}{2}\left(c\left(E_L^d - E_R^d\right) + c^2\left(\Phi_R + \Phi_L\right)\right) \\ \frac{1}{2}\left(c\left(E_L^{d1} - E_R^{d1}\right) + c^2\left(B_R^{d2} + B_L^{d2}\right)\right) \\ \frac{1}{2}\left(c\left(E_L^{d2} - E_R^{d2}\right) - c^2\left(B_R^{d1} + B_L^{d1}\right)\right) \\ \frac{\chi_B}{2}\left(c\left(\Psi_L - \Psi_R\right) + c^2\left(B_R^d + B_L^d\right)\right) \\ \frac{\chi_B}{2}\left(c\left(B_L^d - B_R^d\right) + \left(\Psi_R + \Psi_L\right)\right) \\ \frac{1}{2}\left(c\left(B_L^{d1} - B_R^{d1}\right) - \left(E_R^{d2} + E_L^{d2}\right)\right) \\ \frac{1}{2}\left(c\left(B_L^{d2} - B_R^{d2}\right) + \left(E_R^{d1} + E_L^{d1}\right)\right) \\ \frac{\chi_E}{2}\left(c\left(\Phi_L - \Phi_R\right) + \left(E_R^d + E_L^d\right)\right) \end{bmatrix} . \tag{3.8}$$

In the above equation, $\mathbf{F}^d$ is the electromagnetic flux computed on a face normal to direction d, and $d1$ and $d2$ are the directions tangent to the face; for example, in a 3D Cartesian coordinate system, if $d = 0$ or x, then $d1 = 1$ or y and $d2 = 2$ or z.

3.4 Boundary Conditions

Boundary conditions are required to fully define the computational domain. A well-posed boundary condition approach takes into account the direction of wave propagation and the theory of characteristics. Our approach involves prescribing artificial or ghost states outside the domain boundary and using the Riemann solver to resolve the discontinuity on the physical boundary face between the interiorly-interpolated state and the exteriorly-prescribed state.

3.4.1 Zero-Gradient

An open boundary condition implies the solution information is allowed to leave the domain, ideally without reflection. One approximation of an open boundary condition is to prescribe a zero-gradient of the conservative variables at the boundaries, ∂s, that is:

$$\nabla \mathbf{U}\big|_{\partial s} \cdot \mathbf{e}^d = 0, \tag{3.9}$$

along the normal of the boundary curve or surface. In its simplest form, a 1st-order accurate, zero-gradient boundary condition is implemented by setting the ghost cells values to the boundary-adjacent interior cell values.

3.4.2 Perfect Electrical Conductor

A common boundary condition for the electromagnetic equations is a perfectly electrically conducting (PEC) wall. On a surface with perfect electrical conduction, there are no transverse electric fields, and thus, the normal component of the magnetic field is also zero. When utilizing divergence cleaning potentials in the electromagnetic equations to propagate error out of the domain, the boundary conditions for these values need to be prescribed accordingly. A Neumann type boundary

condition is utilized for the scalar potential Ψ because a Dirichlet boundary is incompatible with the characteristic theory[36]. Written numerically, the definition of a PEC boundary is

$$\mathbf{e}^d \times \vec{E}^* = 0, \tag{3.10}$$

$$\frac{\partial \Psi^*}{\partial d} = 0, \tag{3.11}$$

$$\mathbf{e}^d \cdot \vec{B}^* = 0, \tag{3.12}$$

$$\Phi^* = 0, \tag{3.13}$$

where the terms with superscripts * refer to the state on the boundary face and $\mathbf{e}^d$ is the outward normal unit vector (in direction d) at the face. Accordingly, the exterior ghost states for the PEC boundary on a Cartesian mesh are

$$\begin{bmatrix} E_x^+ \\ E_y^+ \\ E_z^+ \\ \Psi^+ \\ B_x^+ \\ B_y^+ \\ B_z^+ \\ \Phi^+ \end{bmatrix} = \begin{bmatrix} E_x^- \\ -E_y^- \\ -E_z^- \\ \Psi^- \\ -B_x^- \\ B_y^- \\ B_z^- \\ -\Phi^- \end{bmatrix} \tag{3.14}$$

where the superscripts $+$ and $-$ refer to the faces outside and inside the domain, respectively[36,38].

3.4.3 Silver-Müller Absorbing Boundary Condition

A Silver -Müller absorbing boundary condition (ABC) can artificially truncate the domain without reflecting parasitic information to the interior.

$$\left(\vec{E^*} - \vec{B^*} \times \mathbf{e}^d\right) \times \mathbf{e}^d = \left(\vec{E^{inc}} - \vec{B^{inc}} \times \mathbf{e}^d\right) \times \mathbf{e}^d, \tag{3.15}$$

$$\frac{\partial \Psi^*}{\partial d} = 0, \tag{3.16}$$

$$\Phi^* = 0, \tag{3.17}$$

where $\vec{E^{inc}}$ and $\vec{B^{inc}}$ are given fields along the boundary. The computation method of the ABC boundary is the same as the PEC boundary, but with different prescribed, exterior ghost states

$$\begin{bmatrix} E_x^+ \\ E_y^+ \\ E_z^+ \\ \Psi^+ \\ B_x^+ \\ B_y^+ \\ B_z^+ \\ \Phi^+ \end{bmatrix} = \begin{bmatrix} E_x^{inc} \\ E_y^{inc} \\ E_z^{inc} \\ \Psi^- + \left(\vec{B^{inc}} - \vec{B^-}\right) \cdot \mathbf{e}^d \\ B_x^{inc} \\ B_y^{inc} \\ B_z^{inc} \\ -\Phi^- + \left(\vec{E^{inc}} - \vec{E^-}\right) \cdot \mathbf{e}^d \end{bmatrix}. \tag{3.18}$$

3.5 Time Marching Method

Chord is equipped with multiple time-stepping methods, including the standard 4th-order, explicit, Runge-Kutta method (RK4) as well semi-implicit approaches such as a 4th-order additive Runge-Kutta method (ARK4). For the present work, the standard, explicit RK4 method is used.

The general form of the standard RK4 method is as follows

$$\hat{\mathbf{U}}_{n+1/2} = \mathbf{U}_n + \frac{\Delta t}{2}\mathbf{U}_n' \tag{3.19}$$

$$\tilde{\mathbf{U}}_{n+1/2} = \mathbf{U}_n + \frac{\Delta t}{2}\hat{\mathbf{U}}_{n+1/2}' \tag{3.20}$$

$$\bar{\mathbf{U}}_{n+1} = \mathbf{U}_n + \Delta t\tilde{\mathbf{U}}_{n+1/2}' \tag{3.21}$$

$$\mathbf{U}_{n+1} = \mathbf{U}_n + \frac{\Delta t}{6}\left[\mathbf{U}_n' + 2\left(\hat{\mathbf{U}}_{n+1/2}' + \tilde{\mathbf{U}}_{n+1/2}'\right) + \bar{\mathbf{U}}_{n+1}'\right]. \tag{3.22}$$

In explicit methods, it is necessary to resolve the fastest-propagating information and physical oscillations within the plasma. In the multi-fluid plasma model, typically the fastest wave speed is the speed of light, c, or potentially the divergence error propagation rates, $\chi_B\, c$ or $\chi_E\, c$, if one is using the hyperbolic-only electromagnetic equations.

As pointed out in previous papers[19,34] on the multi-fluid plasma model, it is also critical to resolve the oscillations attributed to cyclotron and plasma frequencies. Therefore, the explicit time step specification in Chord adheres to the following criteria:

$$\Delta t_{max} = min\left[\text{CFL}\left(\frac{\Delta x}{c_{s\,\alpha}}, \frac{\Delta x}{c_{s\,\alpha} + u_{x\,\alpha}}, \frac{\Delta x}{c}, \frac{\Delta x}{\chi_B c}, \frac{\Delta x}{\chi_E c}\right), \frac{0.5}{\omega_{c\,\alpha}}, \frac{0.5}{\omega_{p\,\alpha}}\right], \tag{3.23}$$

where Δt is the time step, Δx is the grid spacing, each species α sound speed is $c_{s\,\alpha} = \sqrt{\gamma_\alpha \frac{p_\alpha}{\rho_\alpha}}$, the cyclotron frequency is $\omega_{c\,\alpha} = q_\alpha \frac{\|\vec{B}\|}{m_\alpha}$, and the plasma frequency is $\omega_{p\,\alpha} = \sqrt{\frac{n_\alpha q_\alpha^2}{\epsilon_0 m_\alpha}}$. The dimensionless parameter CFL refers to the Courant number. The values of 0.5 appearing in Equation (3.23) are used to satisfy the criterion of the Nyquist–Shannon sampling theorem.

3.6 Adaptive Mesh Refinement

It is common for plasmas to experience localized, sharp discontinuities and shocks in response to perturbations. Even in cases of steady, relatively placid plasmas such as glow discharges used in industrial plasmas, the plasma sheath presents steep gradients and hyper-local regions with abrupt

changes in density. Large disparities in length scale like this drive significant mathematical stiffness in numerical simulations of these plasmas. Adaptive mesh refinement has the potential to mitigate the stiffness by adapting resolutions locally to the scales of the solution.

AMR adjusts the mesh-resolution in response to the solution, increasing resolution in regions where the solution variables are discontinuous or feature strong, under-resolved gradients, and coarsening the mesh in quiescent or smooth regions to improve computational efficiency. AMR is provided in Chord by use of the Chombo library[48]. Our multi-fluid plasma model is constructed to leverage and incorporate AMR; however, the present work makes no modifications to the AMR framework. The brief review of AMR presented herein serves only to provide an overview of the technology. For more detail, interested readers are referred to previous publications on the implementation of AMR in Chord [27,49].

Figure 3.3 illustrates a structured AMR grid in 2D with 2 levels of refinement using a refinement ratio of 2 between levels. In the AMR process, identifying or "tagging" cells for refinement is a fundamental aspect of the algorithm. Some common methods include those based on solution values or gradients, vorticity, or geometry properties. For the present work, we utilize tagging methods based on solution variable values and also based on a computed, relative gradient:

$$\nabla_{rel} = \frac{W_{i+1} - W_{i-1}}{W_{i+1} + W_{i-1}}, \tag{3.24}$$

where W represents some solution variable, and the subscript i refers to the cell indexing along a coordinate direction. Furthermore, the AMR refinement ratio can be specified for each level of refinement.

When the mesh is refined and the cells are divided into smaller sizes, the integration time step in those finer cells also requires refinement to maintain solution stability. In a process called subcycling, finer mesh patches are integrated in time multiple times compared to the coarser mesh regions, in order to preserve time synchronization. During this process, ghost cells need to be filled at AMR interfaces by interpolation from the next coarser mesh level. Subcycling requires that the finer mesh patches are solved at an intermediate time relative to the coarser patches; the in-

terpolation from coarse to fine patches is accomplished using a "Dense Output" time interpolation scheme[50]. During integration of the coarse mesh from time t_n to t_{n+1} using the RK4 method, the intermediate stage values are stored for use in time interpolation. Then, the finer mesh is integrated over the same interval with multiple time steps, as illustrated in Figure 3.4. At each RK4 stage of each time step, the coarser solution is interpolated in time (and space) to fill the ghost cells at the AMR boundaries on the finer mesh. More details and rigorous explanations of time stepping with AMR in Chord are available in previous publications from our lab [25–30,50–52]

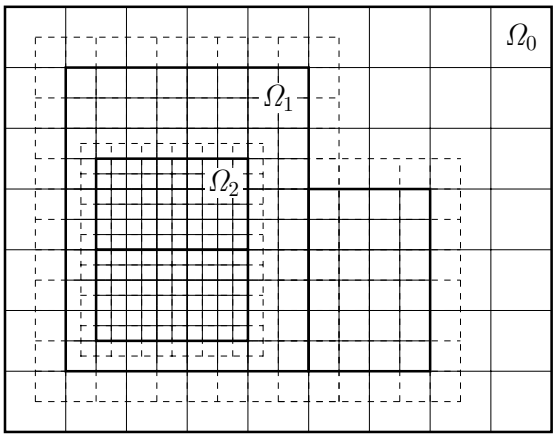

Figure 3.3: Illustration of adaptive mesh refinement on a 2D Cartesian mesh. The labels Ω_0, Ω_1, and Ω_2 represent the progressively higher-resolution meshes, applied selectively to subsets of the domain. In this illustration, the refinement ratio between each level is 2. The boxes outlined in thicker black borders represent the decomposition of the domain into a disjoint union of boxes for parallel computing. The dashed lines represent ghost cells in which the values are interpolated from the coarser mesh.

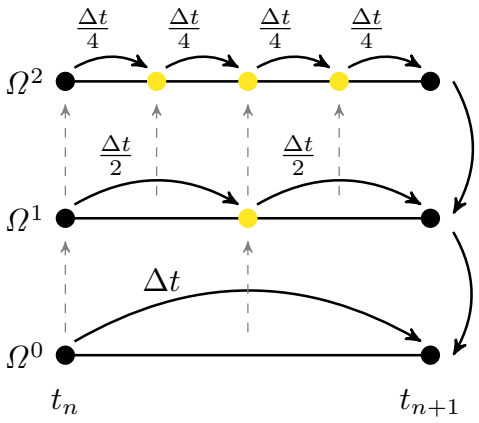

Figure 3.4: Subcycling allows finer grids to be integrated in time using interpolated data from the next coarser grid to fill ghost cells at the AMR boundaries, indicated by the dashed gray lines. In this example, there are two levels of grid refinement, with a refinement ratio of 2 between each level; thus, the timestep is halved as each successfully refined level is subcycled.

3.7 Solution-Stabilizing Methods

A fourth-order accurate reconstruction of the solution in space is inherently prone to oscillatory behavior in the fluid equations near discontinuities. During reconstruction of the face values in our finite volume method, a limiter is employed to suppress oscillations near shocks and under-

resolved gradients. The limiter locally reduces the order of accuracy in these regions. However, in extreme cases, such as those involving strong shocks or locally varying source terms from reactions or electromagnetic fields, further solution-stabilizing techniques are sometimes required. In this section we discuss some of these techniques, including artificial viscosity, face value limiting, a higher-order clipping algorithm for use with AMR, and face construction order reduction.

3.7.1 Artificial Viscosity

In the fluid equations, it is sometimes necessary to add artificial (numerical) dissipation in order to suppress oscillations near discontinuities. In Chord, this is accomplished by introducing an moderate, modifiable, artificial viscosity into the fluid equations in the vicinity of shocks. The artificial viscosity is calculated based on the conservative solution variable gradients and the divergence of fluid velocity, and the magnitude is adjusted through two user-defined coefficients. Application of artificial viscosity to the solution is analogous to incrementing the total flux by some relatively small amount. In regions of smooth flow, the artificial viscosity makes an $O\left(\Delta x^4\right)$ contribution to the solution (where Δx is the grid spacing), preserving the fourth-order accuracy[42]. Artificial viscosity, if enabled, is only applied to the fluid equations in Chord, not the electromagnetic equations.

3.7.2 High-Order Adaptive Clipping-and-Redistribution

When using AMR with a fourth-order accurate reconstruction scheme, newly refined patches are prone to oscillations when proximal to non-smooth solution features. These oscillations can create new extrema and unphysical states when stiff sources are present, which may destabilize a solution. The high-order adaptive clipping-and-redistribution (HO-ACR) method is used to prevent local extrema in these newly refined regions by enforcing adaptively-determined solution bounds. This allows for more robust application of AMR by maintaining stable solutions where non-smooth features are refined or cross AMR interfaces. In addition to preserving fourth-order accuracy in smooth regions, this method maintains solution conservation, requires no predetermined limits, and is non-invasive. An example of the HO-ACR algorithm is show in Figure 3.5. An in-depth

explanation and verification of the HO-ACR algorithm can be found in the paper by Overton-Katz et al[53].

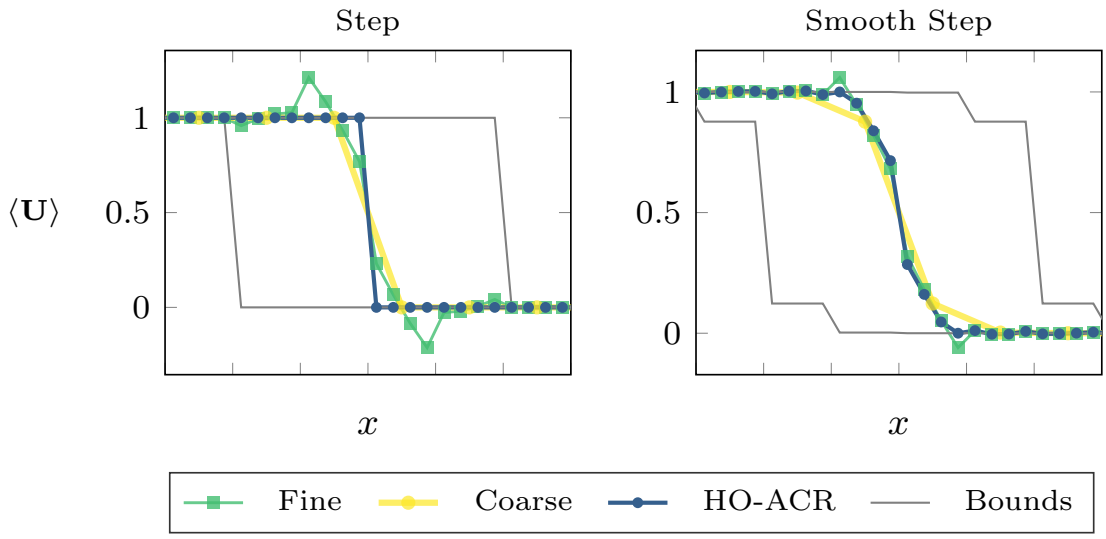

Figure 3.5: 1D interpolation showing the HO-ACR method on Cartesian grids. The interpolation is 4th-order and conservative using a 5-point centered stencil. The x axis shows the coarse cells, and y axis the 4th-order cell-averaged values of the solution. Yellow lines indicate coarse solution values, green lines the coarse to fine interpolation, and blue lines the interpolation with addition of the HO-ACR method. Gray lines show the bounding envelope used by the HO-ACR method for non-smooth regions[53].

3.7.3 Face Value Limiting

The standard limiting approach used in Chord is a high-order extension of the PPM limiter recommended by McCorquodale and Colella[42]. This PPM-based limiter can be organized as three separate steps: limit the face value interpolation, limit the parabolic interpolant construction with consideration for smooth extrema, and apply slope flattening to the interpolants. The first step, face value limiting (FVL), is typically not applied because it can result in excessive dissipation[42]. However, in simulations involving strong shocks and discontinuities, FVL can help stabilize an otherwise unstable or oscillatory solution. The FVL algorithm integrated into Chord is based on the fourth-order FVL method proposed by Colella and Sekora[54], and the integration of FVL replaces the fourth-order face interpolation in the default PPM limiter. Readers interested in the details of the FVL algorithm in Chord are referred to the paper by Owen et al[52].

3.7.4 Face Construction Order Reduction

The face construction order reduction (FCOR) method in Chord is used to selectively modify the order of accuracy of the primitive values used during the construction and limiting of face values. Three conditions are monitored to see if FCOR is necessary. The first check at the cell face involves comparing the difference between the linear face construction using fourth-order average values and second-order values. The second check evaluates the normalized difference between the undivided, second-order face derivatives. The tolerances for both tests are determined through numerical experimentation conducted by Owen et al[52]. The final check considers the tolerance from the nonlinear solver in Chord, and it is performed to ensure FCOR is not applied in regions where round-off error becomes significant. If all three conditions are met, the face values are constructed based on the second-order, primitive state instead of the default, fourth-order state[52].

Chapter 4

Verification

The fluids solver in Chord has already been extensively verified and validated, but the capability to solve Maxwell's equations is a new addition to Chord by the present study. Therefore, prior to studying the full, complex physics of the multi-fluid plasma model, it is prudent to independently validate the electromagnetic solver against a known solution. For this, a three-dimensional, plane-polarized, electromagnetic wave problem with periodic boundary conditions is used. Next, the solution accuracy of the full, multi-fluid plasma model with coupling between the fluid and electromagnetic physics is verified using a one-dimensional, electron acoustic wave problem. Test cases with exact solutions are chosen to provide both verification and validation of the multi-fluid algorithm.

4.1 Three Dimensional Plane-Polarized Electromagnetic Wave in Vacuum

In this problem, a plane-polarized electromagnetic wave propagates across a three dimensional, vacuum domain with Cartesian coordinates of $[0.0, 1.0]$ m in each direction as illustrated in Figure 4.1. Periodic boundary conditions are used so the accuracy of the 4th-order interior scheme can be verified. The exact, electric and magnetic fields are given by the following equations[22]:

$$\vec{E}\,(x,y,z,t) = \cos\left[2\pi\left(x+y+z-c\sqrt{3}\,t\right)\right]\left(0\hat{x}-\frac{1}{\sqrt{2}}\hat{y}+\frac{1}{\sqrt{2}}\hat{z}\right) \tag{4.1}$$

$$\vec{B}\,(x,y,z,t) = \cos\left[2\pi\left(x+y+z-c\sqrt{3}\,t\right)\right]\left(\sqrt{\frac{2}{3}}\hat{x}-\frac{1}{\sqrt{6}}\hat{y}-\frac{1}{\sqrt{6}}\hat{z}\right) \tag{4.2}$$

where $\hat{x}$, $\hat{y}$, and $\hat{z}$ are the components of the $\vec{E}$ and $\vec{B}$ vectors in directions x, y, z. The test case is solved over a range of mesh sizes, all to a final time of 1.2 ns. At the end of each simulation, the numerical solution is compared to the exact solution. The corresponding errors are evaluated using L_1, L_2, and L_∞ norms. Figure 4.2 shows the rate of error reduction with increasing mesh size; clearly, the slopes converge towards -4.0, verifying the fourth-order algorithm. Further, Table 4.1 lists the data for Figure 4.2, including the sequence of grids used, the error norms for both electric and magnetic field components, and error reduction rates between two consecutive mesh sizes.

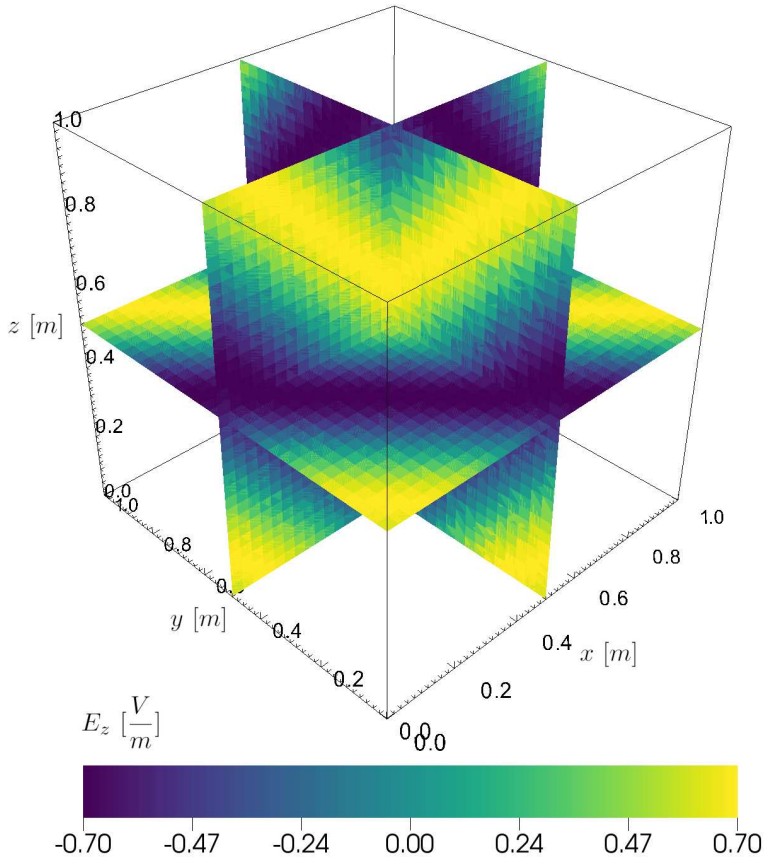

Figure 4.1: Three plane contour plot of variable E_z from the 3D electromagnetic wave test case, at time 1.2 ns.

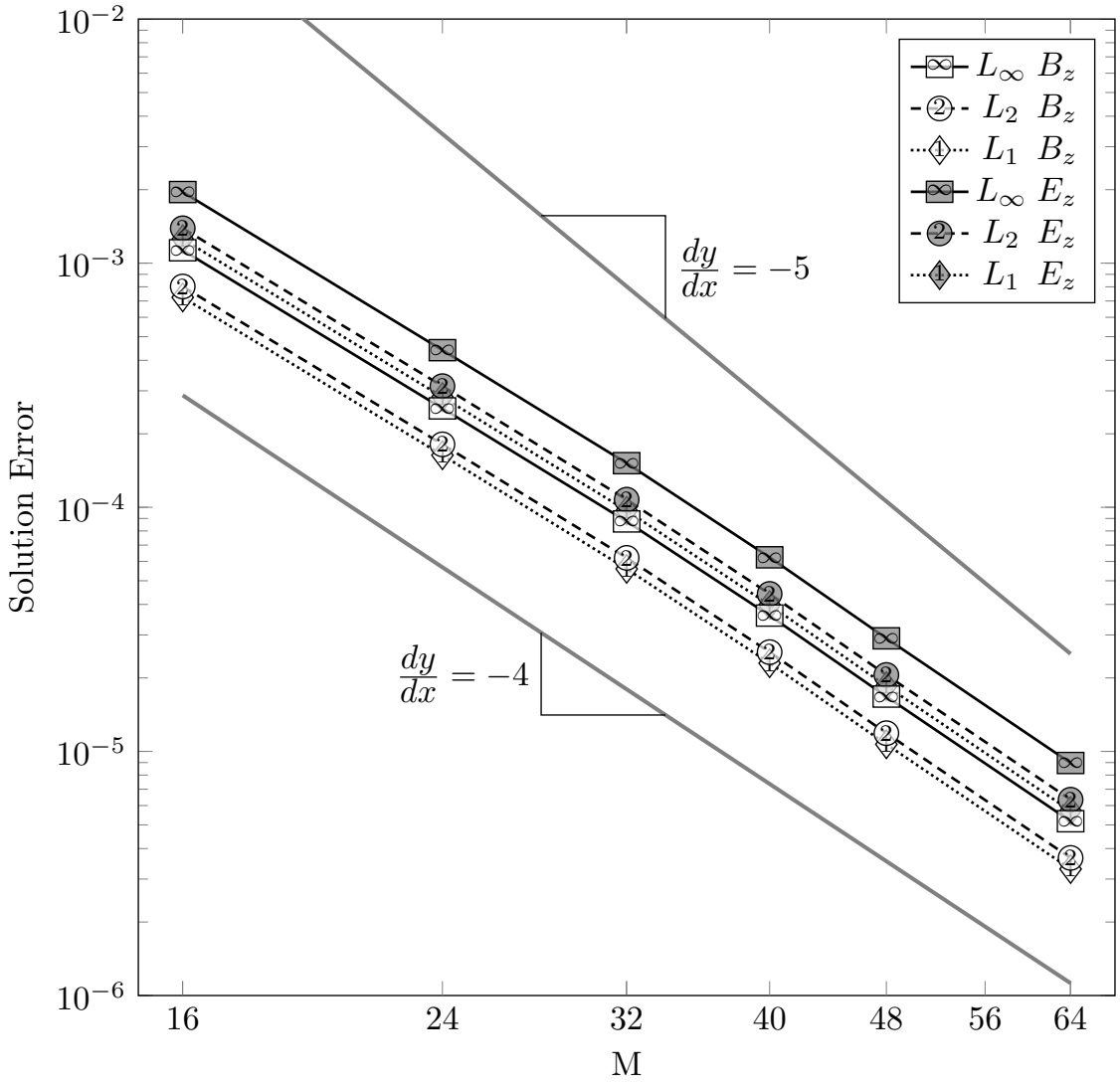

Figure 4.2: Grid convergence rate of L_1, L_2, and L_∞ for variables E_z and B_z from the electromagnetic wave test case, at time 1.2 ns.

Table 4.1: L_p norms (where $p = 1, 2, \infty$) of the electromagnetic solution errors for the 3D plane-polarized electromagnetic wave test case at time 1.2 ns. The convergence rates are computed between consecutive grid resolutions, demonstrating the 4th-order accuracy of the algorithm.

	L_p	24^3	**rate**	32^3	**rate**	40^3	**rate**	48^3	**rate**	64^3
E_y	L_1	2.83E-04	-3.73	9.69E-05	-3.99	3.98E-05	-4.19	1.85E-05	-4.09	5.71E-06
	L_2	3.14E-04	-3.72	1.07E-04	-3.98	4.42E-05	-4.19	2.06E-05	-4.09	6.34E-06
	L_∞	4.40E-04	-3.71	1.52E-04	-3.98	6.24E-05	-4.19	2.91E-05	-4.09	8.96E-06
E_z	L_1	2.83E-04	-3.73	9.69E-05	-3.99	3.98E-05	-4.19	1.85E-05	-4.09	5.71E-06
	L_2	3.14E-04	-3.72	1.07E-04	-3.98	4.42E-05	-4.19	2.06E-05	-4.09	6.34E-06
	L_∞	4.40E-04	-3.71	1.52E-04	-3.98	6.24E-05	-4.19	2.91E-05	-4.09	8.96E-06
B_x	L_1	3.27E-04	-3.73	1.12E-04	-3.99	4.60E-05	-4.19	2.14E-05	-4.09	6.60E-06
	L_2	3.62E-04	-3.72	1.24E-04	-3.98	5.10E-05	-4.19	2.37E-05	-4.09	7.32E-06
	L_∞	5.08E-04	-3.71	1.75E-04	-3.98	7.20E-05	-4.19	3.35E-05	-4.09	1.04E-05
B_y	L_1	1.63E-04	-3.73	5.59E-05	-3.99	2.30E-05	-4.19	1.07E-05	-4.09	3.30E-06
	L_2	1.81E-04	-3.72	6.21E-05	-3.98	2.55E-05	-4.19	1.19E-05	-4.09	3.66E-06
	L_∞	2.54E-04	-3.71	8.75E-05	-3.98	3.60E-05	-4.19	1.68E-05	-4.09	5.18E-06
B_z	L_1	1.63E-04	-3.73	5.59E-05	-3.99	2.30E-05	-4.19	1.07E-05	-4.09	3.30E-06
	L_2	1.81E-04	-3.72	6.21E-05	-3.98	2.55E-05	-4.19	1.19E-05	-4.09	3.66E-06
	L_∞	2.54E-04	-3.71	8.75E-05	-3.98	3.60E-05	-4.19	1.68E-05	-4.09	5.18E-06

4.2 1D Electron Acoustic Wave, One-Harmonic

A dispersion relation, derived from a linearizion of the multi-fluid plasma governing equations, can be used to model an electron acoustic wave in a low-temperature, fully-ionized plasma[55]. The dispersion relation is used to simulate the propagation of a finite, Fourier-series approximation of an initial square wave perturbation in the electron fluid state[19]. Because the dispersion relation provides an analytical solution, the electron acoustic wave test case is a good candidate to verify the order of accuracy and validate the solution of the multi-fluid plasma model infrastructure in Chord. This is a two-fluid problem: electrons (e) and ions (i). In this problem, the solution state, Equation (3.2), is represented as background value ($\mathbf{U}^0$) plus a perturbation ($\mathbf{U}^1$):

$$\mathbf{U} = \mathbf{U}^0 + \mathbf{U}^1. \tag{4.3}$$

Only the inertial terms of the fluid equations are solved, no viscous or heat flux is considered. The electron and ion fluids are both modeled using a calorically-perfect, ideal gas equation of state. The speed of light is prescribed as $c = 1$, with a permittivity $\epsilon_0 = 1$. All solution state background values ($\mathbf{U}^0$) are set to zero, with the following exceptions:

$$\rho_i^0 = m_i n_i^0$$

$$\rho e_i^0 = \frac{P_i^0}{\gamma_i - 1}$$

$$\rho_e^0 = m_e n_e^0$$

$$\rho e_e^0 = \frac{P_e^0}{\gamma_e - 1},$$

where

$$m_i = \infty, m_e = 1$$

$$n_i^0 = n_e^0 = 1$$

$$P_i^0 = P_e^0 = 1$$

$$\gamma_i = \gamma_e = 2.$$

In practice, a very large number is used for the ion mass; for example, $m_i = 10^{10}$. The perturbed values ($\mathbf{U}^1$) are all zero with the following exceptions, which vary in time, t:

$$\rho_e^1 = \sum_{n=0}^{N-1} -\rho_e^0 \frac{u_0}{(2n+1)} \frac{k_n}{\omega_n} \cos\left(k_n x - \frac{\pi}{2} + \omega_n t\right)$$

$$u_e^1 = \sum_{n=0}^{N-1} \rho_e^0 \frac{u_0}{(2n+1)} \cos\left(k_n x - \frac{\pi}{2} + \omega_n t\right)$$

$$P_e^1 = \sum_{n=0}^{N-1} -P_e^0 \gamma_e \frac{u_0}{(2n+1)} \frac{k_n}{\omega_n} \cos\left(k_n x - \frac{\pi}{2} + \omega_n t\right)$$

$$E_x^1 = \sum_{n=0}^{N-1} n_e^0 \frac{u_0}{(2n+1)} \frac{q_e}{\omega_n \epsilon_0} \cos\left(k_n x + \omega_n t\right)$$

$$\rho u_e^1 = \rho_e^0 u_e^1$$

$$\rho e_e^1 = \frac{P_e^1}{\gamma_e - 1} + \frac{1}{2} \rho_e^0 \left(u_e^1\right)^2,$$

where

$$k_n = 2\pi\,(2n+1)$$

$$\omega_n = \sqrt{\gamma_e \frac{P_e^0}{\rho_e^0} k_n^2 + n_e^0 \frac{q_e^2}{\epsilon_0 m_e}}$$

$$u_0 = 1 \times 10^{-8}.$$

The problem is initialized to the background values plus the perturbations at a time of $t = 0$. The number of odd harmonics, N, considered determines the sharpness of the initial square wave perturbation, as shown in Figure 4.3.

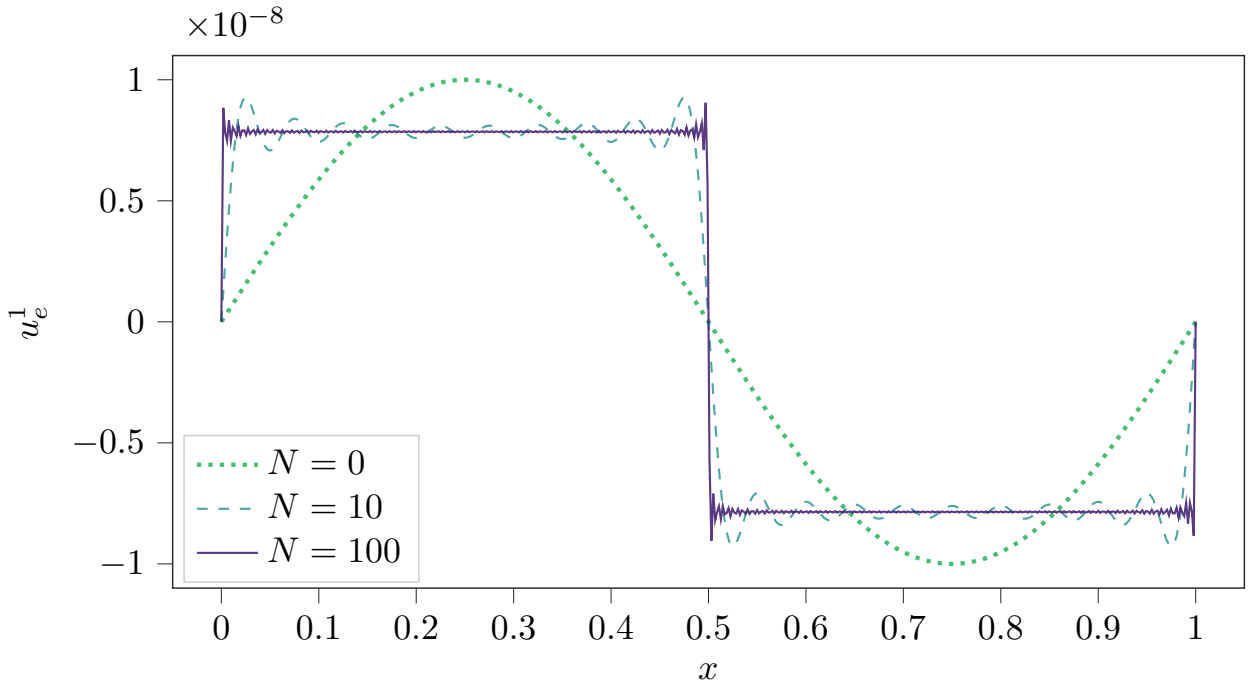

Figure 4.3: Electron acoustic wave problem, initial perturbation to the electron velocity for various numbers of odd harmonics, N

To verify the order of accuracy of the multi-fluid plasma solver in Chord, the smoother, single-harmonic case is simulated in order to avoid utilization of the limiter which can affect the order of accuracy. The simulation is repeated on increasing grid sizes, and the errors of the numerical

results (relative to the exact solution) are analyzed. As shown in Table 4.2 and Figure 4.4, the Chord solution is converging at an error reduction rate of -4, confirming the 4th-order accuracy of the solver.

Table 4.2: L_p norms (where $p = 1, 2, \infty$) of pertinent solution errors for the single-harmonic electron acoustic wave test case at time 3. The convergence rates are computed between consecutive grid resolutions, demonstrating the 4th-order accuracy of the algorithm.

	L_p	**32**	**rate**	**48**	**rate**	**64**	**rate**	**80**	**rate**	**96**
ρ_e	L_1	7.90E-12	-3.98	1.57E-12	-3.99	4.98E-13	-3.99	2.04E-13	-4.01	9.85E-14
	L_2	8.79E-12	-3.99	1.74E-12	-3.99	5.53E-13	-4.00	2.27E-13	-4.01	1.09E-13
	L_∞	1.24E-11	-3.99	2.47E-12	-3.99	7.83E-13	-3.99	3.22E-13	-3.97	1.56E-13
$\rho u_{x\,e}$	L_1	1.67E-11	-3.98	3.32E-12	-3.99	1.05E-12	-4.00	4.31E-13	-3.99	2.08E-13
	L_2	1.86E-11	-3.99	3.68E-12	-3.99	1.17E-12	-3.99	4.79E-13	-3.99	2.31E-13
	L_∞	2.62E-11	-3.99	5.20E-12	-3.99	1.65E-12	-3.99	6.78E-13	-3.99	3.27E-13
ρe_e	L_1	1.58E-11	-3.98	3.14E-12	-3.99	9.96E-13	-4.00	4.08E-13	-4.00	1.97E-13
	L_2	1.76E-11	-3.99	3.49E-12	-3.99	1.11E-12	-4.00	4.53E-13	-4.00	2.19E-13
	L_∞	2.49E-11	-3.99	4.93E-12	-3.99	1.56E-12	-3.99	6.42E-13	-3.99	3.10E-13
E_x	L_1	1.24E-11	-3.98	2.47E-12	-3.99	7.82E-13	-4.00	3.20E-13	-3.99	1.55E-13
	L_2	1.38E-11	-3.98	2.74E-12	-3.99	8.68E-13	-3.99	3.56E-13	-3.99	1.72E-13
	L_∞	1.95E-11	-3.99	3.86E-12	-3.99	1.23E-12	-3.99	5.03E-13	-3.98	2.44E-13

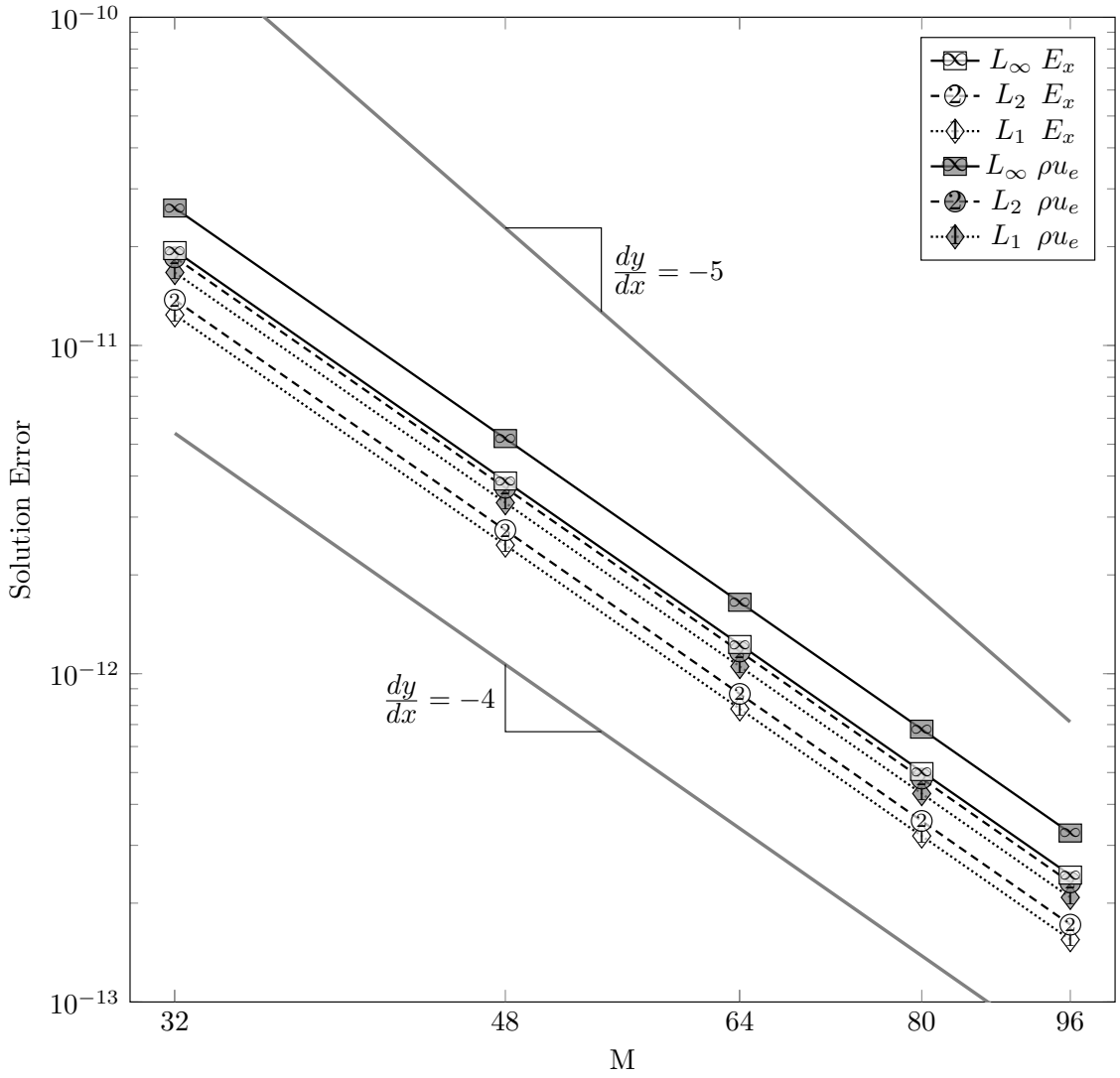

Figure 4.4: Grid convergence rate of L_1, L_2, and L_∞ for variables E_x and ρu_e from a 1-harmonic electron acoustic wave test case at a normalized time of 3. Reference lines with slopes of -4 and -5 are shown adjacent to the error plots to illustrate the 4th-order accurate convergence rate. The x-axis represents mesh size (cell count), M, for each solution.

Chapter 5

Validation

Validation of the multi-fluid plasma model in Chord is performed by solving plasma test problems in Chord and comparing the results to either exact solutions or to experimental data. First we validate the fluid solver and solution-stabilizing features in Chord, as well as a monotonic extrapolation scheme for thermophysical fluid properties, by solving a problem involving the rapid expansion and cooling of a laser-initiated plasma kernel. Next, we independently validate the EM solver in Chord by solving a 2D transmagnetic wave problem. Finally, we use Chord to simulate a 10-harmonic version of the electron acoustic wave to validate all the physics of the fully-coupled multi-fluid plasma model.

5.1 Axisymmetric Plasma Kernel Expansion

The intention of this test case is to assess the stability of the multi-fluid algorithm framework — a fourth-order accurate CFD code with AMR — for problems involving the temperature magnitudes and spatial gradients encountered in plasmas. Furthermore, we seek to develop a solution methodology and to compare our results against the literature.

Many plasmas and plasma systems are cylindrical in nature, and often the plasmas exhibit sufficient azimuthal symmetry that the physics can be accurately represented with a 2D-axisymmetric problem domain. These problems can be solved in the Cartesian coordinate system by analytically rearranging the governing equations, resulting in source terms, **S**, which account for the axisymmetric coordinate. A complete derivation of these geometric source terms can be found in CFD textbooks[56].

Recent work on laser-initiated, plasma-enhance combustion[57] provides relevant test cases for the initial developments of our multi-fluid plasma model. In one such example[57], the 2D-axisymmetric shock expansion of an initial kernel or filament of high-energy gas is modeled and compared to experimental data. Experimentally, the plasma kernel is created by overlapping a pre-

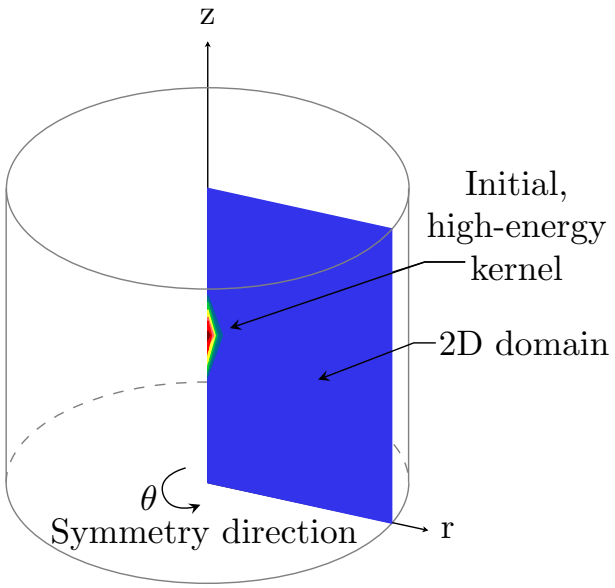

Figure 5.1: An illustration of the laser-initiated plasma kernel problem domain for the test case

ionizing, ultra-violet (UV) laser pulse with a near-infrared (NIR) laser pulse to deposit energy to the plasma, and the resulting shape is a symmetric, elliptical structure. In that study, the initial energy kernel creation is not modeled. Instead, the numerical model begins approximately 500 ns after the pulse. The compressible Navier-Stokes equations were solved, assuming a thermally-perfect ideal gas equation of state. This simplified model does not account for any electrodynamics or charged species; instead, the gas is assumed to be molecular Nitrogen in the ground state. In the present study, we take a similar approach to numerical modeling of the plasma kernel evolution. The 2D-axisymmetric problem domain and initial, high-energy kernel are illustrated in Figure 5.1. This is the computational geometry and domain used in the present study.

5.1.1 Axisymmetric Governing Equations

In the discussion of this laser-plasma kernel test case, we revert to a more familiar nomenclature for the fluid equations in order to be consistent with the reference literature, and also because the more detailed nomenclature and formulation of the governing equations used in Chapters 2 and

3 are better suited for problems involving multiple, charged species. Simplifying the governing equations (3.1) in 2-D axisymmetric problem space, for a single, neutral species, results in the following solution vector

$$\mathbf{U} = \left[\rho, \rho u_r, \rho u_z, \rho e\right]^T, \tag{5.1}$$

hyperbolic flux,

$$\vec{\mathbf{F}} = \begin{bmatrix} \begin{bmatrix} \rho u_r \\ \rho u_r^2 + p \\ \rho u_r u_z \\ \rho u_r \left(e + p/\rho\right) \end{bmatrix}, \begin{bmatrix} \rho u_z \\ \rho u_r u_z \\ \rho u_z^2 + p \\ \rho u_z \left(e + p/\rho\right) \end{bmatrix} \end{bmatrix}, \tag{5.2}$$

viscous (elliptical) flux,

$$\vec{\mathbf{G}} = \begin{bmatrix} \begin{bmatrix} 0 \\ \tau_{rr} \\ \tau_{rz} \\ u_r\tau_{rr} + u_z\tau_{rz} - \phi_r \end{bmatrix}, \begin{bmatrix} 0 \\ \tau_{rz} \\ \tau_{zz} \\ u_r\tau_{rz} + u_z\tau_{zz} - \phi_z \end{bmatrix} \end{bmatrix}, \tag{5.3}$$

and source terms,

$$\mathbf{S} = -\frac{1}{r}\begin{bmatrix} \rho u_r \\ \rho u_r^2 - \tau_{rr} \\ \rho u_r u_z - \tau_{rz} \\ \rho u_r \left(e + p/\rho\right) - u_r\tau_{rr} - u_z\tau_{rz} + \phi_r \end{bmatrix}. \tag{5.4}$$

In this simplified case of a single, neutral species, there are no source terms to account for collisions or reactions. Instead, the vector of source terms (5.4) represents the transformation between

the Cartesian coordinate version of the conservation equations and a 2D-axisymmetric coordinate system.

5.1.2 Boundary Conditions and Initialization

The z axis in Figure 5.1 represents the symmetry axis (i.e. the axis of rotation). From a boundary condition perspective, this z-axis edge of the 2D domain is modeled as a slip boundary. This boundary treatment prescribes a zero velocity in the r direction, but does not inhibit or dictate the z direction velocity, which is reconstructed from adjacent cells. The three other edges of the problem domain are also modeled as slip wall boundaries; however, the domain is sized with the intention that the shock propagation does not reach any boundaries within the time range of interest.

The 2D domain size is 16 mm in the r direction and 32 mm in the z direction (Figure 5.1). The initial kernel of high-energy described in the reference[57] is 2 mm long (z direction) and has a minor radius of 0.5 mm (r direction) resulting in a length to width aspect ratio of 2:1. The shape of the initial kernel is described as an ellipse superimposed on an elongated rectangle or diamond shape. After the initial kernel shape is constructed, the pressure and temperature inside the kernel are set to 2.2×10^7 Pa and 35,000 K, respectively. Outside the kernel, the remainder of the domain is initialized to 101,325 Pa and 300 K. The only gas species considered in this test case is diatomic Nitrogen, N_2, in the ground state. Finally, a circular-averaging (pillbox) filter method is applied to the problem domain, with a filter radius of 0.25 mm, to smooth the sharp discontinuities at the kernel edges. A contour plot of the kernel initialization is shown in Figure 5.2.

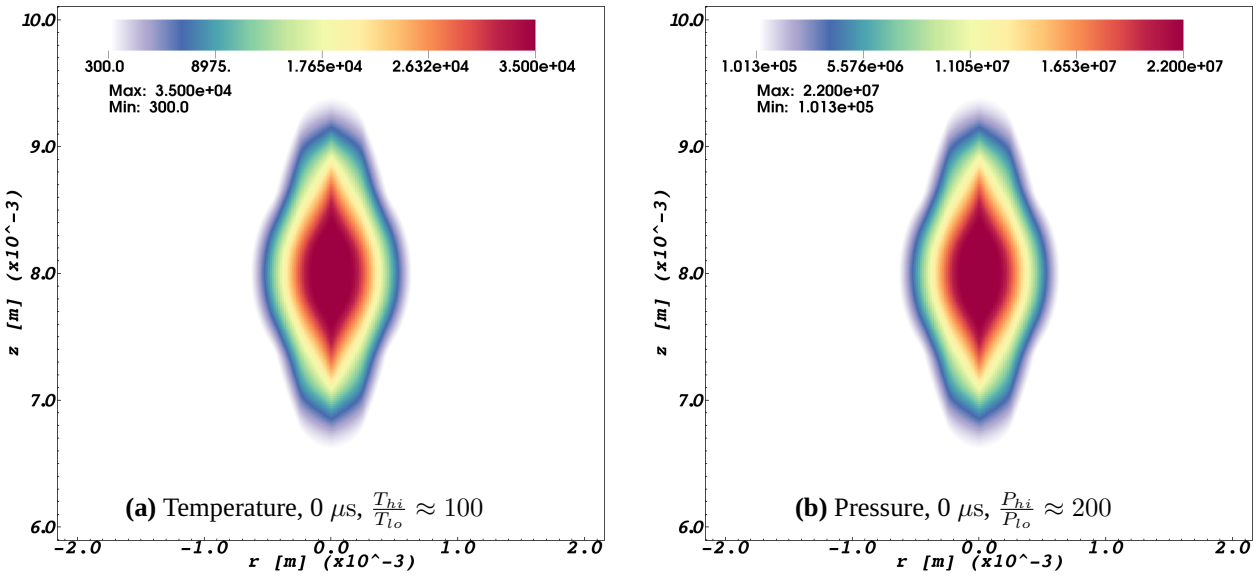

(a) Temperature, 0 μs, $\frac{T_{hi}}{T_{lo}} \approx 100$

(b) Pressure, 0 μs, $\frac{P_{hi}}{P_{lo}} \approx 200$

Figure 5.2: Initial conditions for the high-energy laser-initiated plasma kernel. Spatial scaled is zoomed in relative to the problem domain.

5.1.3 Transport and Thermodynamic Properties

The initial temperature in the high-energy kernel, 35,000 K, is far beyond any useful tables or constitutive models for transport or thermodynamic coefficients of gases. In fact, at those temperatures, the Nitrogen molecules would exhibit a significant level of dissociation into atomic Nitrogen as well as thermal ionization. However, the goal of this work is to establish solution methods for problems involving strong discontinuities commonly found in plasmas and laser excitations of gas, so the chemical and charge complexities of the gas are neglected in the present study. Similar assumptions were made in the reference literature[57].

Thermodynamic and transport data are based on the coefficients and polynomials published by NASA Glenn Research Center[58]. For Nitrogen, these tables provide transport coefficients up to 15,000 K and thermodynamic coefficients up to 20,000 K. The polynomial for thermal conductivity — based on coefficients at 15,000 K — is monotonic and stable when extrapolated between 15,000 K – 35,000 K, so the high-temperature coefficients for κ were used without modification inside the high-temperature kernel. Some literature suggests the viscosity of Nitrogen at temperatures between 15,000 K – 35,000 K is relatively consistent[59], so in our model we have held the viscosity

constant over this entire high-temperature range, based on the value of μ at 15,000 K. The results of the ultra-high temperature transport property models are shown in Figure 5.3.

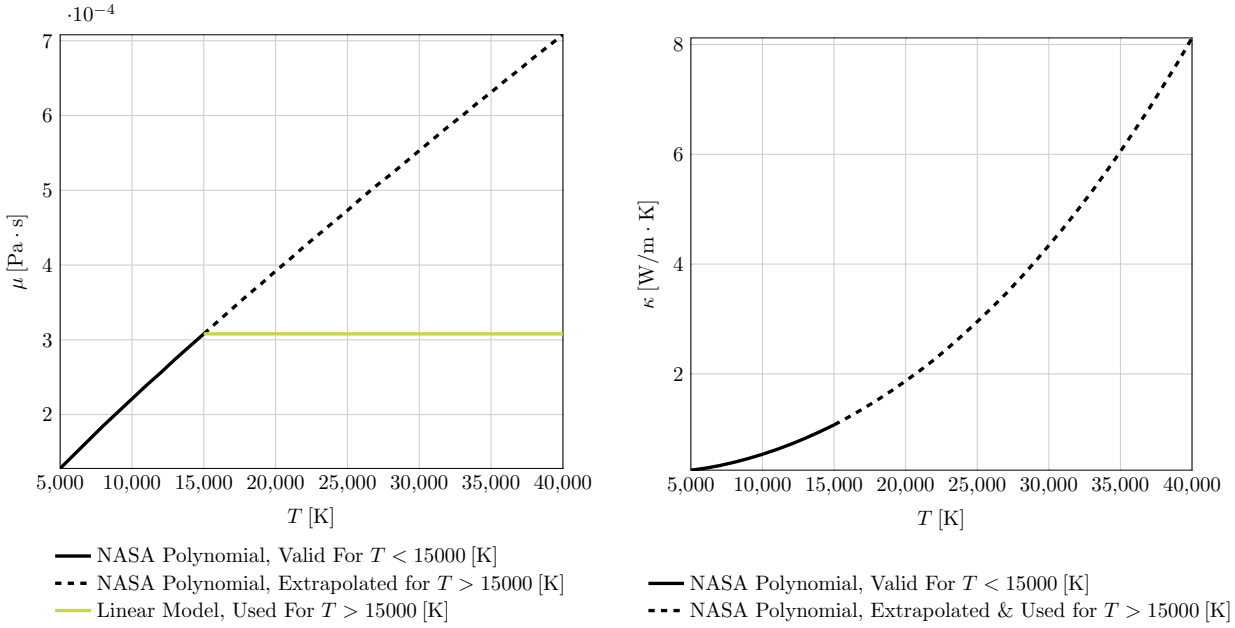

Figure 5.3: Extrapolation model for ultra-high temperature transport properties

At temperature values above 15,000 K, the Prandtl number for air tends to remain approximately 0.3, so we assume this trend also applies for Nitrogen[59]. However, extending the specific heat equation, $C_p\,(T)$ beyond the maximum temperature range from the NASA tables results in a highly nonlinear relationship with temperature, and the resulting C_p values, combined with extrapolated values for μ and κ, yield Prandtl numbers that are excessively high. Therefore, a new model for specific heat was constructed for temperatures above 20,000 K. This model assumes a linear relationship with temperature, with a slope that approximately results in a Prandtl number of 0.3 over the temperature range of 20,000 – 35,000 K. Results of the high-temperature thermodynamic property extrapolation are shown in Figure 5.4.

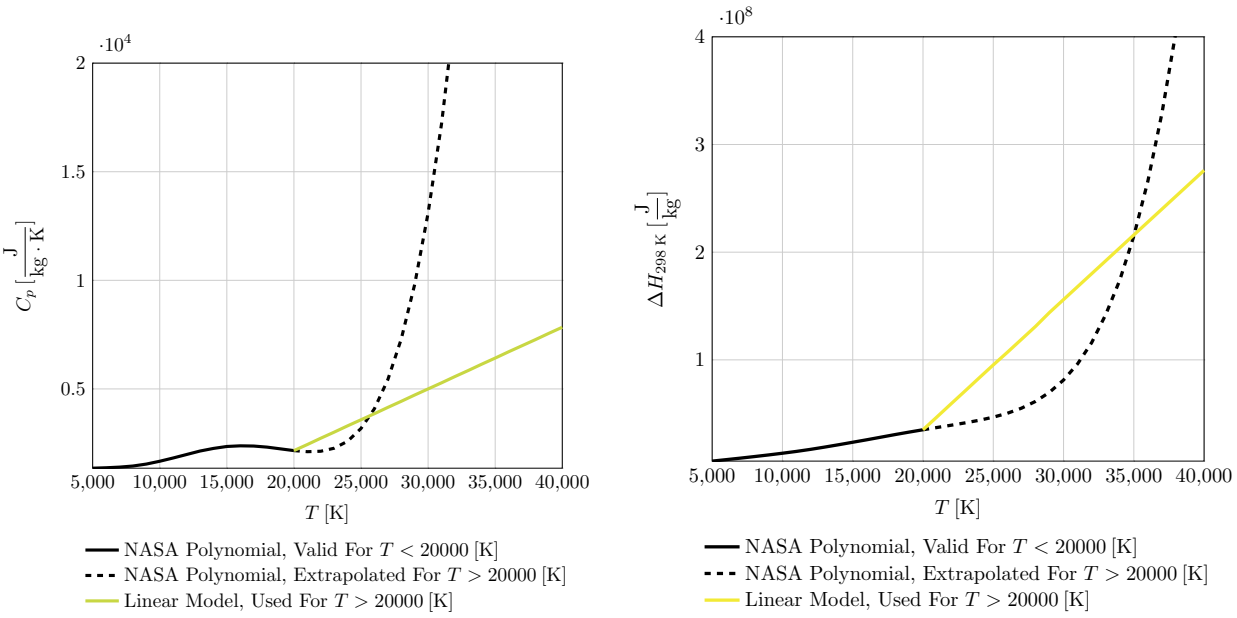

Figure 5.4: Extrapolation model for ultra-high temperature thermodynamic properties

5.1.4 Solution Methodology

For a significant duration of the transient solution, the majority of the problem domain is quiescent. In order to promote computational efficiency in these undisturbed regions, a coarse resolution is specified for the top-level mesh. As the solution progresses, the decision on whether to refine the mesh is based on pressure and density gradients. Cells are tagged for refinement if the gradients in density or pressure spanning the cell exceed some predetermined threshold for each variable. For the simulation presented here, the tagging thresholds of 0.1 – 0.01 were found to provide a good balance between refinement and solution efficiency. Also, in the current simulation, four levels of mesh refinement were employed, each level with twice the mesh resolution as the previous level. As a result, the cell sizes vary between 125 μm on the coarsest grid to approximately 8 μm on the finest grid.

The standard fourth-order Runge-Kutta scheme is used to evolve the solution in time. To ensure stability during the iterative solution, both convective and diffusive fluxes (and the corresponding wave speeds), as well as the source terms need to be considered when determining a time step size. Eigensystem analysis of the source term Jacobian matrix reveals maximum wave speeds of the

radial velocity component, u. In the case of this laser-induced plasma kernel, it is the convective wave speeds that dominate the propagation of error terms through the domain. Therefore, the time step is determined at each iteration of the nonlinear solution, based on the maximum wave speed of the hyperbolic flux terms and a prescribed CFL number. For the simulations presented in this work, CFL numbers in the range 0.50-0.75 were used.

5.1.5 Results and Discussion

The most volatile conditions in the simulation occur within 1.0 μs, when the initial high pressure region rapidly expands past the region of high temperature. Compression waves coalesce around the perimeter, driving high density shock wave along the front of the expansion bubble. The leading edge of the expansion bubble are where the gradients are highest, and the mesh is actively refined in this region, as shown in Figure 5.5. Furthermore, having a highly-refined mesh along the surface of the expansion bubble allows for the shock discontinuity to be captured with a sharp, non-oscillatory edge, as shown in subfigure (b) of Figure 5.6. Additionally, line plots showing the pressure and temperature values in the r direction, through the center of the kernel, are shown for multiple times in Figure 5.6.

The transient response of the initial high-energy kernel in time is illustrated in Figure 5.7. Around 4-5 μs, the high-temperature region begins to collapse inward along the z axis, rapidly cooling the center, eventually producing a toroidal shape as shown in Figure 5.8. Also around 4-5 μs, the high-pressure has evacuated the initial kernel, leaving behind a region of high temperature which is propagating on a slower time scale due to thermal diffusion. During this time, the density inside the expansion bubble becomes lower than the surrounding conditions.

After the initial shock formation and rapid outward convection, the thermodynamic evolution of the high-temperature kernel left behind occurs on a much slower timescale. As time progresses, the simulation predicts a similar kernel structure compared to experimental results; however, the temporal response of the simulation is roughly twice as slow as captured in the experimental results. Clearly, this is due — at least in part — to the gross simplifications in physics we have made

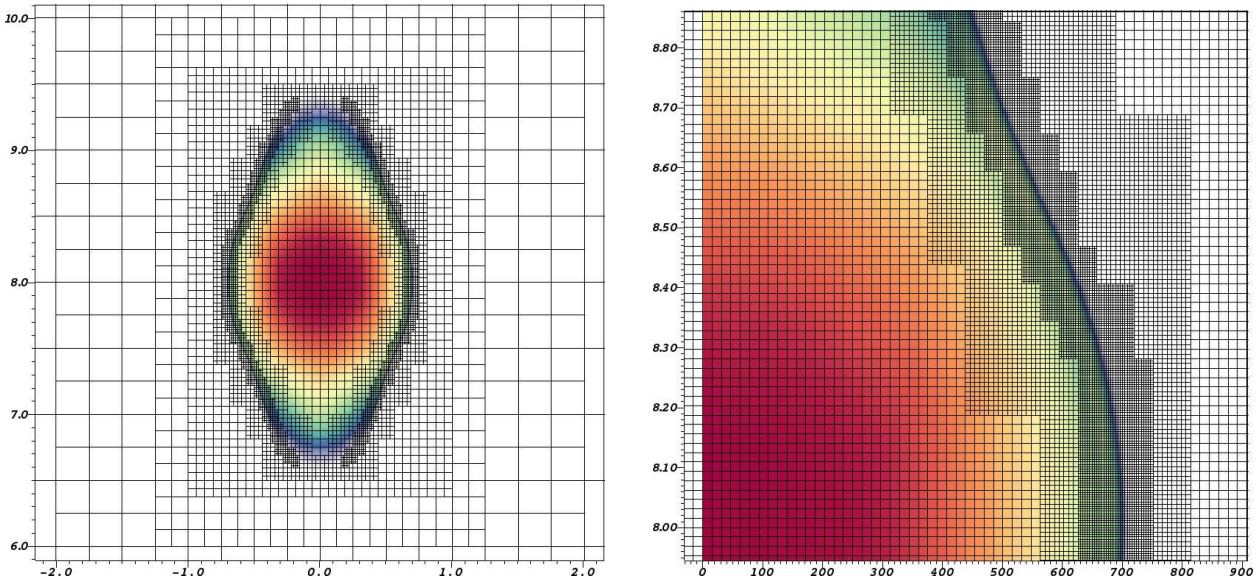

(a) Pressure, 0.1 μs **(b)** Pressure, 0.1 μs, zoomed in NE quadrant

Figure 5.5: Example of solution-adaptive mesh refinement, with tagging thresholds of 0.2 for both pressure and density and 5 levels of AMR. Contour plots show pressure at 0.1 μs. Only one in four actual mesh lines are shown in subfigure (a) to enhance clarity in the figure.

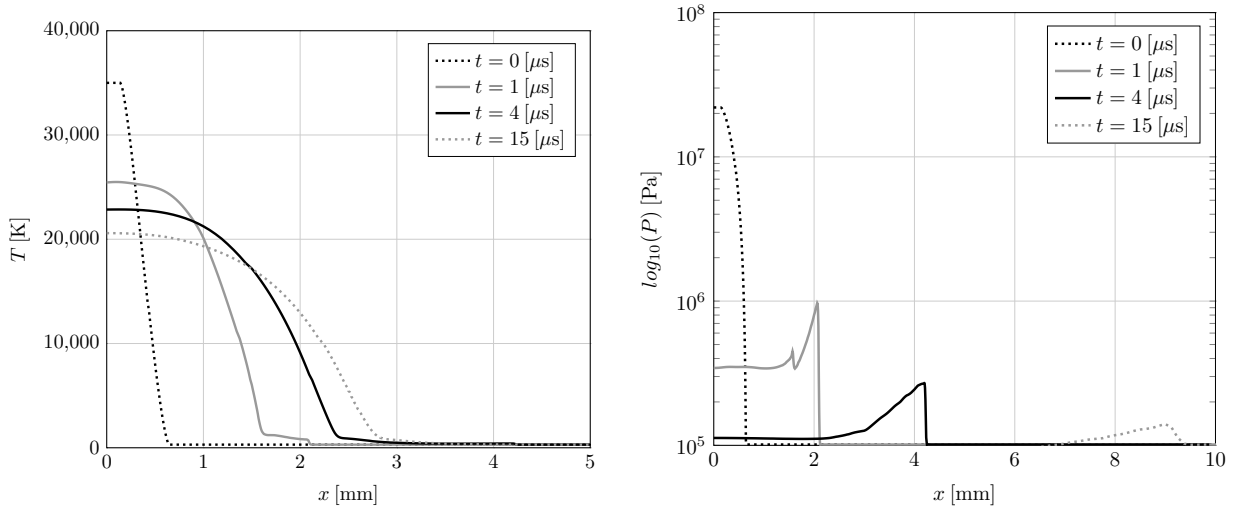

(a) Temperature **(b)** Pressure

Figure 5.6: Temporal evolution of high-energy kernel. Spatial scaled is zoomed in for temperature plot.

regarding the high-temperature properties and characteristics of the fluid. It will be interesting in future work to include more relevant physics, accounting for the presence of charged, excited, and atomic species.

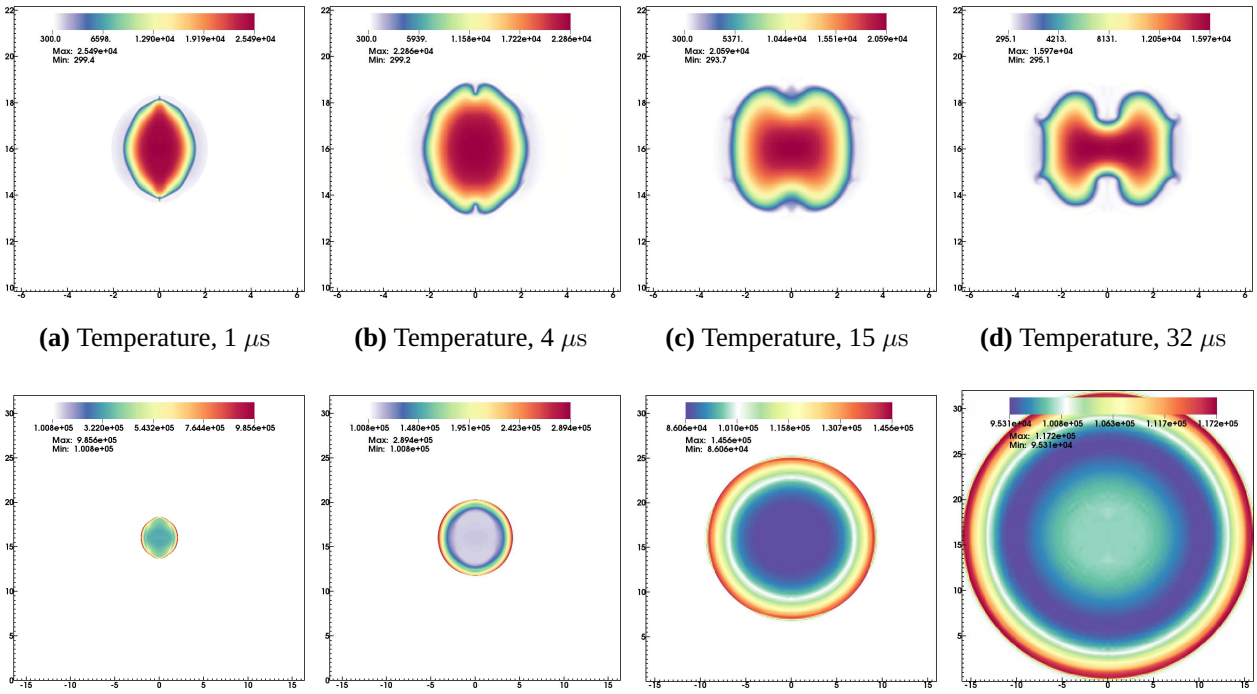

(a) Temperature, 1 μs **(b)** Temperature, 4 μs **(c)** Temperature, 15 μs **(d)** Temperature, 32 μs

(e) Pressure, 1 μs **(f)** Pressure, 4 μs **(g)** Pressure, 15 μs **(h)** Pressure, 32 μs

Figure 5.7: Simulation results at four steps. Spatial scale is zoomed in for temperature plots.

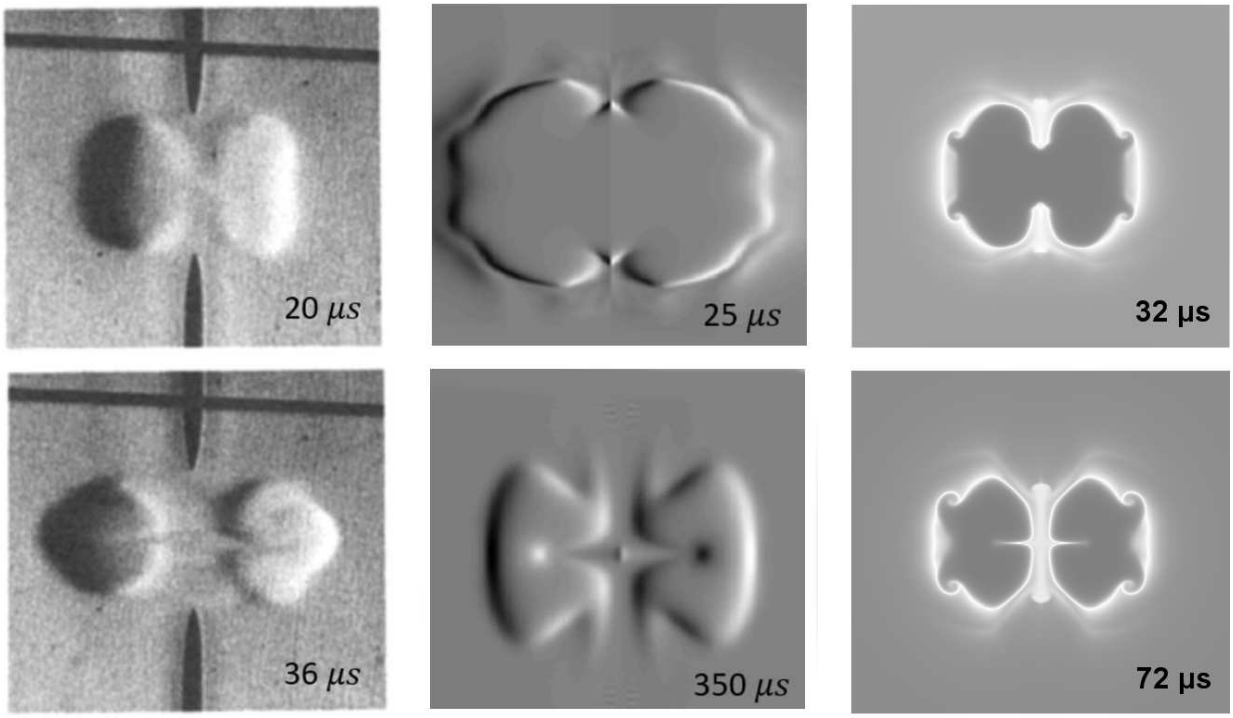

(a) Experimental data, Schlieren photos[60]

(b) 2nd-order accurate CFD model, synthetic Schlieren plots[57]

(c) Current work, density plots with a diverging colormap

Figure 5.8: Comparing thermodynamic kernel evolution between the current work and results from literature

5.2 2D Transmagnetic Wave

Another class of electromagnetic test cases with exact solutions are the various waveguide modes: transverse magnetic (TM), transverse electric (TE), and transverse electromagnetic (TEM). In particular, a TM wave simulation considered in previous literature[36] provides a relevant validation test for our current work. In this test case, a rectangular, two-dimensional plane represents a cross-section of a waveguide. The domain size is $L_x = 80\,\mathrm{m}$ and $L_y = 40\,\mathrm{m}$. The wavenumbers are given by

$$a = \frac{m\pi}{L_x} \qquad\qquad b = \frac{n\pi}{L_y}, \tag{5.5}$$

where $m = 8$, $n = 5$. The net wave travels in the z direction, oscillating at the cutoff frequency, ω. The exact solution for this problem is given by equations (5.6) – (5.8),

$$E_z = \Re(E_0 \sin(ax) \sin(by) e^{-j\omega t}), \tag{5.6}$$

$$B_x = \Re(-j\frac{b}{\omega} E_0 \sin(ax) \cos(by) e^{-j\omega t}), \tag{5.7}$$

$$B_y = \Re(j\frac{a}{\omega} E_0 \cos(ax) \sin(by) e^{-j\omega t}), \tag{5.8}$$

where $\Re$ denotes the real component of the complex expressions, j is the imaginary unit, and E_0 is the initial electric field value ($1\,\mathrm{V/m}$ in our test case).

The TM wave problem is modeled with PEC boundary conditions and initialized using the analytical solution data at time $t = 0$. The divergence cleaning potentials are both initialized to zero. The wave speed scalars used on the divergence cleaning potentials Ψ and Φ are $\lambda = 1.0$ and $\chi = 0.0$, respectively. The solution is advanced in time using a CFL number of 0.8 based on the EM wave propagation speed (the speed of light).

The scalar electric field, E_z oscillates in time according to the analytical solution and numerical damping of the magnitude is minimized by the 4th-order algorithm as shown in Figure 5.9. Line samples of the simulation results at $75\,\mathrm{ns}$ compare well with the exact solution, as shown in

Figure 5.10, and are also consistent with higher-order, numerical methods used in previous literature[36]. As the solution advances in time, the initial electric field gradients drive the evolution of rotating magnetic fields (Figure 5.11). The shape and magnitudes of the magnetic fields are symmetric and also appear to free from adverse affects from the physical boundary.

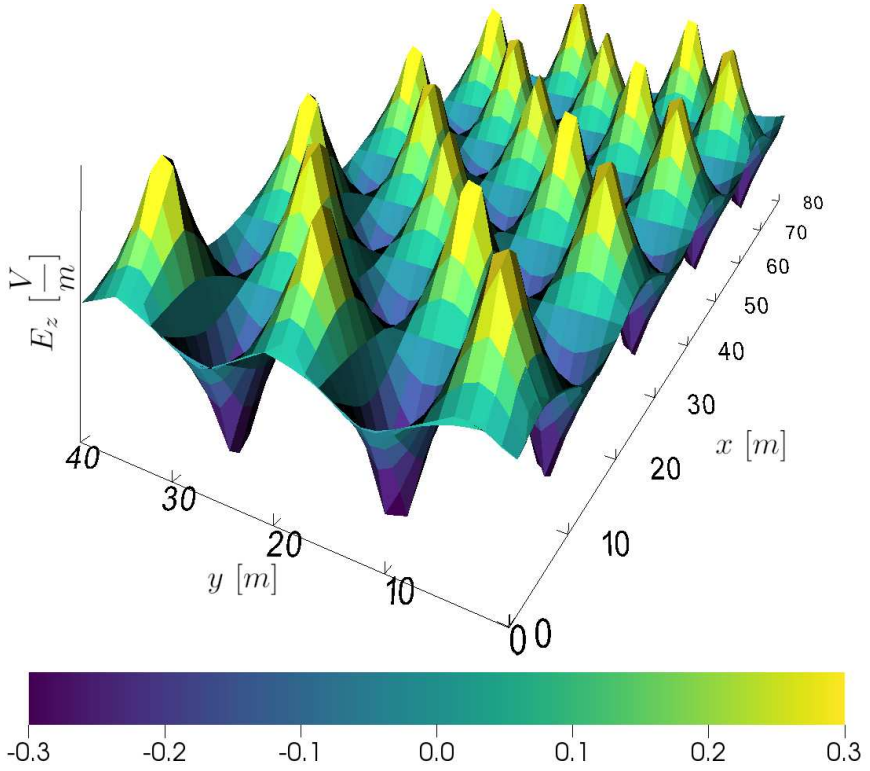

Figure 5.9: Transverse magnetic wave solution for scalar electric field E_z with $m = 8$ and $n = 5$, at solution time 75 ns on a 64×32 mesh.

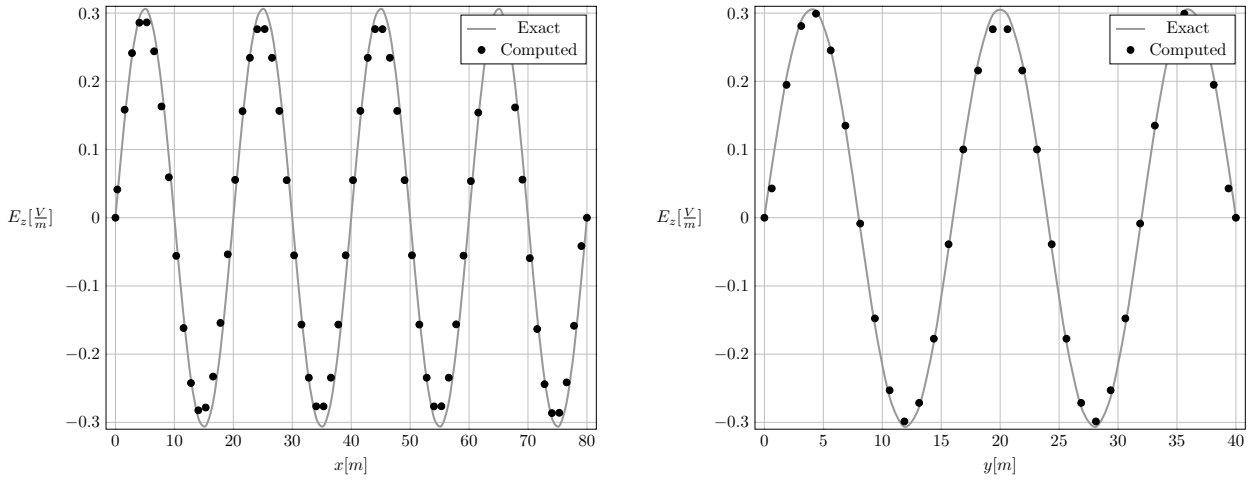

Figure 5.10: Comparison of numerical results for the TM wave calculation on a 64×32 mesh, with $m = 8$ and $n = 5$, at solution time 75 ns. Left plot shows E_z at $y = 20$ m and right plot shows E_z at $x = 25$ m. The numerical results (black marks) show good agreement with the exact solution (solid lines).

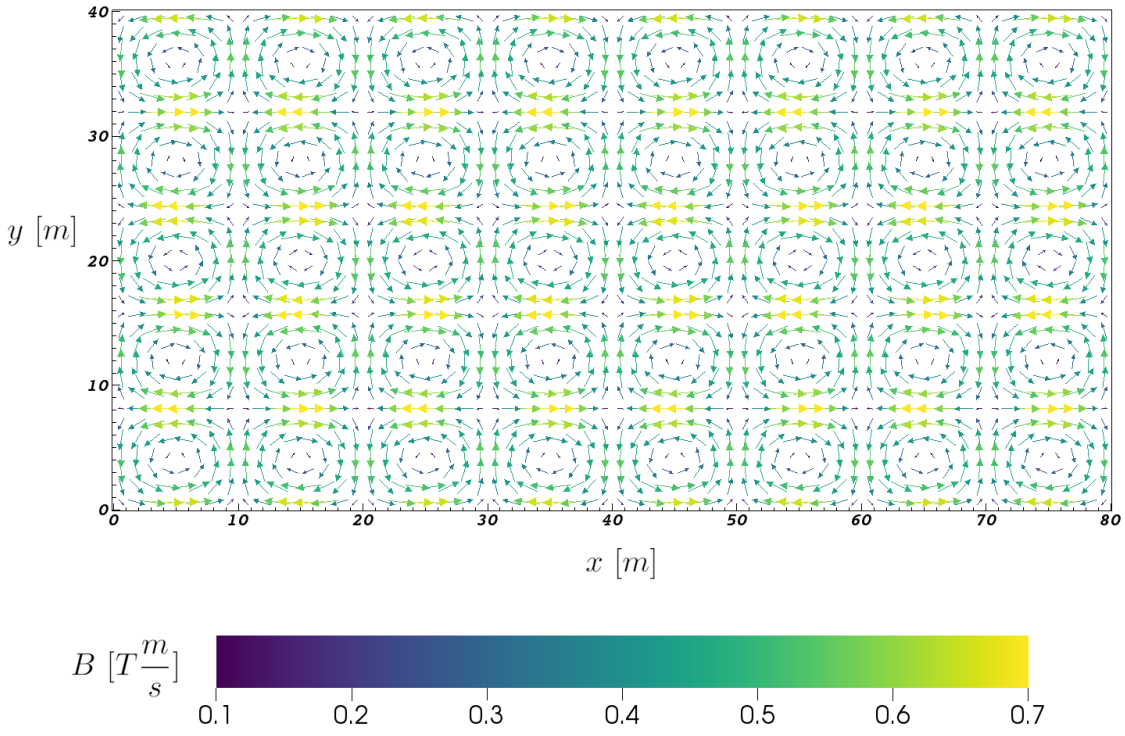

Figure 5.11: Transverse magnetic wave solution for magnetic field $\vec{B}$ with $m = 8$ and $n = 5$, at solution time 75 ns on a 64×32 mesh.

5.3 1D Electron Acoustic Wave, 10-Harmonics

To validate the solution produced by the multi-fluid plasma algorithm in Chord, the electron acoustic problem from Section 4.2 is solved for a 10-harmonic ($N = 10$) case to a time of 3. The numerical algorithm handles the initial discontinuity well and produces a solution that precisely aligns with the exact solution, as shown in Figure 5.12.

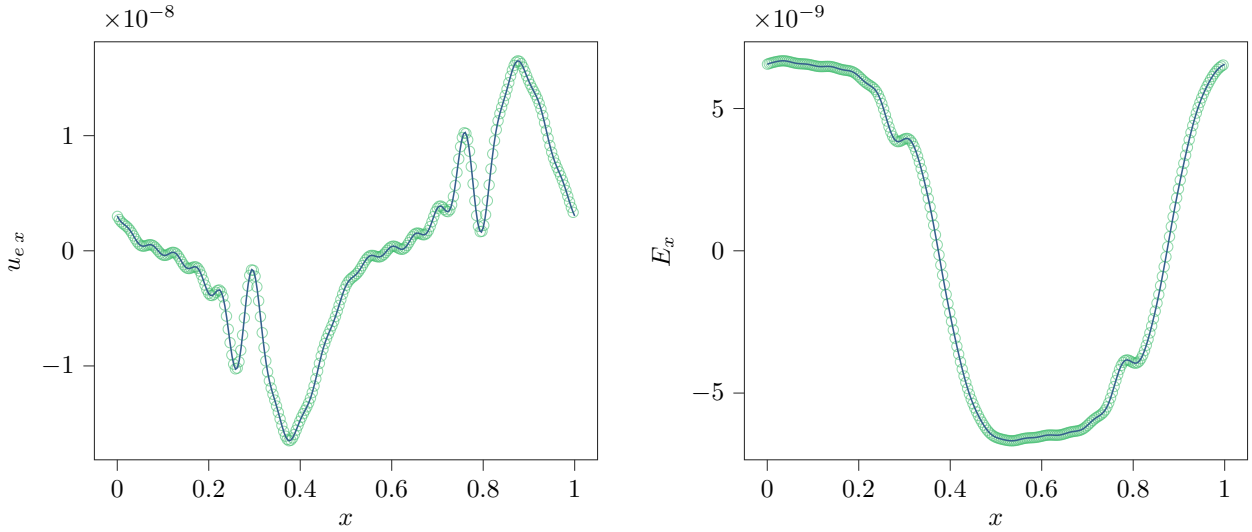

Figure 5.12: Electron acoustic wave results, 10-harmonic case, at a normalized time of 3. The solution from Chord (lighter markers) is compared to the exact solution (darker, solid line). The plot on the left shows electron velocity and the plot on the right shows the x-component of the electric field. The Chord solution is using a 4th-order accurate algorithm with a fixed mesh size of 1024. The marker density for the Chord solution has been reduced by a factor of 1/4 to improve clarity.

Chapter 6

Simulation Results and Discussion

With a fully verified and validated algorithm, the next step is to compare simulations of common plasma tests cases in Chord with results from the literature. In the process, there are further opportunities to explore AMR configurations and solution-stabilizing methods. The test cases considered herein are an electromagnetic refractive disk, a 1D magnetic shock tube, the GEM magnetic reconnection challenge problem, and a 2D plasma blast explosion problem.

6.1 Refractive Scattering of an Electromagnetic Pulse

We adapt a problem from Balsara et al.[61] to demonstrate spatially-varying material properties in Chord and to test our implementation of zero-gradient boundary conditions on the electromagnetic variables; this is a test of our electromagnetic solver only, not the full, multi-fluid plasma model.

6.1.1 Problem Setup

In this problem, a compact electromagnetic pulse with a Gaussian taper travels obliquely through a square, two-dimensional domain bound by $[-7.0, 7.0] \times [-7.0, 7.0]\ \mathrm{m}$. In the center of the domain is a dielectric disk with a radius of $0.75\ \mathrm{m}$. The permeability in the domain is constant, set to $\mu = \mu_0 = 4\pi \times 10^{-7}\ \mathrm{N\,A^{-2}}$, and a permittivity specified as

$$\epsilon\left(x, y\right) = \epsilon_0 \left(5.0 - 4.0 \tanh\left(\frac{\sqrt{x^2 + y^2} - 0.75}{0.08}\right)\right), \tag{6.1}$$

where $\epsilon_0 = 8.8542 \times 10^{-12}\ \mathrm{F\,m^{-1}}$. Thus, the speed of light is also spatially varying, $c = 1/\sqrt{\epsilon\left(x, y\right)\mu}$. In the lower left corner of the domain, an initial electromagnetic pulse is specified, with a Gaussian taper in both transverse and longitudinal directions. The magnetic and electric field components of

this initial pulse are specified as

$$E_x = c\left(\frac{w_1\,(y-b)\,C_2\sin\left(C_1\right)}{\sqrt{2}\,\pi w_2^2} - \frac{C_2\cos\left(C_1\right)}{\sqrt{2}}\right) \tag{6.2}$$

$$E_y = -c\left(\frac{w_1\,(x-a)\,C_2\sin\left(C_1\right)}{\sqrt{2}\,\pi w_2^2} + \frac{C_2\cos\left(C_1\right)}{\sqrt{2}}\right) \tag{6.3}$$

$$B_z = C_2\cos\left(C_1\right) - w_1\frac{(x-a)\,C_2\sin\left(C_1\right)}{\pi w_2^2}, \tag{6.4}$$

with the following substitution variables and model parameters

$$C_1 = 2\pi\frac{x+y}{w_1} \tag{6.5}$$

$$C_2 = e^{\frac{-(y-b)^2-(x-a)^2}{w_2^2}} \tag{6.6}$$

$$a = b = -2.5\ \mathrm{m} \tag{6.7}$$

$$w_1 = w_2 = 1.5\ \mathrm{m}. \tag{6.8}$$

All other solution variables are initialized to zero, including the divergence correction potentials Φ and Ψ. The divergence correction wave speed scalars are set to $\chi_E = \chi_B = 1.1$. The mesh is specified as 64×64 coarse grid cells, and AMR is applied to this problem, with 2 levels of refinement and a refinement ratio of 2 between each level. Cells are tagged for refinement based on the amplitude of the B_z component, with a threshold of $|B_z| \geq 0.3$. The initialized domain with an illustration of the refractive disk are shown in Figure 6.1. A time step of 0.1 ns is used.

6.1.2 Results and Discussion

As the solution evolves in time, the electromagnetic pulse travels obliquely through the domain at a 45° angle. When the pulse interacts with the higher-permittivity disk in the middle of the domain, the pulse wavelength compresses and the wave velocity slows as it passes through the circular disk, while the portions of the pulse outside of the refractive disk continue to propagate

unimpeded. As a result, the waveform develops a wake around the disk, as shown in Figure 6.2. Interaction with the refractive media also causes the generation of error in the divergence correction term, Φ. Because the wave-speed scalar χ_E is greater than unity, the values of Φ propagate and leave the domain faster than the electric and magnetic field information. By tagging on the amplitude of the B_z component, the mesh is adaptively refined in and around the refractive disk, and areas of the solution with steep gradients and higher detail are meshed with higher resolution. This adaptive refinement is visualized in Figure 6.2. Mesh refinement based on waveform amplitude is effective in this problem and provides improvements in computational efficiency compared to a fixed-size mesh. However, a more robust tagging method might be based on wavelength instead of amplitude; this type of tagging is not currently available in Chord, but is something we are considering for future work.

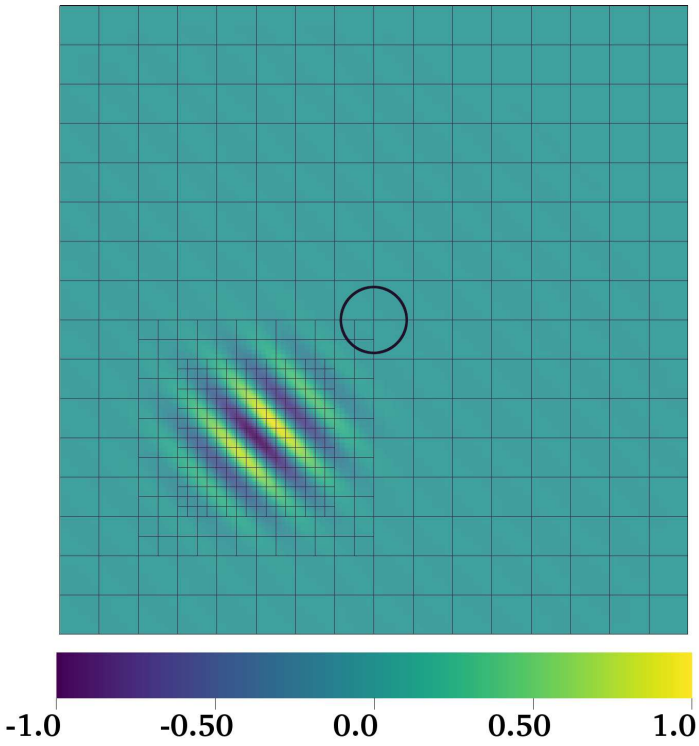

Figure 6.1: Initialization of the z component of the magnetic field, B_z. Units are in T or $\mathrm{kg\,A^{-1}\,s^{-2}}$. A circle is superimposed on the plot to illustrate the refractive disk in the middle of the domain, with permittivity as defined by Equation (6.1). The initial mesh is shown, with refinement triggered by the amplitude of the B_z term.

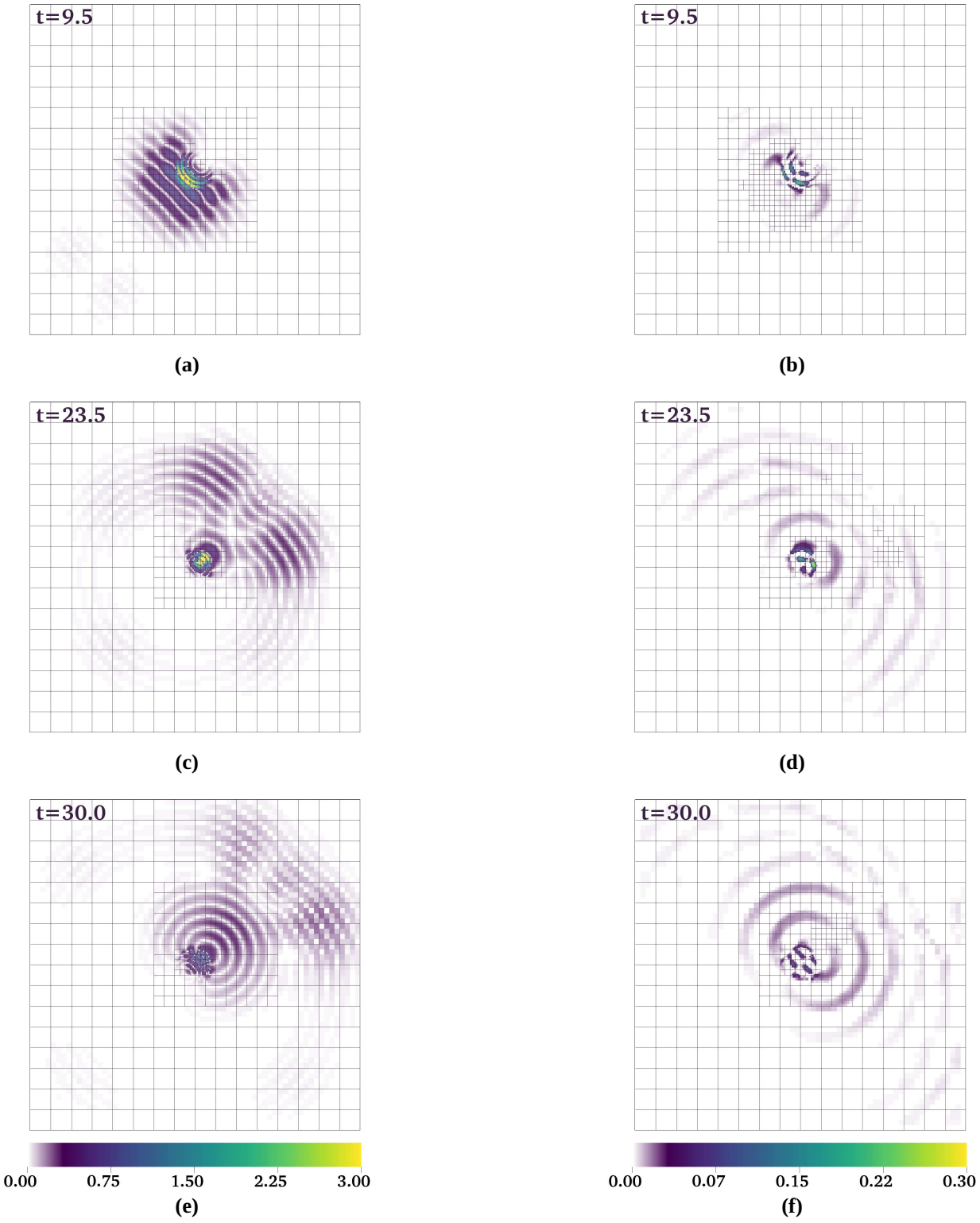

Figure 6.2: Results from a Gaussian-tapered, electromagnetic pulse incident on a refractive disk, at various times as indicated (in units of ns). The left column of plots show the magnitude of the magnetic field in units of T or $\mathrm{kg\,A^{-1}\,s^{-2}}$, and the right column shows the magnitude of the divergence correction potential, Φ, also in units of T or $\mathrm{kg\,A^{-1}\,s^{-2}}$.

6.2 1D Magnetic Shock Tube

The classic, Brio-Wu magnetic shock tube problem[62] has been studied extensively using both MHD and multi-fluid algorithms, which makes it a good candidate to demonstrate the capabilities of Chord in resolving shock waves with efficiency and accuracy.

6.2.1 Problem Setup

The electron and ion fluids are both modeled using a calorically-perfect, ideal gas equation of state with both $\gamma_i = 5/3$ and $\gamma_e = 5/3$, and similar to the previous test cases, only the inertial terms of the fluid equation are considered. The speed of light is prescribed as $c = 1$, with a permittivity $\epsilon_0 = 1$. A realistic ion to electron mass ratio is maintained, $m_i/m_e = 1836$, and the ion and electron charges are set to $q_i = -q_e = 1$. The problem is solved on a one-dimensional grid spanning a nondimensionalized domain of $x \in [0, 1]$. There is an initial discontinuity in the domain at position 0.5, dividing the domain into left and right states, which are initialized with the following values:

$$\begin{bmatrix} \rho_i \\ \rho_i \vec{u}_i \\ \rho_i e_i \\ \rho_e \\ \rho_e \vec{u}_e \\ \rho_e e_e \\ \vec{E} \\ \Psi \\ B_x \\ B_y \\ B_z \\ \Phi \end{bmatrix}_{left} = \begin{bmatrix} 1.0 \\ 0 \\ \frac{5\times10^{-5}}{\gamma_i - 1} \\ 1.0\frac{m_e}{m_i} \\ 0 \\ \frac{5\times10^{-5}}{\gamma_e - 1} \\ 0 \\ 0 \\ 0.75 \times 10^{-2} \\ 1.0 \times 10^{-2} \\ 0 \\ 0 \end{bmatrix} \qquad \begin{bmatrix} \rho_i \\ \rho_i \vec{u}_i \\ \rho_i e_i \\ \rho_e \\ \rho_e \vec{u}_e \\ \rho_e e_e \\ \vec{E} \\ \Psi \\ B_x \\ B_y \\ B_z \\ \Phi \end{bmatrix}_{right} = \begin{bmatrix} 0.125 \\ 0 \\ \frac{5\times10^{-6}}{\gamma_i - 1} \\ 0.125\frac{m_e}{m_i} \\ 0 \\ \frac{5\times10^{-6}}{\gamma_e - 1} \\ 0 \\ 0 \\ 0.75 \times 10^{-2} \\ -1.0 \times 10^{-2} \\ 0 \\ 0 \end{bmatrix} \tag{6.9}$$

This problem uses 1st-order, zero-gradient boundary conditions. It has been previously demonstrated that the ion inertial length factors significantly into the characteristics of the magnetic shock tube solution[18–20,23]; this is studied in the present work by varying the ion mass m_i.

6.2.2 Results and Discussion

An initial investigation was performed to understand the grid requirements for the various discretization algorithms in Chord; in particular, we were interested in comparing the grid requirements for the 4th-order and 2nd-order algorithms in Chord. To demonstrate the accuracy of the Chord solution, the results are plotted along with a reference solution based on data provided by Huang et al.[23]. As shown in Figure 6.3, the 4th-order algorithm in Chord requires roughly half the cell count of the 2nd-order methods to produce an equivalent solution. Next, we explore applying and configuring AMR to the magnetic shock tube case. For the same parameters as the fixed-mesh simulations shown in Figure 6.3, a simulation is performed using the 2nd-order algorithm with 3 levels of adaptive mesh refinement. The grid spacing on the coarsest level corresponds to a grid size of only 1024 cells ($\Delta x \approx 1 \times 10^{-3}$). Refinement tagging is based on the relative gradient of the electron fluid density, with a threshold value of 0.005. These settings result in an accurate solution while maintaining a total cell count of only 2336 cells, a 3.5 times reduction in cell count compared to the fixed-mesh requirement for the 2nd-order solution shown in Figure 6.3. For studies shown in Figure 6.3 and Figure 6.4, the speed of light is set to $c = 2$ in order to match the settings from the reference solution over the time frame considered. These initial simulations are only run to an intermediate time, before the interior solution information reaches the boundaries, because the 4th-order accurate interior scheme in Chord is not compatible with the 1st-order, zero-gradient boundary conditions used. A higher-order, zero-gradient boundary condition is being developed for Chord. In the meantime, the remainder of the magnetic shock tube results presented here utilize the 2nd-order, PPM-limiter algorithm in Chord and a 1st-order, zero-gradient boundary conditions.

As previously mentioned, we vary the ion mass m_i to study the effects of scaling the ion inertial length ($d_{s\,i} = c/\omega_{p\,i}$) relative to the solution domain length. In Figure 6.5, the ion inertial length is

slightly larger than the domain length. The ion fluid is nearly decoupled from the magnetic field, and is much slower to respond than the electron fluid. The solution structure looks similar to that of a neutral gas shock; however, there are some oscillations in the electron density (particularly for $x \in [0.0, 0.35]$) due to coupling with the electromagnetic fields.

Figure 6.6 represents a case where the ion inertial length is about 4 times smaller than the domain length. In this case, there is extensive, high-wavenumber content in the solution and the resulting gradients from the oscillations have triggered adaptive mesh refinement over most of the domain, as illustrated by the vertical mesh lines in the background of the plot. This level of refinement is probably unnecessary except in regions of strong discontinuities, and this particular case may benefit from a different tagging method. Regardless, the Chord solution agrees well with the reference solution.

When the ion inertial length is $\sim 10^3$ times smaller than the domain size, both electron and ion fluids are strongly coupled to the electromagnetic fields. As shown in Figure 6.7, the solution structure starts to resemble that of the classic, MHD based solution[18,20,62], with one notable difference from MHD: the multi-fluid solution is capable of capturing the dispersive waves originating in the source terms which result from the high plasma frequency in this regime. In this case, the AMR settings have produced an efficient refinement of the mesh; the solution is highly detailed near shocks and dispersive oscillations, but the grid spacing is sufficiently coarsened in regions which are more quiescent. The minimum time step requirements outlined in Section 3.5 are adhered to for the magnetic shock tube cases discussed herein. However, the minimum grid size is also critical to the accuracy of these simulations, as demonstrated in Figure 6.8. As the grid is coarsened, the maximum wavenumber captured by the solution is reduced, and the solution becomes generally smoother and less oscillatory.

Finally, we offer some preliminary performance characterization of various algorithms and AMR settings in Chord for the magnetic shock tube problem. The results and simulation parameters are shown in Table 6.1. By enabling a lower overall cell count, the solutions using AMR demonstrate significant improvements in computational time compared to fixed-grid solutions. The

higher-order solution allows a coarser mesh to be used, and AMR provides a reduction in total cell count compared to a fixed, high-resolution grid; as a result, the 4th-order algorithm with 2 levels of AMR achieved equivalent solution accuracy in only $\sim 30\%$ of the time required by the 2nd-order algorithm with a fixed, high-resolution grid.

Table 6.1: Comparing the computational efficiency of various solution methods in Chord. All rows represent minimum grids required for an accurate solution to the magnetic shock tube problem with $m_i = 1$. The simulations are run to a partial solution time of $t = 0.4$ to avoid interaction with the boundaries, for reasons discussed earlier. All cases are run with the same CFL number, 0.82. The AMR solutions use refinement criteria based on electron density relative gradients with a threshold of 0.01. The values reported in the Compute Time column represent normalized wall clock times for each solution. The absolute values of computational CPU-hours aren't currently germane because the algorithm has not yet been compiled in an optimized, production environment.

Solver	**AMR Levels**	**Coarse Cells**	**Total Cells**	**Coarse Δx**	**Coarse Δt**	**Compute Time**
2nd-order PPM	0	8192	8192	1.22×10^{-4}	1.0×10^{-4}	1.00
4th-order PPM	0	4096	4096	2.44×10^{-4}	2.0×10^{-4}	0.40
2nd-order PPM	2	2048	2656	4.88×10^{-4}	4.0×10^{-4}	0.27
4th-order PPM	2	1024	1512	9.77×10^{-4}	8.0×10^{-4}	0.29

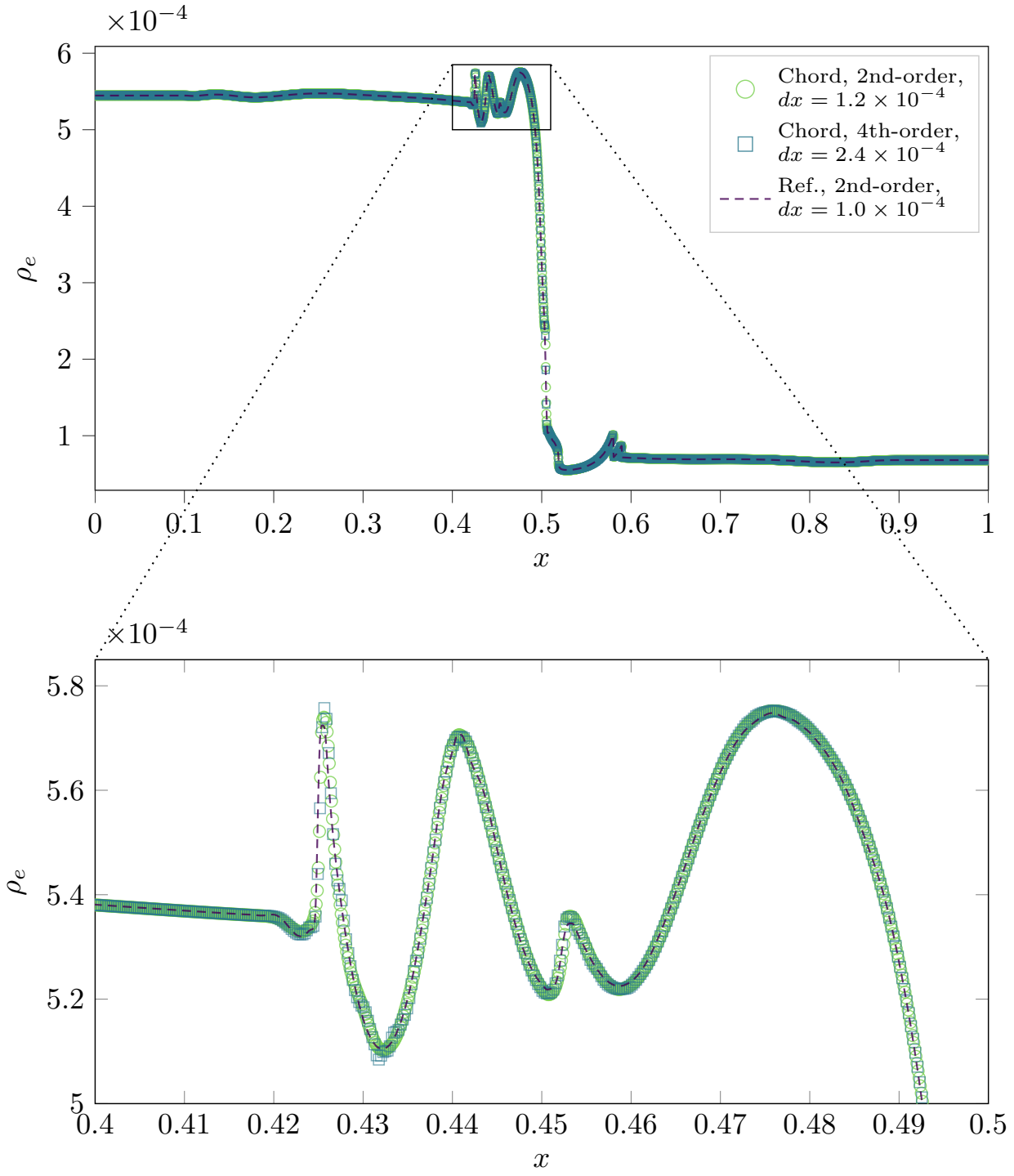

Figure 6.3: Magnetic shock tube results at a normalized time of 0.2 for $m_i = 1$. The solutions from Chord (lighter markers) are compared to the reference solution (darker, dashed line)[23]. For these simulations, the speed of light was set to $c = 2$ in order to match the settings of the reference solution. Results are shown for both the 2nd-order and 4th-order accurate algorithms in Chord. The reference solution is 2nd-order. All solutions use a fixed grid, with grid spacing as specified in the legend.

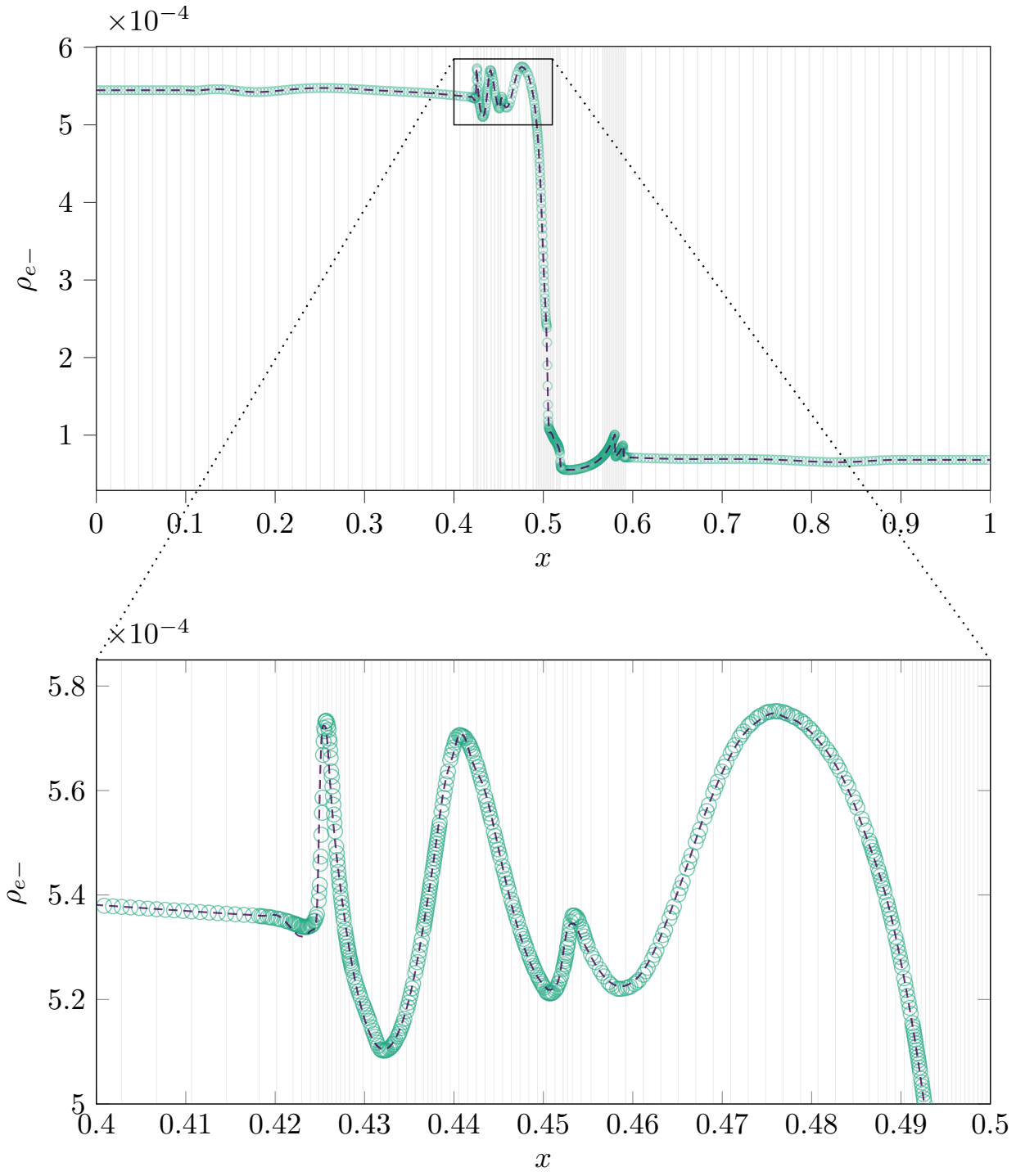

Figure 6.4: Magnetic shock tube results at a normalized time of 0.2 for $m_i = 1$ and $c = 2$. The solution from Chord (lighter, circular markers) is compared to the reference solution (darker, dashed line)[23]. The reference solution uses a fixed mesh spacing of 1.0×10^{-4}. The Chord solution uses AMR with 3 levels of refinement and a coarse mesh spacing of 1×10^{-3}. Mesh refinement was determined based on the relative gradient values of the electron density, ρ_e, with a gradient threshold of 0.005. The adaptive mesh spacing in Chord is displayed on the plot as thin, vertical lines (the mesh line density has been reduced by a factor of $1/8$ to improve clarity).

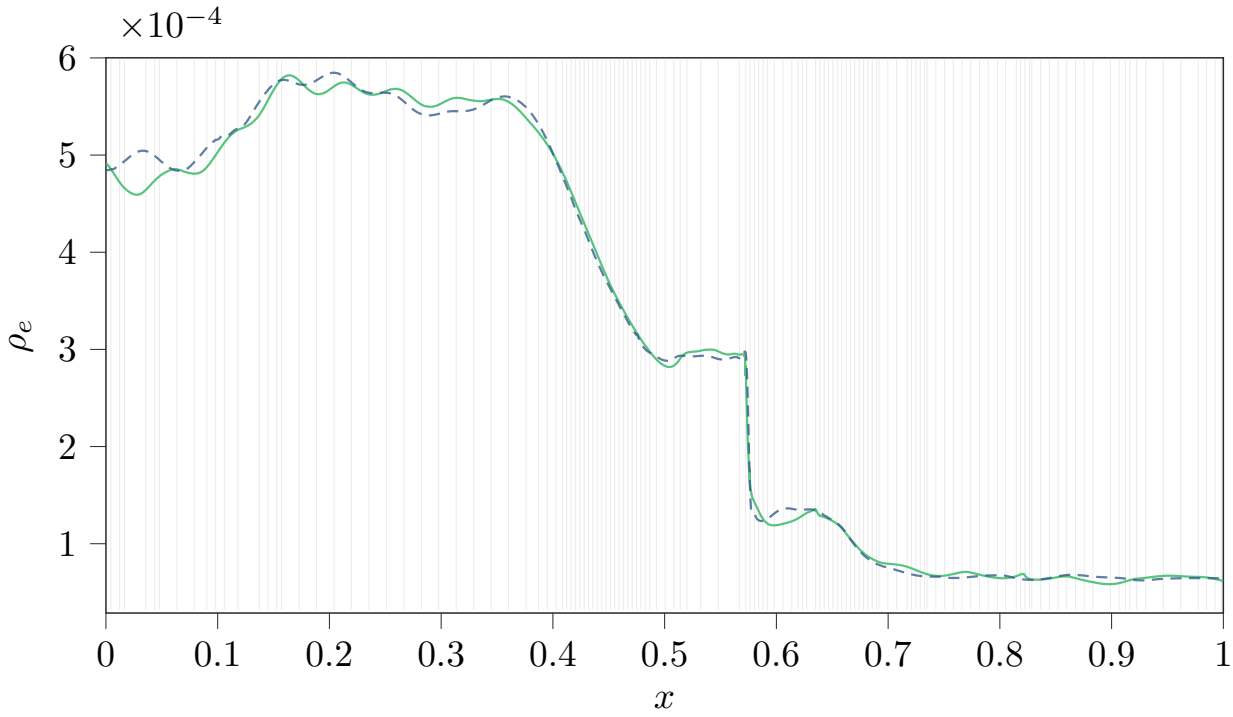

Figure 6.5: Magnetic shock tube results at a normalized time of 10 for $m_i = 1$. The solution from Chord (lighter, solid line) is compared to the reference solution (darker, dashed line)[23]. The reference solution uses a fixed mesh spacing of 1.0×10^{-4}. The Chord solution uses AMR with 3 levels of refinement and a coarse mesh spacing of 3.9×10^{-3}. Mesh refinement was determined based on the relative gradient values of the electron density, ρ_e, with a gradient threshold of 0.005. The adaptive mesh spacing in Chord is displayed on the plot as thin, vertical lines (the mesh line density has been reduced by a factor of $1/8$ to improve clarity).

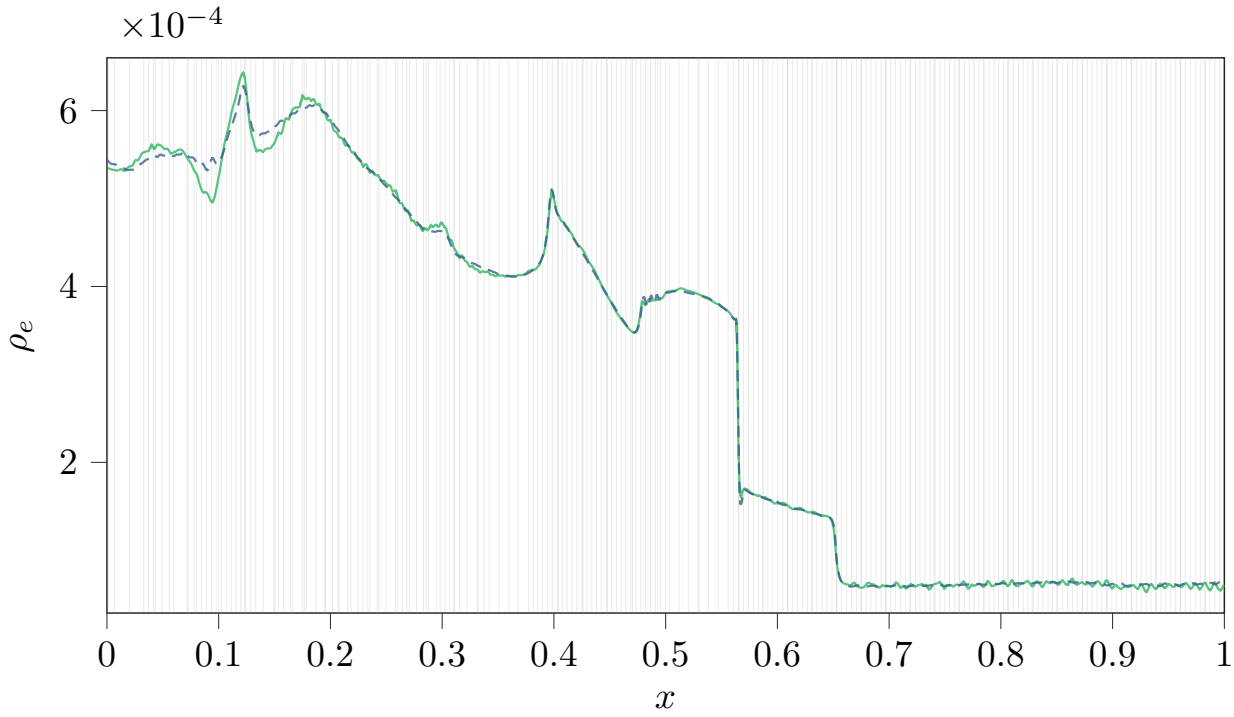

Figure 6.6: Magnetic shock tube results at a normalized time of 10 for $m_i = 1 \times 10^{-1}$. The solution from Chord (lighter, solid line) is compared to the reference solution (darker, dashed line)[23]. The reference solution uses a fixed mesh spacing of 1.0×10^{-4}. The Chord solution uses AMR with 3 levels of refinement and a coarse mesh spacing of 1.9×10^{-3}. Mesh refinement was determined based on the relative gradient values of the electron density, ρ_e, with a gradient threshold of 0.002. The adaptive mesh spacing in Chord is displayed on the plot as thin, vertical lines (the mesh line density has been reduced by a factor of $1/16$ to improve clarity).

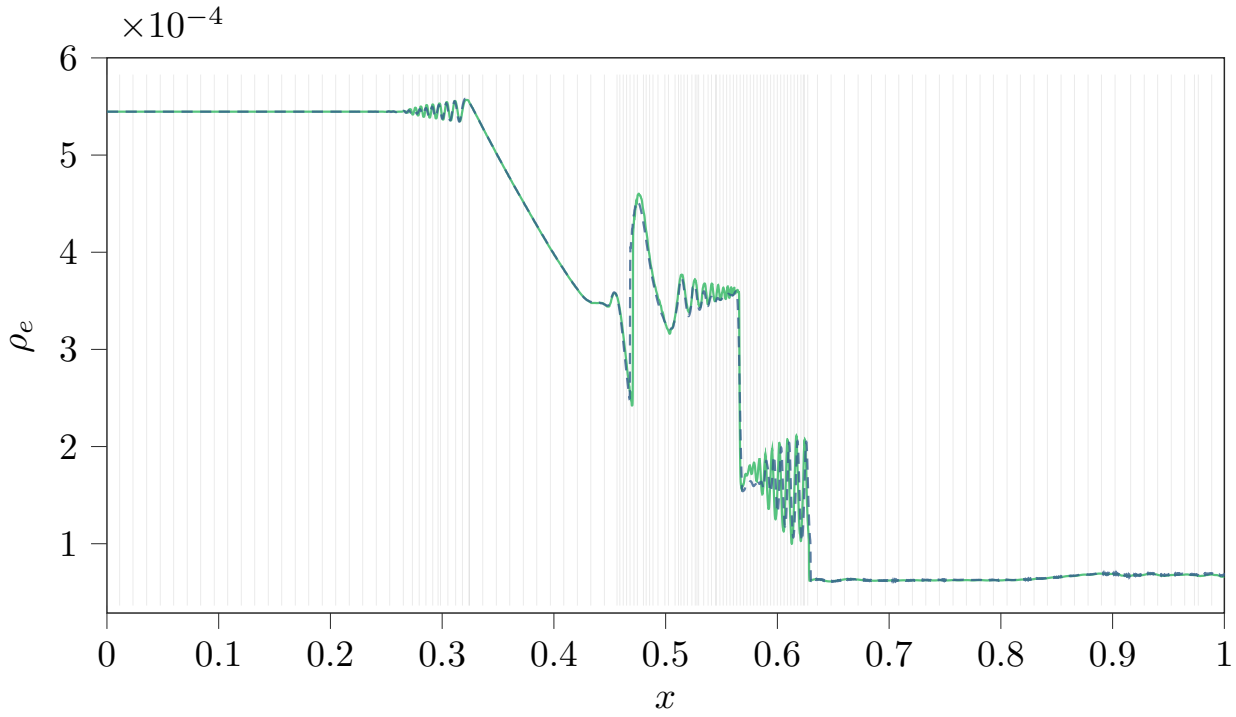

Figure 6.7: Magnetic shock tube results at a normalized time of 10 for $m_i = 1 \times 10^{-3}$. The solution from Chord (lighter, solid line) is compared to the reference solution (darker, dashed line)[23]. The reference solution uses a fixed mesh spacing of 1.0×10^{-4}. The Chord solution uses AMR with 2 levels of refinement and a coarse mesh spacing of 2.4×10^{-4}. Mesh refinement was determined based on the relative gradient values of the electron density, ρ_e, with a gradient threshold of 0.002. The adaptive mesh spacing in Chord is displayed on the plot as thin, vertical lines (the mesh line density has been reduced by a factor of $1/48$ to improve clarity).

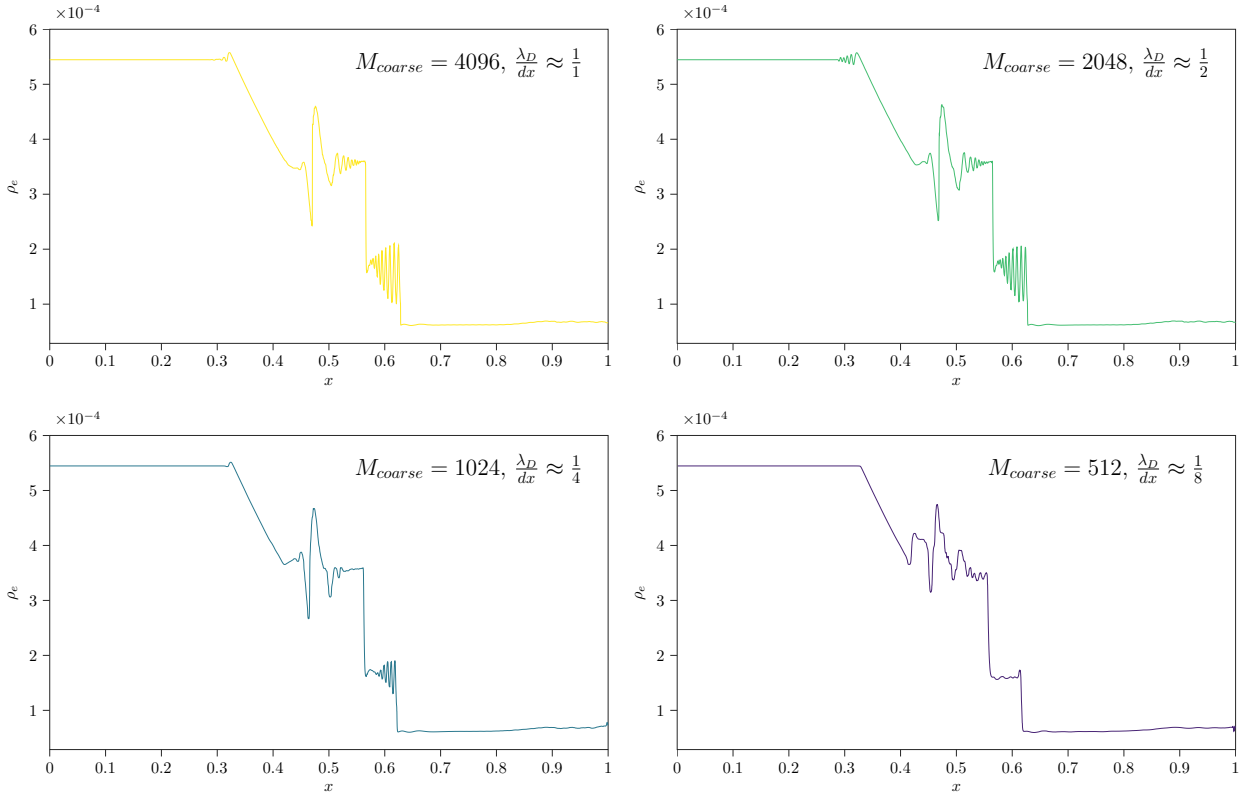

Figure 6.8: Magnetic shock tube results at a normalized time of 10 for $m_i = 1 \times 10^{-3}$. The solution from Chord is compared for four different mesh resolutions. Two levels of AMR refinement are used in all cases. Mesh refinement was determined based on the relative gradient values of the electron density, ρ_e, with a gradient threshold of 0.002. In all four cases, the plasma (electron) frequency drives the maximum time step, so the same time step value of $\Delta t = 2.5 \times 10^{-5}$ is used in each case.

6.3 GEM Challenge Magnetic Reconnection Problem

Magnetic reconnection is a physical phenomenon occurring in some plasmas in which the topology of the magnetic field is modified, and the resulting change in magnetic energy is absorbed by the plasma via changes to the kinetic and thermal energy. We setup this simulation according to the Geospace Environmental Modeling (GEM) Reconnection Challenge project, which was established to study the discrepancy in magnetic reconnection times between plasma models (particularly single-fluid MHD models) and empirical observations[3].

6.3.1 Nondimensionalization

In accordance with the original definition of the GEM challenge problem[3], we nondimensionalize spatially using the ion inertial length or skin depth $d_{s\,i} = \sqrt{m_i / \left(n_i q_i^2 \mu_0\right)}$ using number density $n_i = n_0$. Temporal nondimensionalization is performed using the ion cyclotron frequency $\omega_{c\,i} = q_i \|\vec{B}\| / m_i$, with $|\vec{B}| = B_0$. As a result, velocities are normalized by the Alfvén speed $v_A = B_0 / \sqrt{\mu_0 n_0 m_i}$ (we neglect the contribution of electrons to the mass density for simplicity).

6.3.2 Domain & Boundary Conditions

The original GEM challenge problem is specified in a 2D domain on the x-z plane. In the present work, we have translated the problem onto the x-y plane to be consistent with the coordinates and nomenclature used in Chord. The GEM challenge problem is modeled in Chord as a 2D domain spanning $[0, L_x] \times [0, L_y]$. The $x-$boundaries are periodic, and the $y-$boundaries are set as conducting (PEC) walls, as defined in Section 3.4.2.

6.3.3 Initial Conditions

The problem is initialized with a Harris current sheet with the following equilibrium magnetic field profile:

$$\vec{B}^0 = B_0 \tanh\left(\frac{y - \frac{L_y}{2}}{\kappa}\right) \cdot \mathbf{e}^x, \tag{6.10}$$

where $\mathbf{e}^x$ is a unit vector in the x direction. A perturbation is applied to the magnetic field to disturb the equilibrium condition,

$$\zeta\left(x,y\right)=\zeta_0\cos\left(\frac{2\pi\left(x-\frac{L_x}{2}\right)}{L_x}\right)\cos\left(\frac{\pi\left(y-\frac{L_y}{2}\right)}{L_y}\right) \tag{6.11}$$

$$\vec{B}^1=-\mathbf{e}^z\times\nabla\zeta\left(x,y\right), \tag{6.12}$$

resulting in the following initialization of the magnetic field:

$$\vec{B}=\vec{B}^0+\vec{B}^1. \tag{6.13}$$

Both divergence-correction potentials, Φ and Ψ, are initialized to zero throughout the domain. The original GEM problem seems to have been designed for MHD models; when applying the GEM problem to the multi-fluid plasma model herein, decisions have to be made regarding initialization of the electric current and electric field. A common treatment is to initialize the electric field to zero

$$\vec{E}=\left[0,0,0\right]^T. \tag{6.14}$$

It is also common to assume the initial electrical current is carried only by electrons and is based solely on the equilibrium component of the magnetic field, $\vec{B}^0$ [19,20,63], thus the initial electric current density would be

$$\vec{j}=\frac{1}{\mu_0}\vec{\nabla}\times\vec{B}^0=-\frac{B_0}{\mu_0\kappa}\operatorname{sech}^2\left(\frac{y-\frac{L_y}{2}}{\kappa}\right)\cdot\mathbf{e}^z. \tag{6.15}$$

These assumptions simplify the problem setup, but they are inconsistent. As a result, the intended equilibrium condition is contravened and the incongruence may quickly destabilize the solution. A more robust initialization would consider both the ion and electron contributions to electric current,

and the initial, equilibrium electric field would be in balance with the fluid pressure and momentum terms. Nevertheless, after numerical experiments, we have elected to use the simpler, popular initialization of the current and electric field, Equation (6.14) and Equation (6.15), because it allows more direct comparison to other multi-fluid simulations of the GEM challenge from literature, and it is an interesting test of Chord's capability of handling the initialization inconsistency. The initial number density for both ion and electron fluids is

$$n_i = n_e = n_0 \operatorname{sech}^2\left(\frac{y - \frac{L_y}{2}}{\kappa}\right) + n_\infty, \tag{6.16}$$

thus the initial mass densities are

$$\rho_i = m_i n_i \tag{6.17}$$

$$\rho_e = m_e n_e. \tag{6.18}$$

Initial ion fluid momentum is prescribed as zero and the initial electron fluid momentum is determined from the electrical current density, $\vec{j}$. Consequently, the fluid momentum and velocity terms are initialized as follows:

$$\rho_i \vec{u}_i = [0, 0, 0]^T \tag{6.19}$$

$$\rho_e \vec{u}_e = \frac{m_e}{q_e} \vec{j} \tag{6.20}$$

$$\vec{u}_i = \frac{\rho_i \vec{u}_i}{\rho_i} \tag{6.21}$$

$$\vec{u}_e = \frac{\rho_e \vec{u}_e}{\rho_e}. \tag{6.22}$$

Initial fluid temperatures are constant throughout the domain, and the fluid pressure is initialized as

$$p_i = n_i \frac{B_0^2}{2\mu_0 k_B n_0 \left(1 + \frac{T_e}{T_i}\right)} \tag{6.23}$$

$$p_e = p_i \frac{T_e}{T_i}. \tag{6.24}$$

These equations are structured to include the ratio T_e/T_i because this is a model input parameter. Finally, the fluid energy density is initialized, based on the fluid pressure, density, and velocity, as

$$\rho_i e_i = \frac{\rho_i}{2} \vec{u}_i \cdot \vec{u}_i + \frac{p_i}{\gamma_i - 1} \tag{6.25}$$

$$\rho_e e_e = \frac{\rho_e}{2} \vec{u}_e \cdot \vec{u}_e + \frac{p_e}{\gamma_e - 1}. \tag{6.26}$$

6.3.4 Model Parameters

Most of the parameters for the simulation come from the original GEM problem definition[3]. The domain size is $L_x = 8\pi$ and $L_y = 4\pi$. In normalized units, $B_0 = 1$, $\zeta_0 = 0.1$, and $n_0 = 1$. The ratio of ion mass to electron mass is $m_i/m_e = 25$, the ion mass is $m_i = 1$, the temperature ratio is $T_e/T_i = 0.2$, and the background number density is $n_\infty = 0.2 n_0$. The current sheet width parameter is set to $\kappa = 0.5$. The specific heat ratios for each fluid are equal, $\gamma_i = \gamma_e = 5/3$. Normalized fluid electric charge values are: $q_i = -q_e = 1$. The normalized Boltzmann constant is specified as $k_B = 1$. The original paper describing the GEM challenge did not specify the speed of light, c. We prescribe the normalized light speed as $c = 10 v_A$, where $v_A = B_0/\sqrt{\mu_0 n_0 m_i}$. Finally, we set $\mu_0 = 1$ and $\epsilon_0 = 1/\left(c^2 \mu\right)$.

To demonstrate the solution-stabilizing efficacy of the methods described in Section 3.7, in particular the HO-ACR and FCOR methods, we solve the GEM challenge problem with and without these two methods enabled. The two simulations are otherwise identical. Both use a coarse mesh size of 144×72. Two levels of AMR are specified, with a refinement ratio of 2 between each level.

AMR tagging is based on relative gradients of the electron energy density, with a tagging threshold of 0.18. A fixed time step of 5×10^{-3} is specified at the coarse mesh level.

6.3.5 Results and Discussion

Two simulations are performed: one without using the stabilization techniques, and the other using the HO-ACR and FCOR methods. Both solutions are initialized with the same AMR mesh topology, as expected. Due to the nature of the problem, the solution starts off slowly and both simulations are consistent. However, by a solution time of $t = 5$, in the simulation without the HO-ACR and FCOR methods, we start to observe some nonphysical oscillations developing along the horizontal boundary between the finest and next finest levels of AMR, as shown in Figure 6.9. In contrast, the simulation using HO-ACR and FCOR does not produce any unexpected oscillations at the AMR boundaries, as sown in Figure 6.10.

As the solution without numerical stabilization continues to evolve, the oscillations which originated at the boundaries between AMR levels propagate away from the AMR boundaries and begin to contaminate the solution elsewhere in the domain, as shown in Figure 6.11. By a solution time of $t = 15$, the simulation without HO-ACR and FCOR has become unstable and is near the point of diverging, as shown in Figure 6.13. On the other hand, the simulation with numerical-stabilizing methods HO-ACR and FCOR enabled continues to produce a stable and accurate solution, shown in Figures 6.12 and 6.14.

For completeness, the solution to the simulation with HO-ACR and FCOR is shown at three later time steps in Figure 6.15. Despite the dissipation provided by the solution-stabilizing methods, the simulation produces highly detailed and accurate results which compare well to the reference literature[20,23,64]. It is interesting to note the development of a plasmoid-like feature along the midplane at $y = 2\pi$, shown in Figure 6.15 panels (e) and (f). The dissipation in Chord is not too strong as to suppress naturally occurring instabilities like this, and the plasmoid-like feature convects outwards and eventually coalesces with the larger "island", as reported in literature[65,66].

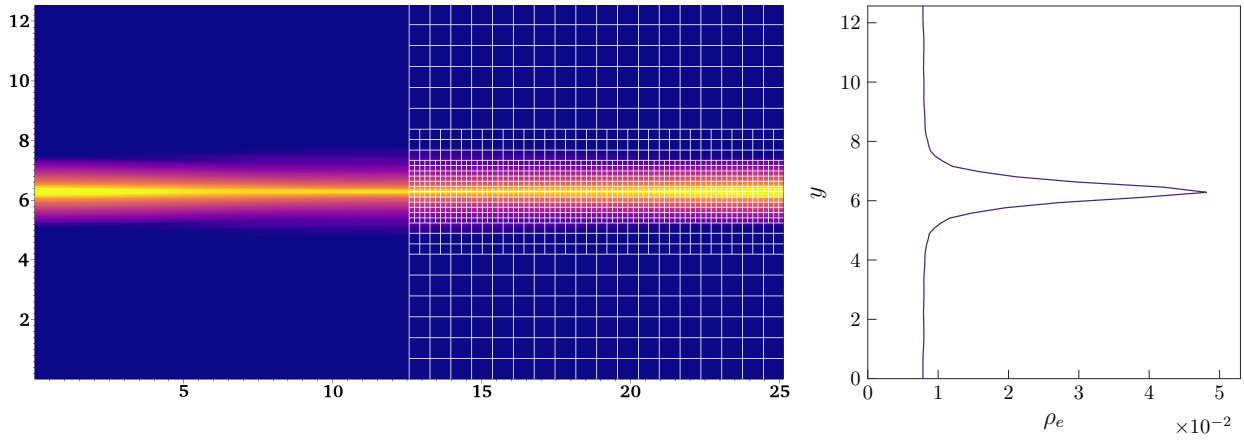

Figure 6.9: Electron density, ρ_e, at $t = 5$, for the case without the HO-ACR algorithm and without FCOR. We see subtle oscillations beginning to develop near the center of the domain, originating at the horizontal boundary between the finest and next finest mesh patches; this is in contrast to the plot in Figure 6.10. The mesh shown here on half of the contour plot has been drawn with a $4\times$ reduced resolution, to improve clarity. On the right is a plot of ρ_e taken from a vertical line through the center of the domain, $x = 4\pi$.

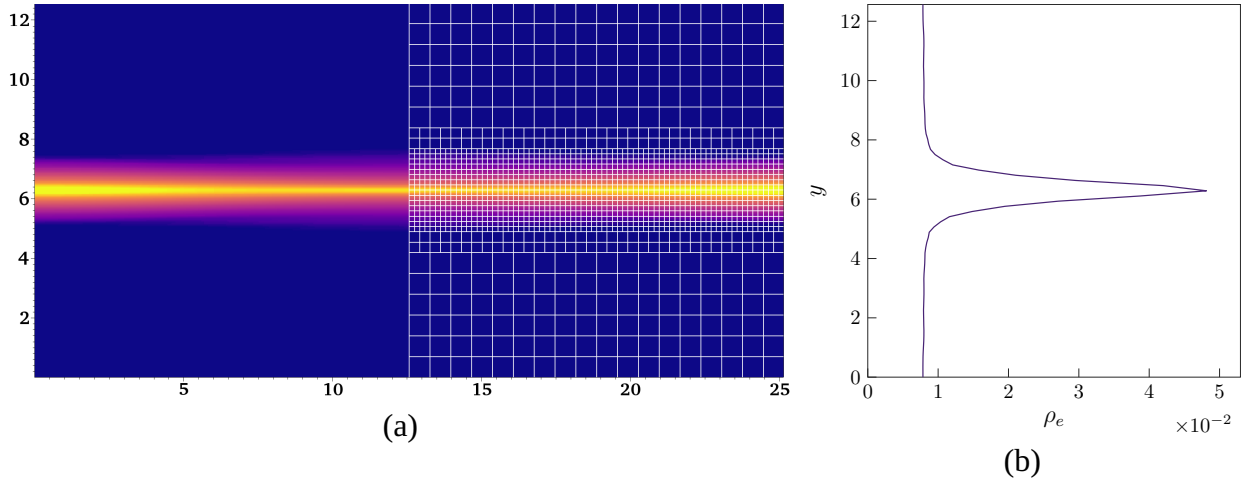

(a) (b)

Figure 6.10: Electron density, ρ_e, at $t = 5$, for the case with the HO-ACR algorithm and with FCOR. No unexpected oscillations are present and the solution evolution is stable. The mesh shown here on half of the contour plot has been drawn with a $4\times$ reduced resolution, to improve clarity. On the right is a plot of ρ_e taken from a vertical line through the center of the domain, $x = 4\pi$.

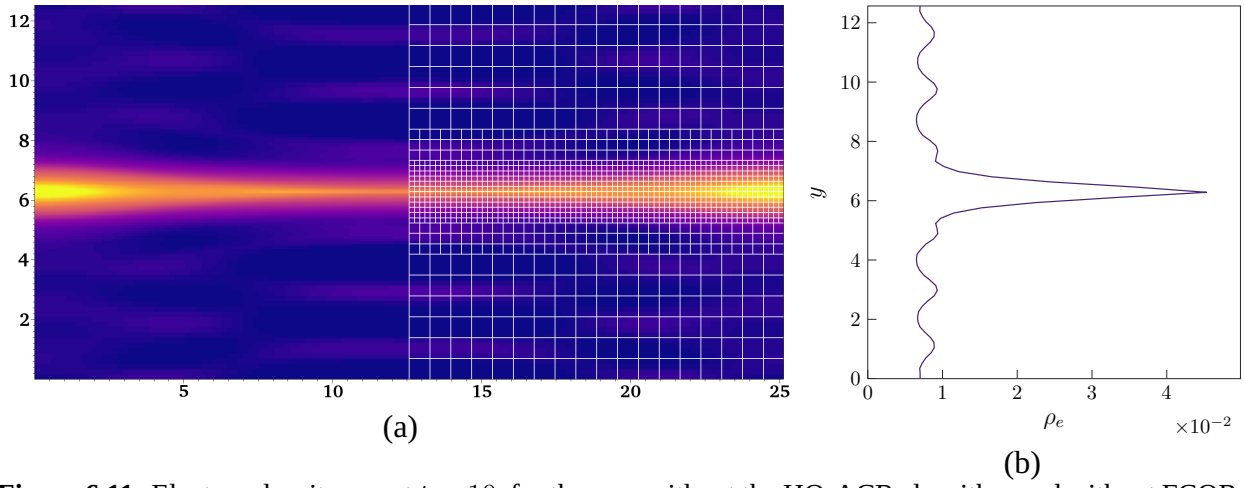

Figure 6.11: Electron density, ρ_e, at $t = 10$, for the case without the HO-ACR algorithm and without FCOR. The oscillations which were first noticed in Figure 6.9 have started to propagate, corrupting the solution away from the AMR boundaries; this is in contrast to the plot in Figure 6.12. The mesh shown here on half of the contour plot has been drawn with a $4\times$ reduced resolution, to improve clarity. On the right is a plot of ρ_e taken from a vertical line through the center of the domain, $x = 4\pi$.

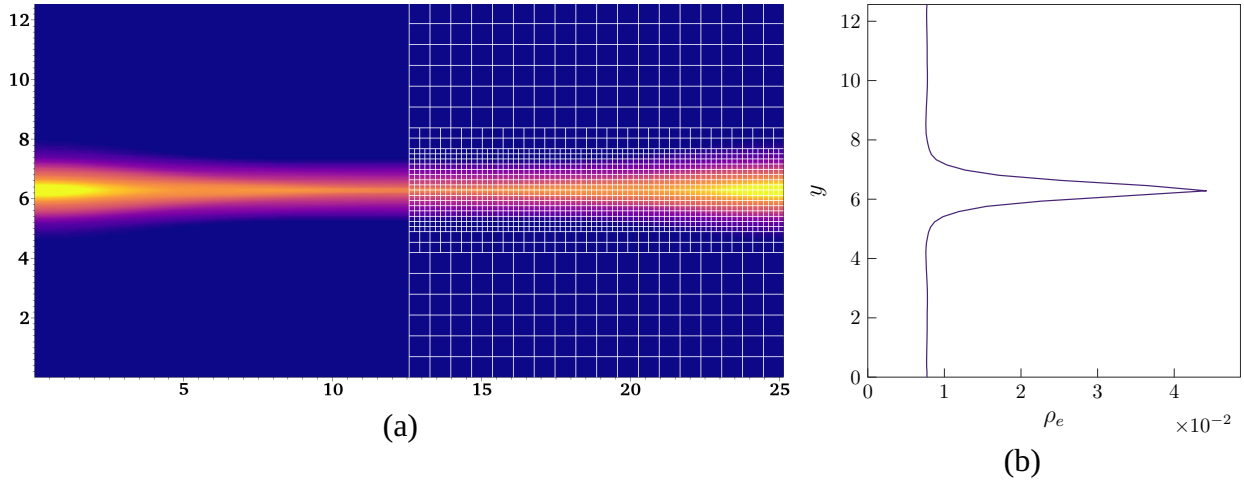

Figure 6.12: Electron density, ρ_e, at $t = 10$, for the case with the HO-ACR algorithm and with FCOR. The solution continues to evolve without unexpected oscillations. The mesh shown here on half of the contour plot has been drawn with a $4\times$ reduced resolution, to improve clarity. On the right is a plot of ρ_e taken from a vertical line through the center of the domain, $x = 4\pi$.

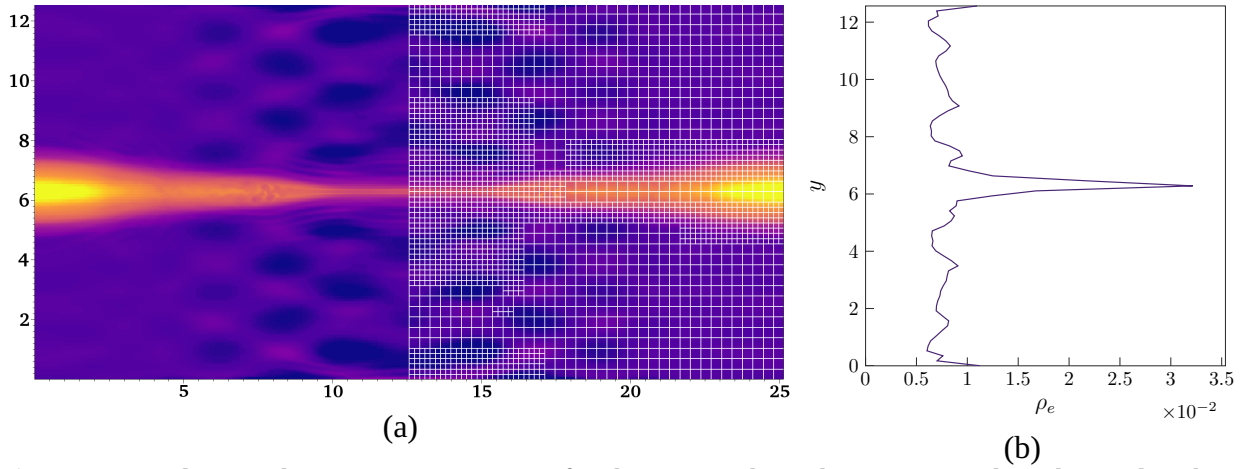

(a) (b)

Figure 6.13: Electron density, ρ_e, at $t = 15$, for the case without the HO-ACR algorithm and without FCOR. The oscillations in electron density have destabilized the solution, affecting other solution variables. The solution does not progress much further in time than this, eventually diverging. Clearly the numerical-stabilizing methods are required for this problem, as demonstrated in Figure 6.14. The mesh shown here on half of the contour plot has been drawn with a $4\times$ reduced resolution, to improve clarity. On the right is a plot of ρ_e taken from a vertical line through the center of the domain, $x = 4\pi$.

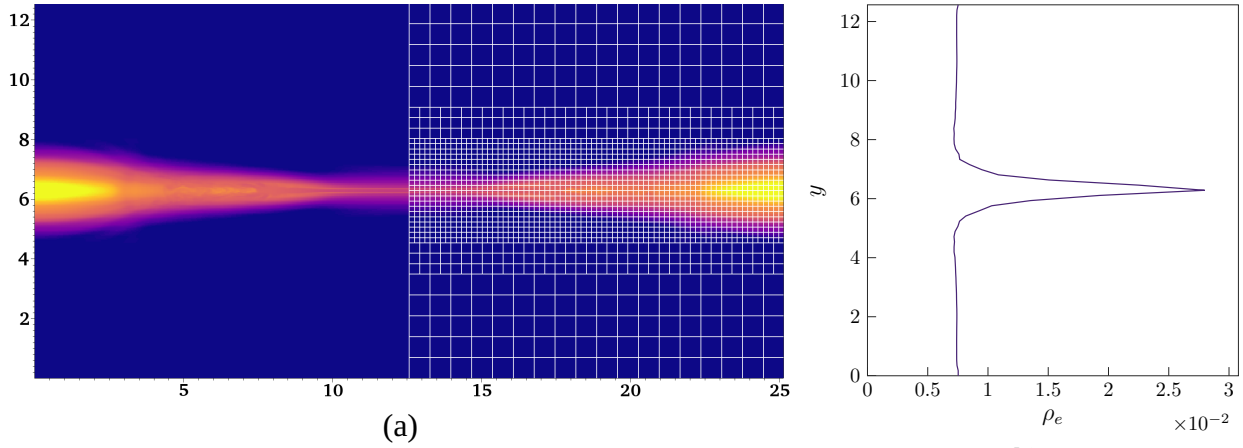

(a) (b)

Figure 6.14: Electron density, ρ_e, at $t = 15$, for the case with the HO-ACR algorithm and with FCOR. The solution continues to evolve without unexpected oscillations. The mesh shown here on half of the contour plot has been drawn with a $4\times$ reduced resolution, to improve clarity. On the right is a plot of ρ_e taken from a vertical line through the center of the domain, $x = 4\pi$.

With the solution-stabilizing methods well-characterized for this problem, the next step is to compare an AMR solution with a solution on a fixed grid. Furthermore, the magnetic flux reconnection for the Chord solutions is compared in Figure 6.16 against the full particle based solution and a classical, single-fluid MHD solution from the GEM Challenge description[3]. The Chord solutions not only compare closely to the full particle solution, but there is also good consistency between the solution obtained with AMR and the solution using a fixed, uniform grid. In Figure 6.17, the fixed-grid and AMR solutions from Chord are plotted side-by-side, for comparison. The abrupt rise in computed magnetic flux in the Chord solution around times 28-30 are due to the formation of the aforementioned plasmoid-like features, which appear in both the AMR and fixed-grid solutions.

In Figure 6.17, the ion density is plotted side-by-side for both simulations, at various, normalized solution times. For each plot, the grid is superimposed over the right half of the domain. The AMR solution is using the relative gradient of electron energy density as a tagging criteria. For the first half of the solution ($t \lesssim 20$), when the electron energy density is still concentrated along the initial current sheet, only about one third of the grid is refined; as a result these earlier time steps require less computational effort and the AMR solution iterates much faster than the fixed-grid solution. However, once the fluid jets start to emerge out of the X-point and shock waves begin to propagate in the y direction, significant gradients in the electron energy density appear throughout the domain, triggering mesh refinement. By the time $t \gtrsim 32$, the majority (sometimes all) of the domain is fully-refined and the computational effort is the same as the fixed-grid case, which is expected for such solution phenomena. Regardless, because of the improvements in computational efficiency earlier in the solution, AMR is able to provide a 15% improvement in solution time compared to the fixed-grid case.

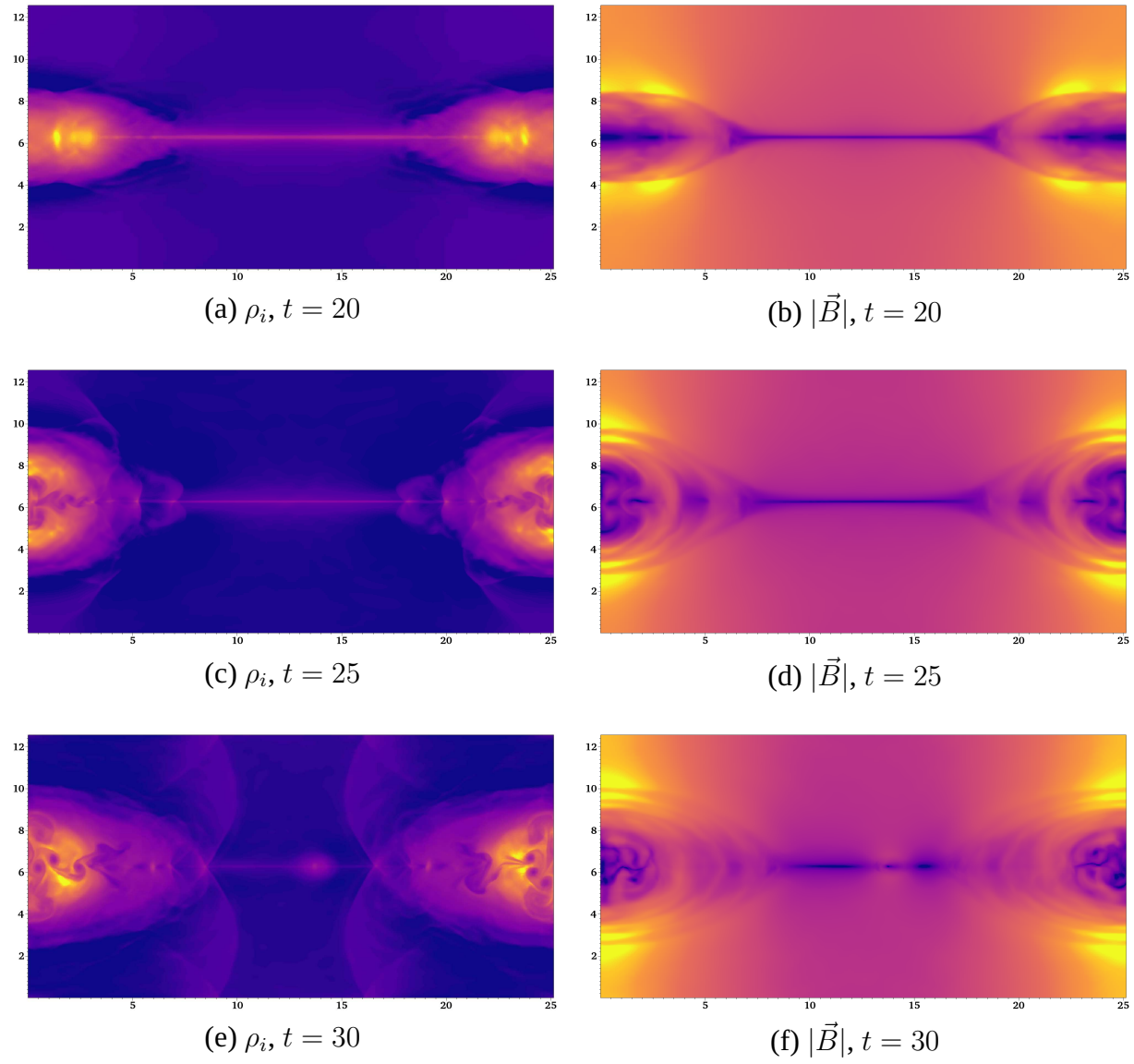

(a) ρ_i, $t = 20$ (b) $|\vec{B}|$, $t = 20$

(c) ρ_i, $t = 25$ (d) $|\vec{B}|$, $t = 25$

(e) ρ_i, $t = 30$ (f) $|\vec{B}|$, $t = 30$

Figure 6.15: The solution evolution in time is shown for the case with the HO-ACR and FCOR algorithms enabled. This simulation uses two levels of AMR and a coarse grid of 144×72, with tagging based on the electron energy density, $\rho_e e_e$. The left column shows the ion density, ρ_i, and the magnetic field magnitude $|\vec{B}|$ is shown on the right.

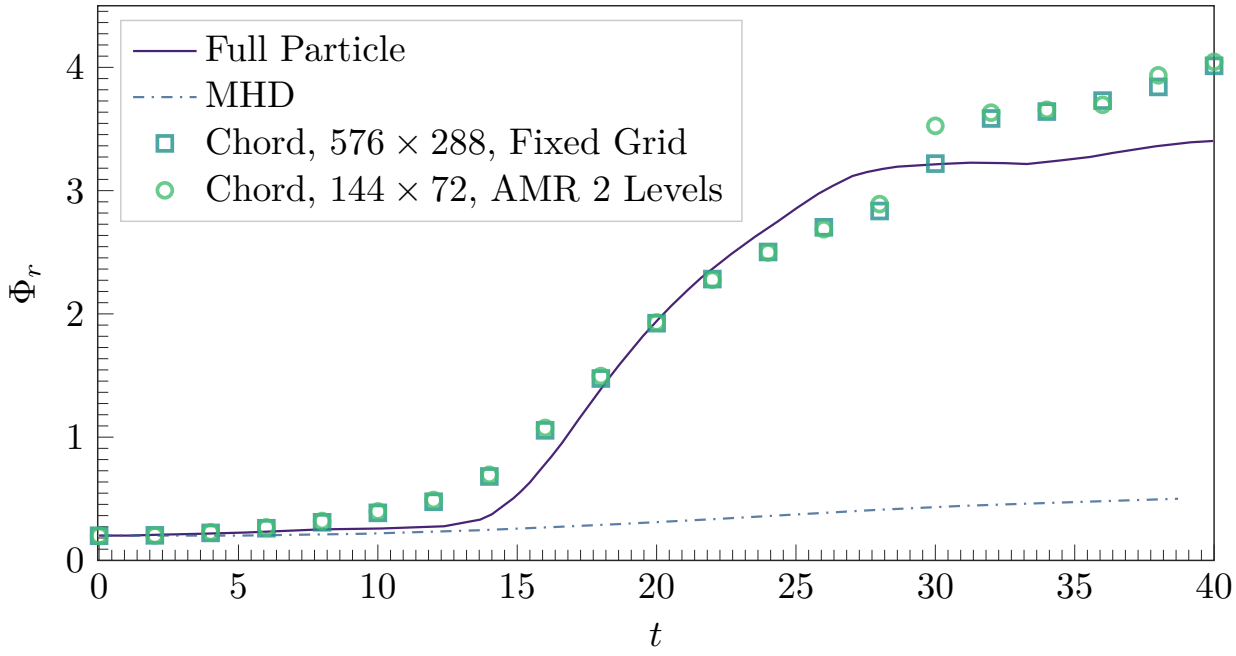

Figure 6.16: Reconnected magnetic flux vs. time for the GEM Challenge case. For reference, the full particle and classical, single-fluid MHD solutions from the original GEM challenge publication[3] are presented. The Chord solutions agree well with the full particle solution. As anticipated, there is little difference in reconnected magnetic flux between the fixed-grid and AMR solutions in Chord.

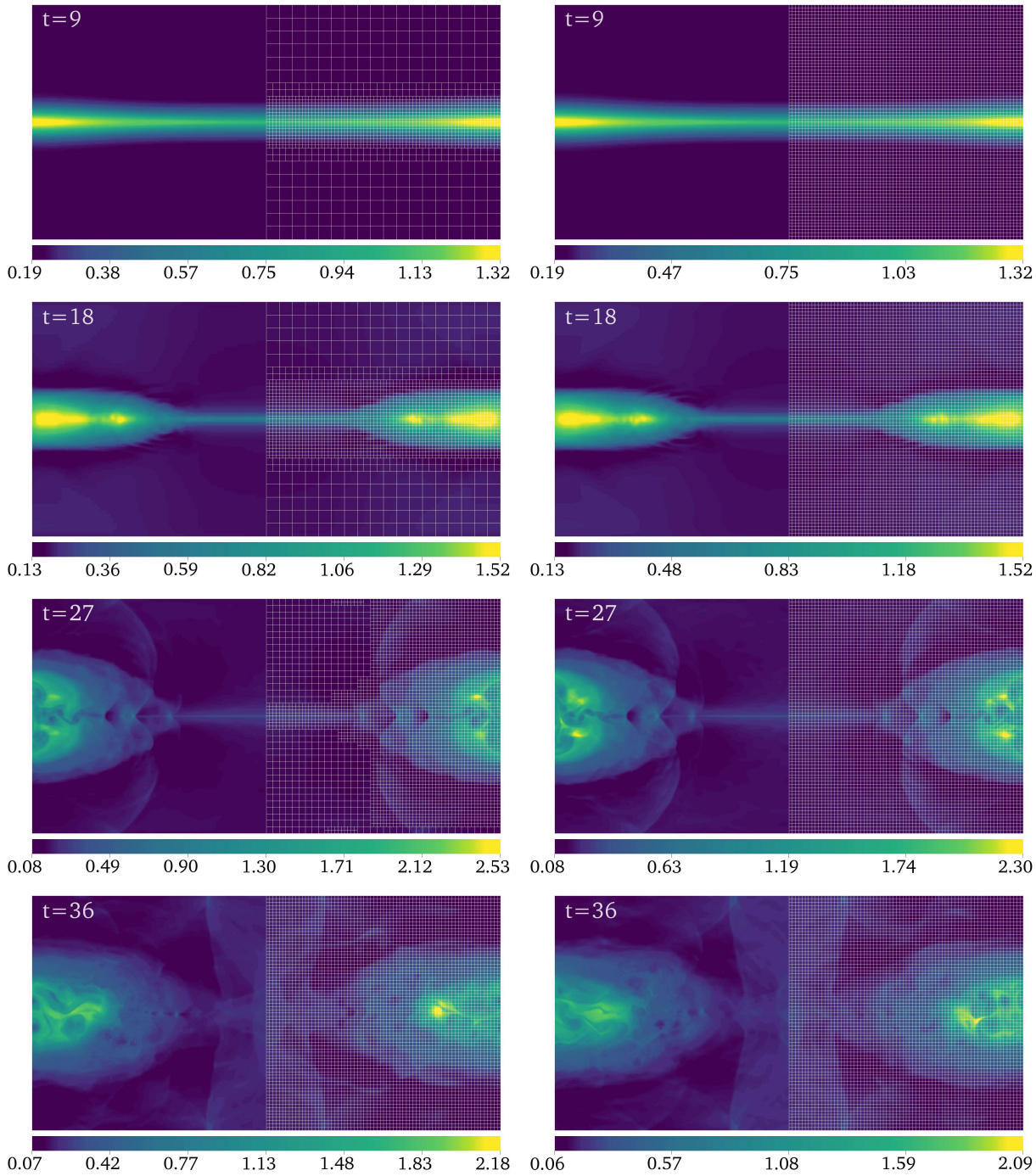

Figure 6.17: Chord solutions to the GEM reconnection problem, comparing the solution obtained with AMR (left column) to that with a fixed, uniform mesh (right column). The plots show nondimensionalized ion mass density ρ_i at various solution times. The AMR solution uses a coarse grid size of 144×72 cells with two levels of adaptive refinement and a refinement ratio of 2. The fixed mesh solution uses a grid size of 576×288. Both solutions use identical CFL numbers. The mesh at each time step is superimposed on the right half of each plot, and the mesh resolution is reduced by a factor of 4 for visualization clarity. The AMR solution uses refinement tagging based on the relative gradient of the electron energy density $\rho_e e_e$.

6.4 Plasma Blast Explosion

Shock waves in a plasma can be distinctly different compared to purely hydrodynamic shocks due to the enormous disparity in mass between various species and because of the influence on charged species motion from electromagnetic fields. Not only are shock waves in plasmas an important and relevant phenomenon to study, but they also provide an excellent test of the stability and robustness of our numerical algorithm. Furthermore, because the strong gradients and trenchant structure that develop around shock waves are often localized within the solution domain, AMR can be a highly efficient tool to improve the computational efficiency.

Previously[64], we have used the multi-fluid plasma algorithm in Chord with AMR to solve a 1D magnetic shock tube problem. In the present work, we adapt a 2D plasma explosion problem from the literature[67]. The 2D plasma explosion or blast test case is interesting because, despite an initially symmetric discontinuity, the anisotropic, external magnetic field drives an asymmetric solution structure to evolve. Cylindrical (2D) and spherical (3D) plasma explosion problems are commonly used as test cases for MHD models, but there is a dearth of these types of problems being solved by multi-fluid plasma models. Therefore, we also investigate the effects of unequal particle mass between the electron and ion species, not resolvable with traditional, single-fluid, Ideal MHD models.

6.4.1 Computational Configurations

The plasma blast problem is constructed on a 2D domain in the x-y plane, spanning $\Big[0, L_x\Big] \times \Big[0, L_y\Big]$. The domain boundaries are set as zero-gradient or open boundaries, as defined in Section 3.4.1. The plasma is initially neutral and homogeneous in density,

$$n_i = n_e = n_0, \tag{6.27}$$

thus the initial mass densities are

$$\rho_i = m_i n_i \tag{6.28}$$

$$\rho_e = m_e n_e. \tag{6.29}$$

The fluid is initially motionless, with zero momentum

$$\rho_i \vec{u}_i = [0, 0, 0]^T \tag{6.30}$$

$$\rho_e \vec{u}_e = [0, 0, 0]^T . \tag{6.31}$$

$$\tag{6.32}$$

There is a circular discontinuity in pressure, centered in the domain, with a radius of $0.1 L_x$. Inside the circle, the fluid pressure is $p_i = p_e = p_{in}$, and everywhere else $p_i = p_e = p_{out}$. The fluid energy density is initialized, based on the fluid pressure, density, and velocity, as

$$\rho_i e_i = \frac{\rho_i}{2} \vec{u}_i \cdot \vec{u}_i + \frac{p_i}{\gamma_i - 1} \tag{6.33}$$

$$\rho_e e_e = \frac{\rho_e}{2} \vec{u}_e \cdot \vec{u}_e + \frac{p_e}{\gamma_e - 1}. \tag{6.34}$$

The initial electric field is zero, and an external magnetic field with magnitude B_0 is applied in the y direction

$$\vec{E} = [0, 0, 0]^T \tag{6.35}$$

$$\vec{B} = [0, B_0, 0]^T . \tag{6.36}$$

Both divergence-correction potentials, Φ and Ψ, are initialized to zero throughout the domain.

6.4.2 Model Parameters

The domain size is $L_x = L_y = 12$. In normalized units, $B_0 = 10$, $n_0 = 1$, and the ion mass is $m_i = 1$. Initially, we set the ratio of ion mass to electron mass to $m_i/m_e = 1$, in order to validate our results against the reference solution[67]. Subsequently, we set the ratio to $m_i/m_e = 25$ (as in the GEM problem) to explore the more complex and realistic physics that materialize in the solution. The specific heat ratios for each fluid are equal, $\gamma_i = \gamma_e = 5/3$. Normalized fluid electric charge values are: $q_i = -q_e = 1$. The initial pressure inside the circle is $p_{in} = 100$ and everywhere else $p_{out} = 1$. We set $\mu_0 = 1$ and $\epsilon_0 = 1/(c^2\mu)$. As in our previous work[64] and in the GEM problem, we follow the convention of setting the light speed to $c = 10v_A$, which, for this problem, results in $v_A = B_0/\sqrt{\mu_0 n_0 m_i} = 10$ and $c = 100$.

6.4.3 Results and Discussion

Our first goal with this test case is to validate the solution by Chord against the reference solution. In their paper, Zachary et al[67] were testing a single-fluid, Ideal MHD model. For a more direct comparison to the reference solution, we set the electron and ion particle masses equal to each other, $m_i/m_e = 1$. The authors of the reference solution appear to have used a fixed CFL number, and their solution results were reported after 48 time steps. However, it's not clear exactly what solution time this corresponds to. In Chord, the problem was solved using a fixed time step and a uniform grid of 160×160. We find that a nondimensionalized solution time of $t = 0.26$ provides results that very closely match the reference solution. As shown in the left column of Figure 6.18, the contour lines in the solution by Chord have approximately the same topology as those in the reference solution[67], and the shock structure in the Chord solution is similarly asymmetric, owing to the influence of the externally applied magnetic field.

One advantage of the multi-fluid approach to plasma modeling is the ability to solve for the electron and ion species separately, with different particle masses. To study this effect, we set the mass ratio to $m_i/m_e = 25$, and the results are shown in the right column of Figure 6.18. A mass ratio of 25 was used to be consistent with the GEM problem also discussed herein, and because it

helps alleviate some of the stiffness from using a realistic mass ratio of approximately 1836. We immediately see the effects of the disparate species masses. When the particle masses are the same (but opposite charge), the y component of the magnetic field forces opposite z component velocities in the electrons and ions, resulting in a z component of the electric field, but there is no mechanism for the development of an x or y component of the electric field. However, when the electrons are lighter and more mobile than the ions, their increased velocity relative to the ions results in a separation of charge, leading to the development of x and y components of the electric field, which effectively "pulls" the ions in tow. As a result, the shape of the solution is even more asymmetric compared to the case where $m_i/m_e = 1$.

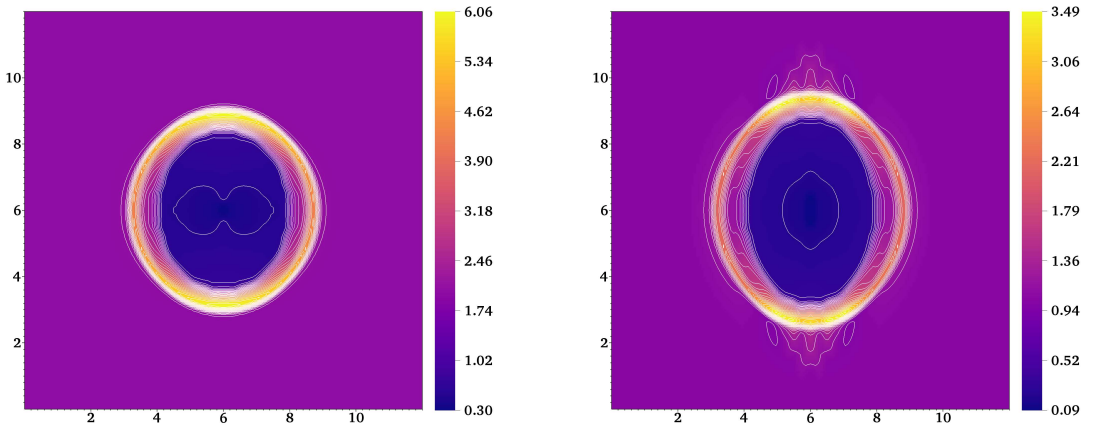

(a) Total fluid density, $m_i/m_e = 1$

(b) Total fluid density, $m_i/m_e = 25$

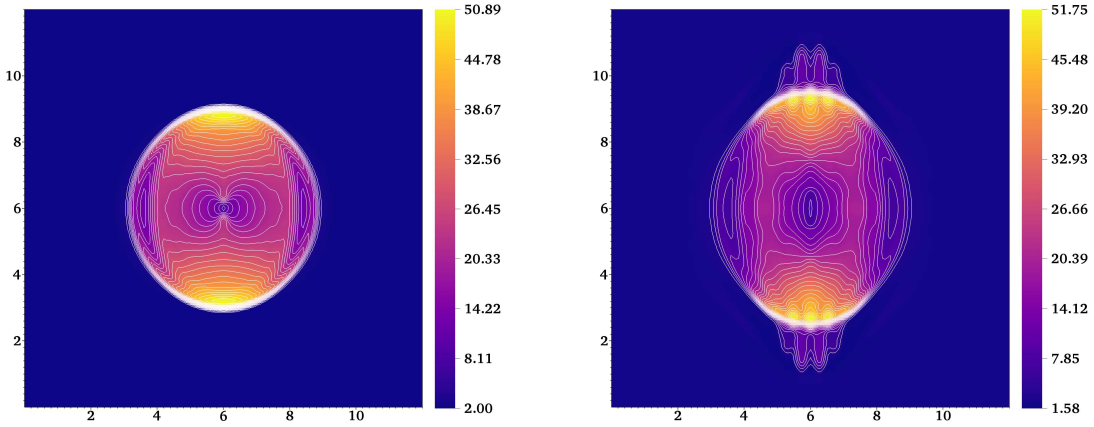

(c) Total fluid pressure, $m_i/m_e = 1$

(d) Total fluid pressure, $m_i/m_e = 25$

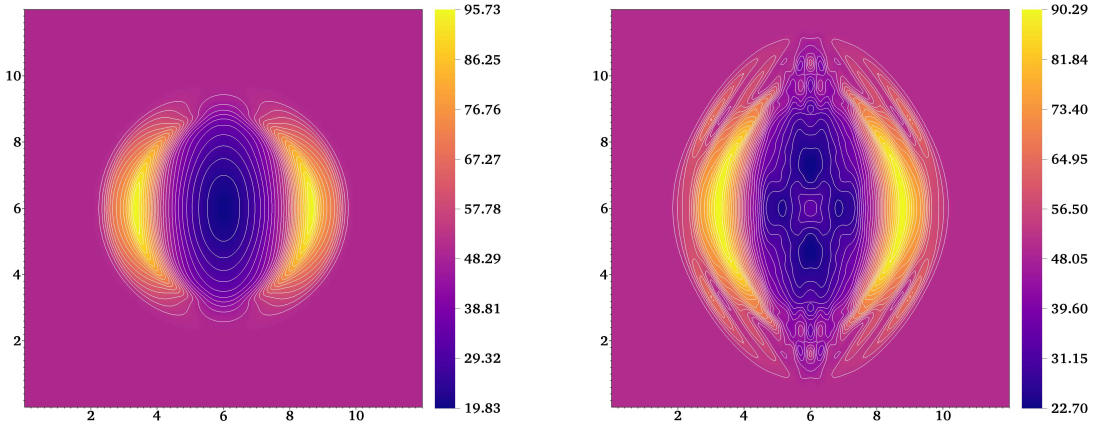

(e) Magnetic pressure, $m_i/m_e = 1$

(f) Magnetic pressure, $m_i/m_e = 25$

Figure 6.18: Plasma explosion results. The left column uses a mass ratio of $m_i/m_e = 1$ and is used to validate the Chord solution against the reference solution[67]. The right column uses a dissimilar mass ratio of $m_i/m_e = 25$ and highlights some of the enhanced detail and fidelity afforded by the multi-fluid plasma model, compared to a traditional, single-fluid MHD model. Both simulations use uniform grids of 160×160 cells and a time step of $\Delta t = 5 \times 10^{-4}$.

Next, we compare the fourth-order algorithm with a second-order algorithm (also PPM-based) in Chord. The advantage of higher-order reconstruction is that it often allows for similarly accurate solutions but on coarser meshes compared to lower-order algorithms, as demonstrated previously using a 1D magnetic shock tube problem[64]. We explore this potential by solving the plasma blast problem on uniform, successively finer meshes, using both the fourth-order and second-order algorithms. When analyzing the results, shown in Figure 6.19, we look for a difference in solution detail between the second and fourth-order algorithm results in columns 1 and 2 (density) as well as a difference in columns 3 and 4 (pressure). However, in this case, the fourth-order results and second-order results appear to converge in detail and accuracy at roughly the same pace relative to the mesh size. A more precise view of this behavior is shown in Figure 6.20, where density and pressure data are extracted from the domain over a diagonal line between $(0, 0)$ and (L_x, L_y); both second-order and fourth-order algorithms appear to reach a mesh-independent solution between mesh sizes 320×320 and 640×640. The explanation of this is actually straightforward: because the solution is highly discontinuous around the shock circumference, the fourth-order reconstruction is being reduced to second-order by the limiter. As a result, the fourth-order and second-order algorithms in Chord produce very similar results for highly-discontinuous problems such as this plasma blast case.

Finally, we explore the application of AMR to the plasma blast problem. In general, AMR is a highly effective technique for improving the computational efficiency of problems like the plasma blast case, where the domain is mostly quiescent and has only localized regions of steep gradients and detailed solution structure. Previously, we demonstrated an improvement in solve time by approximately $3\times$ when applying AMR to a 1D magnetic shock tube problem[64]. In this work, we propose a configuration of AMR settings that proves effective for the plasma blast case. We start with a coarse grid size of 40×40 and use three levels of adaptive mesh refinement. A ratio of 4 is used for the first level of refinement (starting from the coarsest), and a ratio of 2 is used for the next two levels of refinement. Tagging criteria is established based on the relative gradients of both the electron and ion energy density, $\rho_e e_e$ and $\rho_i e_i$, respectively, with a gradient

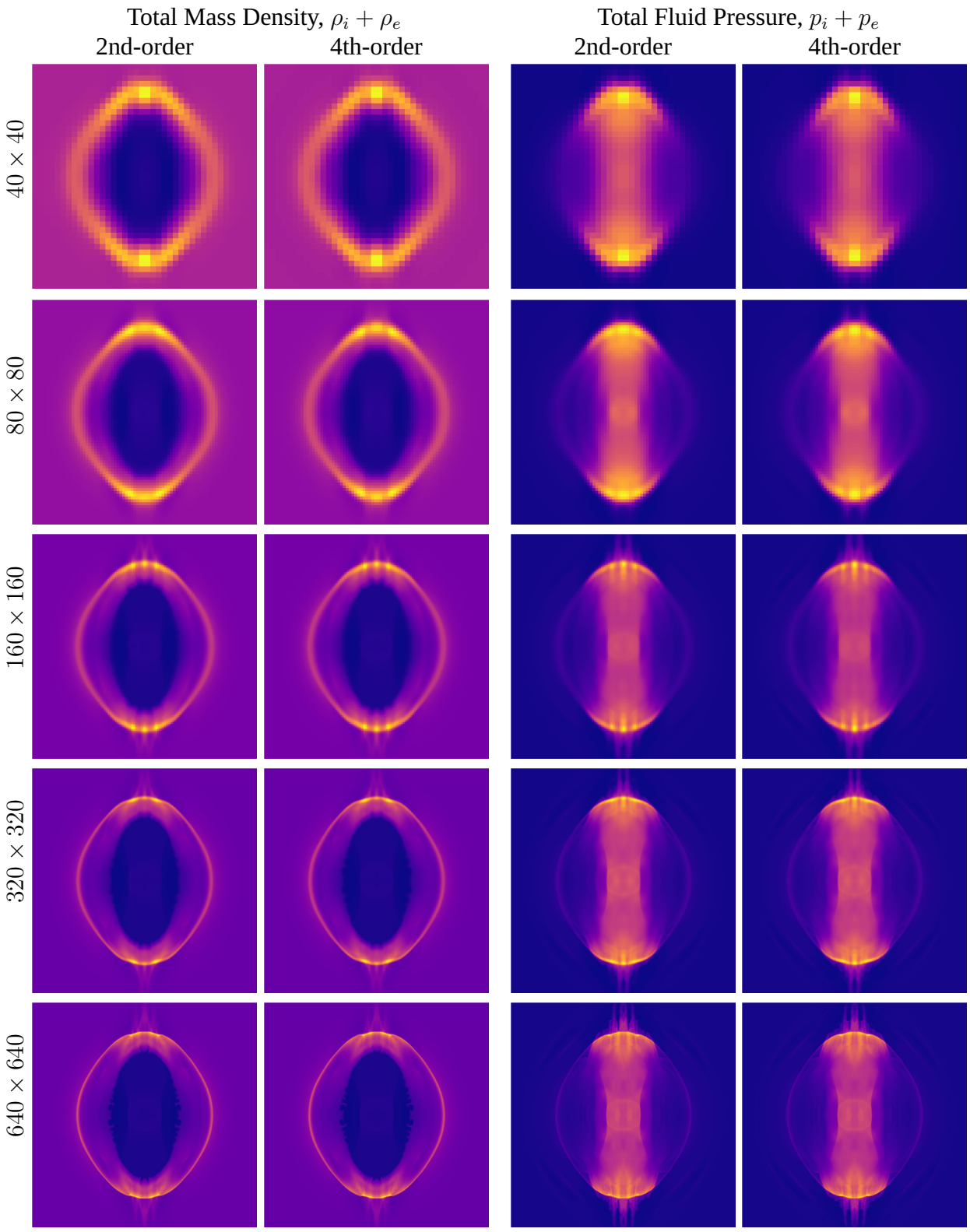

Figure 6.19: Comparing the mesh convergence trends between the second-order and fourth-order spatial reconstruction algorithms by Chord. The left two columns show total mass density, and the right two show total fluid pressure.

threshold of 0.5. Results of this simulation are shown in Figures 6.21 – 6.25. The relative difference in fluid density and pressure between the solution with AMR and the solution on a uniform mesh are plotted in Figure 6.24, illustrating how precisely these two solutions align. In Figure 6.25, sub-figures (e) and (f) show the divergence cleaning potentials Ψ and Φ effectively accumulating error in the solution and allowing the error to propagate out of the domain through the zero-gradient boundary conditions. Furthermore, the improvements in compute time afforded by the use of AMR were significant. As shown in Table 6.2, the plasma blast case with AMR solved approximately $10\times$ faster than an equivalent uniform-mesh case with the same time step (Δt) and grid size (Δx) at the finest level.

Table 6.2: Comparing the computational efficiency of various solution methods by Chord. The simulations are run to a partial solution time of $t = 0.4$. All cases are run with the same CFL number, 0.4. The AMR solutions use refinement criteria based on relative gradients of the electron and ion energy densities, with a threshold of 0.5. The values reported in the Compute Time column represent normalized wall clock times for each solution. The absolute values of computational CPU-hours are not currently apropos because the algorithm has not yet been compiled in an optimized, production environment.

Solver	**AMR Levels**	**Coarse Cells**	**Refinement Ratios**	**Coarse Δx**	**Coarse Δt**	**Compute Time, Normalized**
2nd-order PPM	0	640×640	–	1.875×10^{-2}	6.25×10^{-5}	0.68
4th-order PPM	0	640×640	–	1.875×10^{-2}	6.25×10^{-5}	1.00
2nd-order PPM	3	40×40	$4 - 2 - 2$	0.300×10^{0}	1.00×10^{-3}	0.09
4th-order PPM	3	40×40	$4 - 2 - 2$	0.300×10^{0}	1.00×10^{-3}	0.12

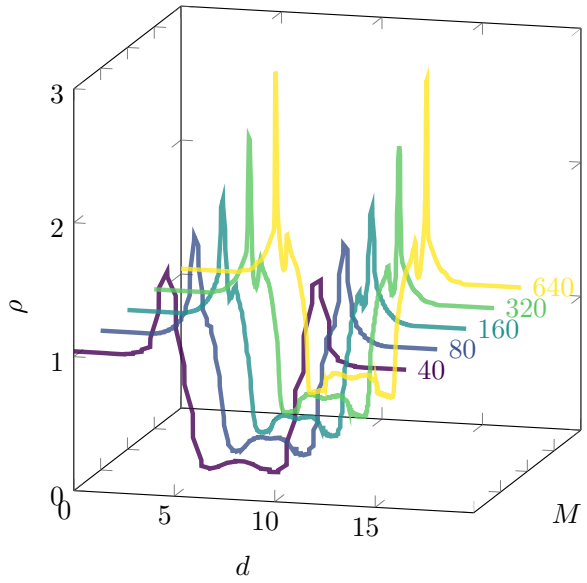

(a) Total mass density, 2nd-order

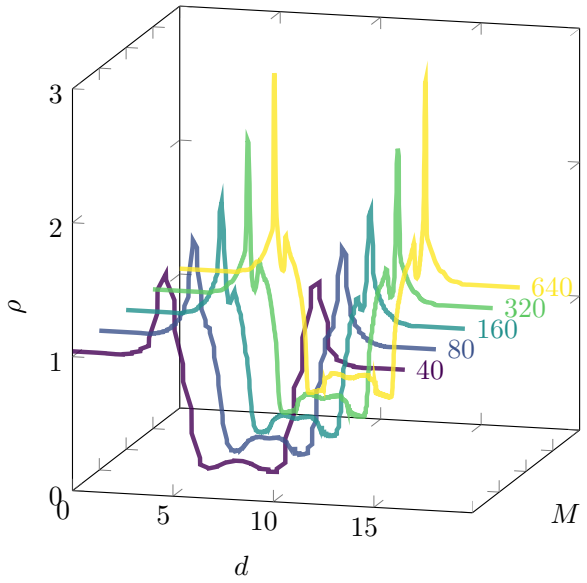

(b) Total mass density, 4th-order

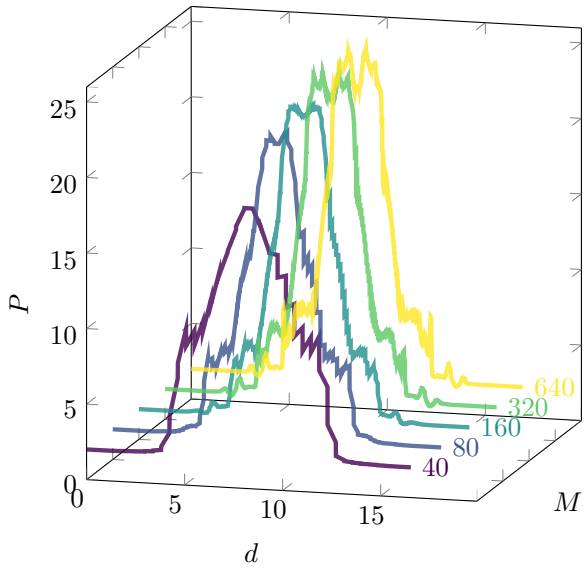

(c) Total fluid pressure, 2nd-order

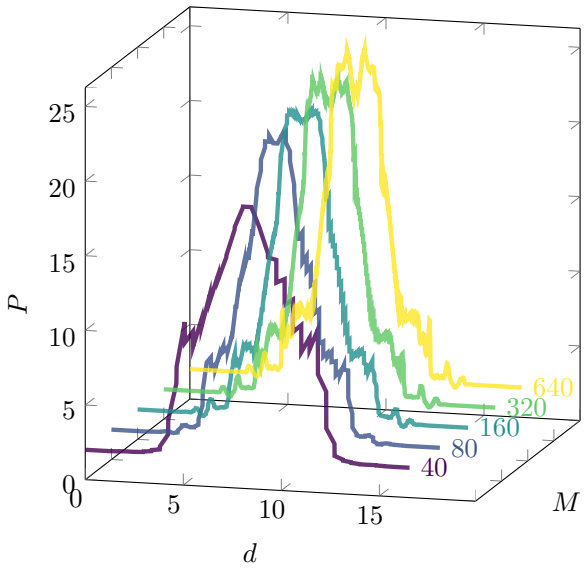

(d) Total fluid pressure, 4th-order

Figure 6.20: Comparing the mesh convergence trends between the second-order and fourth-order spatial reconstruction algorithms by Chord. The data shown in these plots is extracted from a diagonal section through the solution domain between points $(0, 0)$ and (L_x, L_y). The top two plots show total mass density ($\rho_i + \rho_e$), and the bottom two show total fluid pressure ($p_i + p_e$).

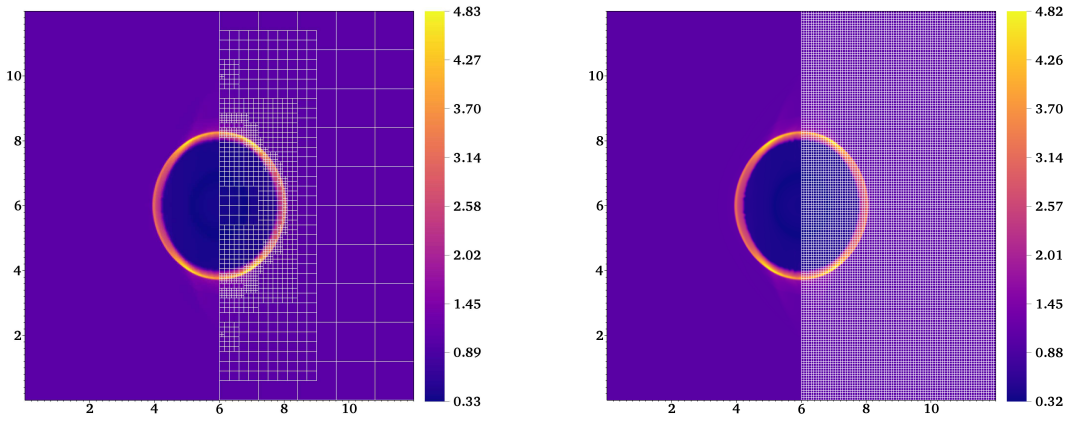

(a) AMR, $t = 0.12$

(b) Uniform Grid, $t = 0.12$

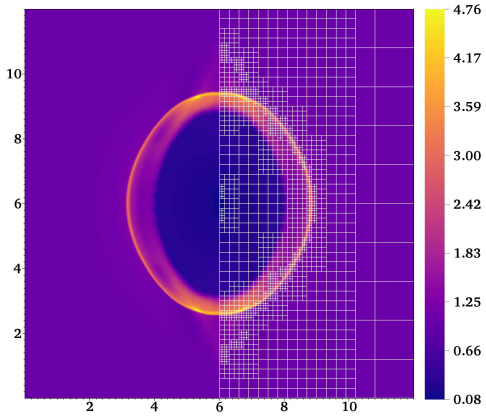

(c) AMR, $t = 0.26$

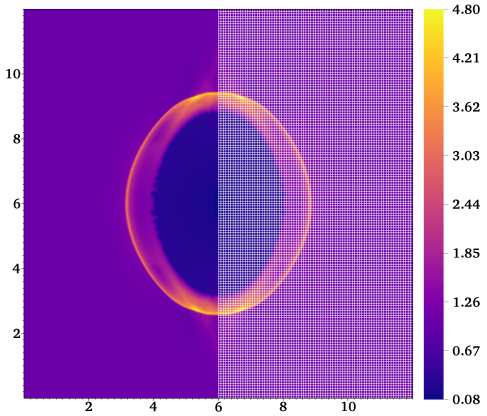

(d) Uniform Grid, $t = 0.26$

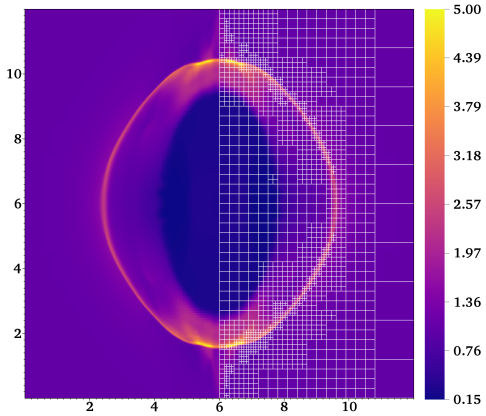

(e) AMR, $t = 0.40$

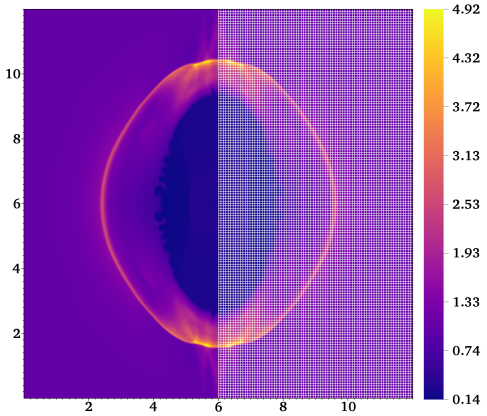

(f) Uniform Grid, $t = 0.40$

Figure 6.21: Total fluid density, $\rho_i + \rho_e$. Comparing the results of the solution with AMR (left column) with the solution on a uniform-grid mesh of 640×640 (right column) at various times shown. Both solutions use a fixed time step and the same CFL number based on the electromagnetic wave propagation speed. The AMR solutions use refinement criteria based on relative gradients of the electron and ion energy densities, with a threshold of 0.5. The mesh is shown on the right side of the domain in each plot, but the mesh resolution is reduced by a factor of $4\times$ to improve clarity.

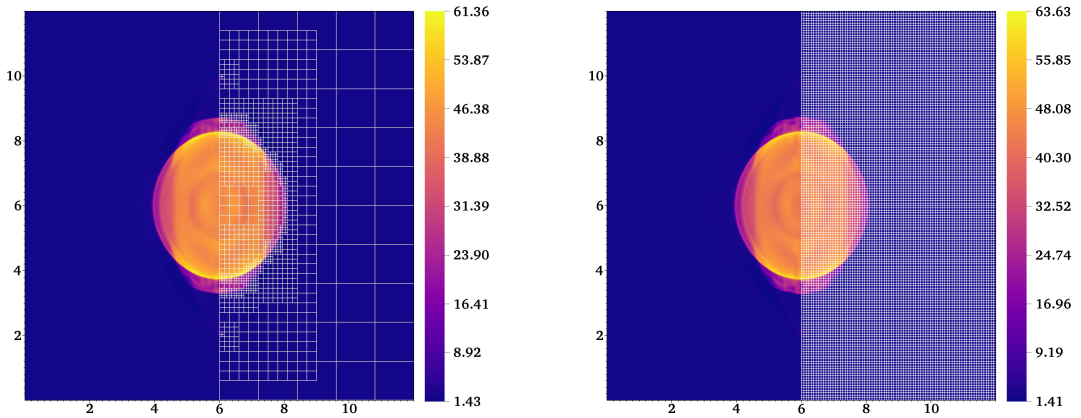

(a) AMR, $t = 0.12$ **(b)** Uniform Grid, $t = 0.12$

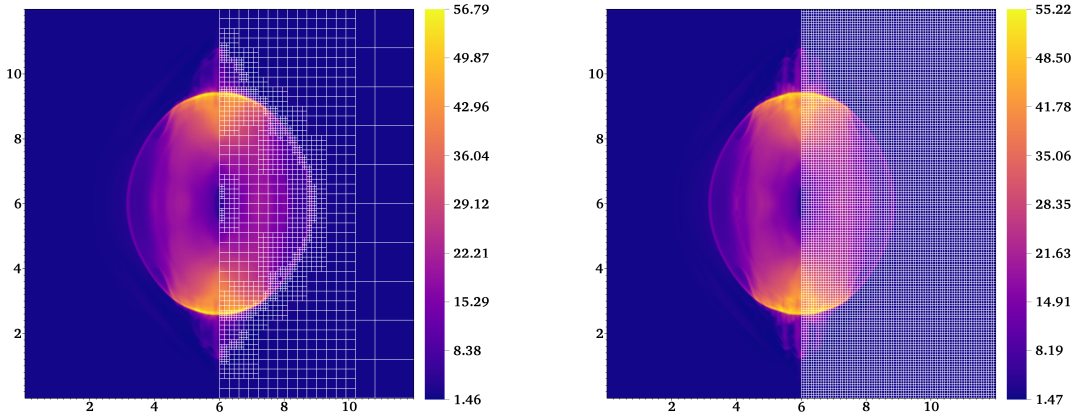

(c) AMR, $t = 0.26$ **(d)** Uniform Grid, $t = 0.26$

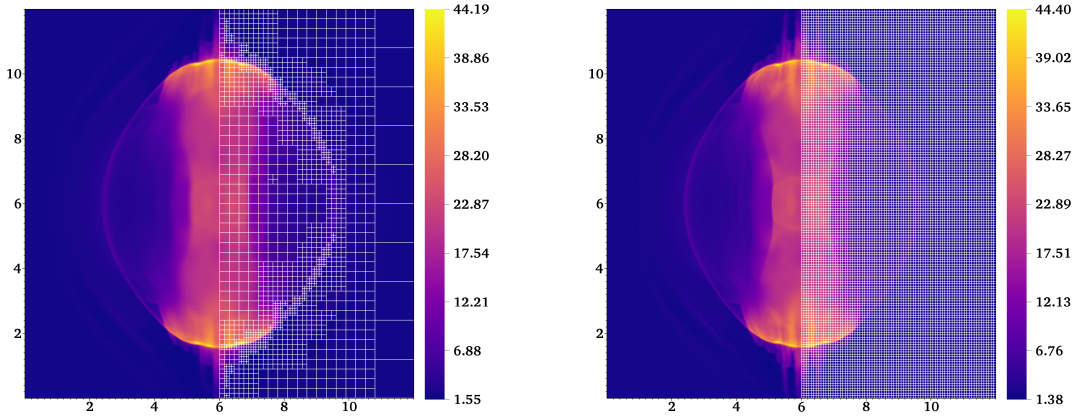

(e) AMR, $t = 0.40$ **(f)** Uniform Grid, $t = 0.40$

Figure 6.22: Total fluid pressure, $p_i + p_e$. Comparing the results of the solution with AMR (left column) with the solution on a uniform-grid mesh of 640×640 (right column) at various times shown. Both solutions use a fixed time step and the same CFL number based on the electromagnetic wave propagation speed. The AMR solutions use refinement criteria based on relative gradients of the electron and ion energy densities, with a threshold of 0.5. The mesh is shown on the right side of the domain in each plot, but the mesh resolution is reduced by a factor of $4\times$ to improve clarity.

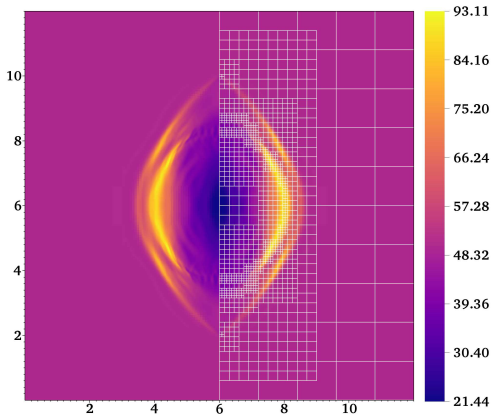

(a) AMR, $t = 0.12$

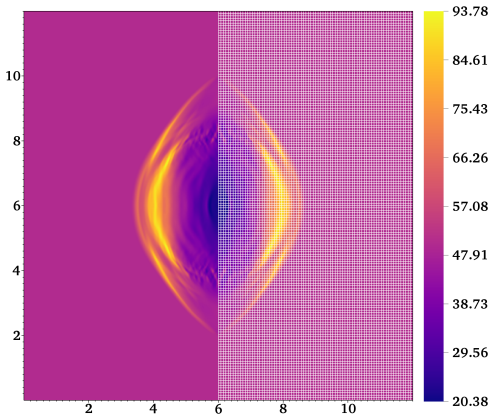

(b) Uniform Grid, $t = 0.12$

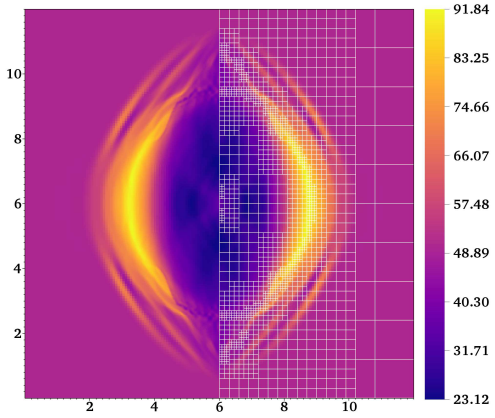

(c) AMR, $t = 0.26$

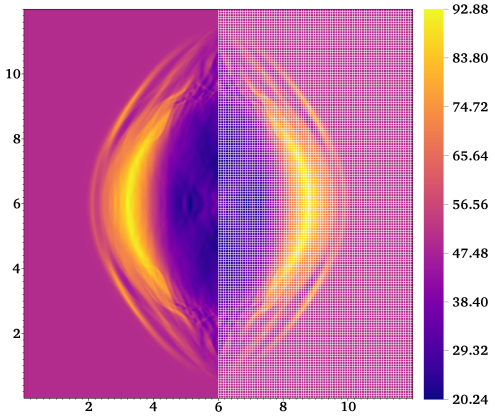

(d) Uniform Grid, $t = 0.26$

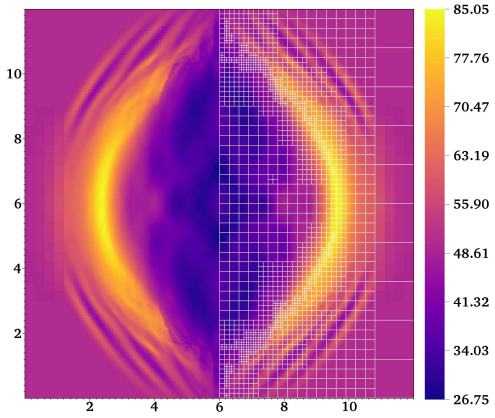

(e) AMR, $t = 0.40$

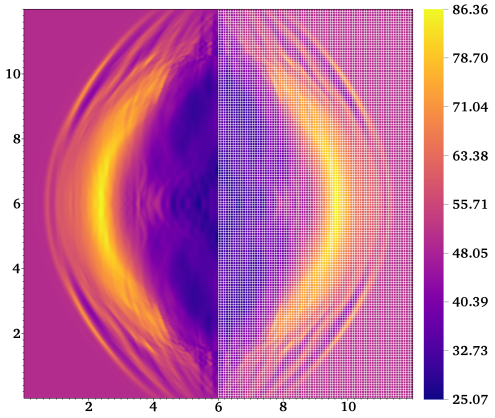

(f) Uniform Grid, $t = 0.40$

Figure 6.23: Magnetic pressure. Comparing the results of the solution with AMR (left column) with the solution on a uniform-grid mesh of 640×640 (right column) at various times shown. Both solutions use a fixed time step and the same CFL number based on the electromagnetic wave propagation speed. The AMR solutions use refinement criteria based on relative gradients of the electron and ion energy densities, with a threshold of 0.5. The mesh is shown on the right side of the domain in each plot, but the mesh resolution is reduced by a factor of $4\times$ to improve clarity.

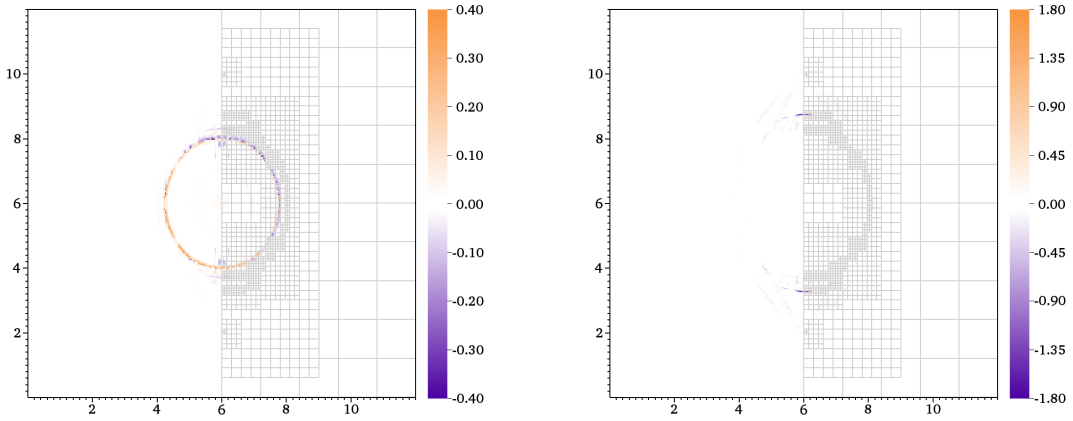

(a) $\frac{\rho_{AMR}-\rho_{Uniform}}{\rho_{AMR}}$, $t = 0.12$ **(b)** $\frac{p_{AMR}-p_{Uniform}}{p_{AMR}}$, $t = 0.12$

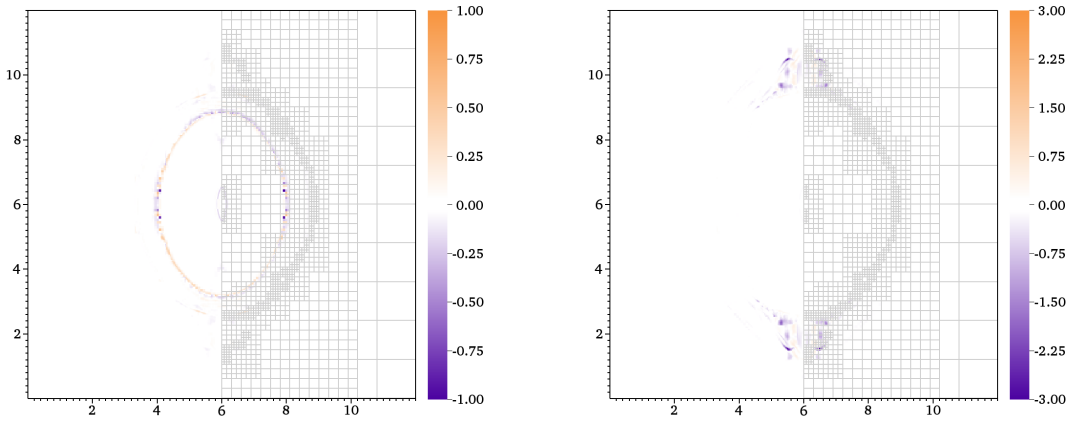

(c) $\frac{\rho_{AMR}-\rho_{Uniform}}{\rho_{AMR}}$, $t = 0.26$ **(d)** $\frac{p_{AMR}-p_{Uniform}}{p_{AMR}}$, $t = 0.26$

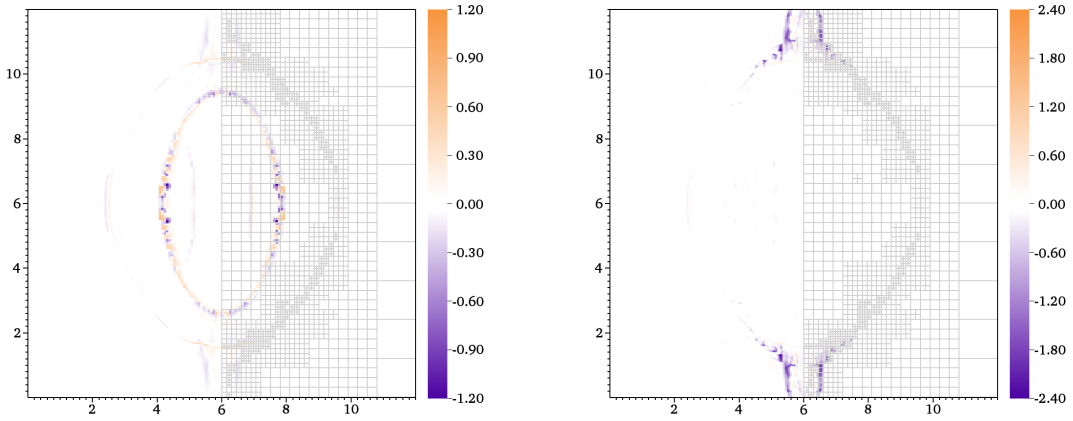

(e) $\frac{\rho_{AMR}-\rho_{Uniform}}{\rho_{AMR}}$, $t = 0.40$ **(f)** $\frac{p_{AMR}-p_{Uniform}}{p_{AMR}}$, $t = 0.40$

Figure 6.24: Plots of the relative difference between the solution with AMR and the solution on a uniform-grid, at various times. The left column shows the relative difference in total mass density, and the relative difference in total fluid pressure is plotted on the right. Both solutions use a fixed time step and the same CFL number. The AMR solutions use refinement criteria based on relative gradients of the electron and ion energy densities, with a threshold of 0.5. The AMR mesh is shown on the right side of the domain in each plot, but the mesh resolution is reduced by a factor of $4\times$ to improve clarity.

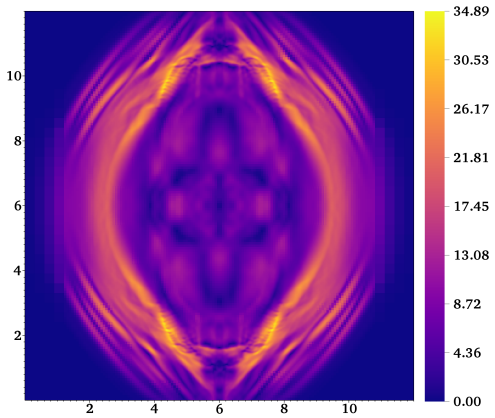

(a) Electric Field, $|\vec{E}|$

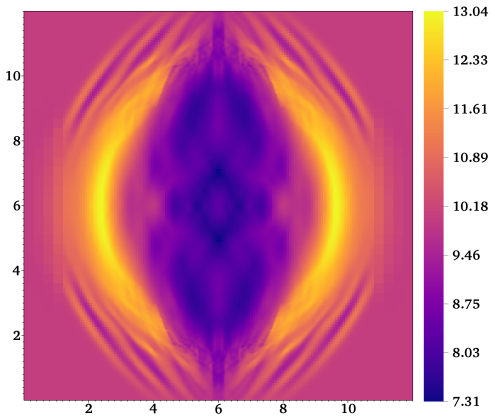

(b) Magnetic Field, $|\vec{B}|$

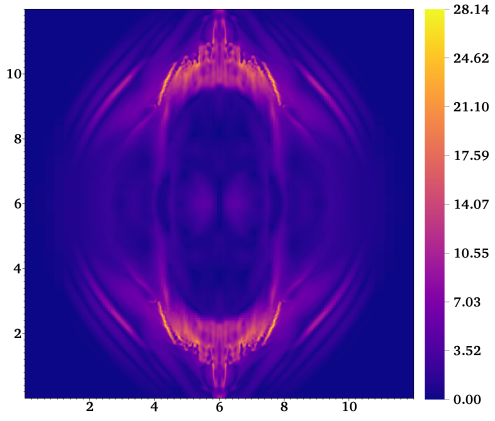

(c) Electric Current Density, $|\vec{j}|$

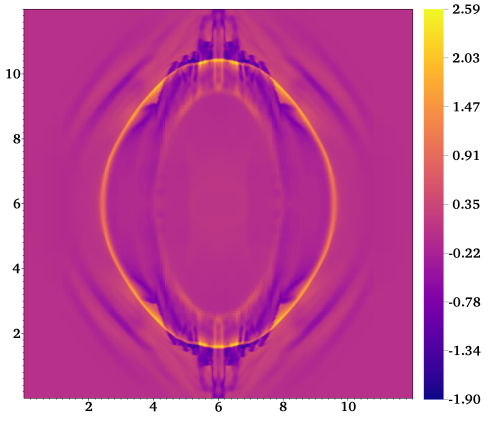

(d) Electric Charge Density, ρ_q

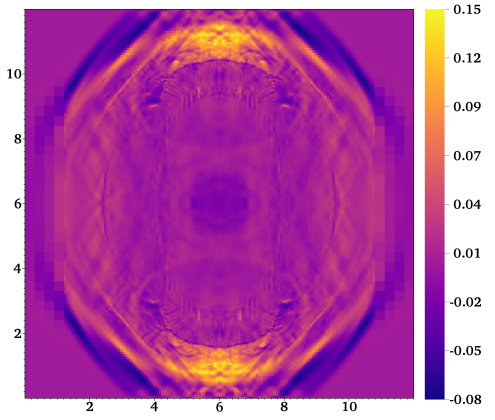

(e) Divergence Correction, Φ

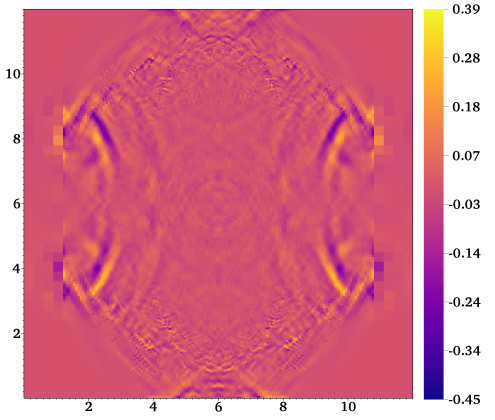

(f) Divergence Correction, Ψ

Figure 6.25: Plots of various electromagnetic parameters from the solution at $t = 0.4$ with AMR.

Chapter 7

Conclusions and Future Work

7.1 Conclusions

This work presents the development of a higher-order, multi-fluid plasma model that is solution-adaptive in both space and time. A number of solution-stabilizing methods are studied and characterized, and the algorithm is demonstrated to be robust at handling the types of strong discontinuities and oscillations common in plasmas. One of the defining advantages of the multi-fluid plasma model over traditional, single-fluid, MHD methods is the ability of the multi-fluid model to resolve high-frequency waves and the accompanying vast ranges in temporal and length scales found in real plasmas. Multiple demonstrations of this effect are provided, including the magnetic shock tube example and a 2D plasma explosion problem. The thermophysical material models for both transport and thermodynamic properties have been extended to include monotonic extrapolations for ultra-high temperature regimes which are beyond the temperature ranges in common fluid properties tables. An HLLC-type Riemann solver is integrated for the electromagnetic equations to resolve the discontinuities at the cell faces, including boundary faces, and compute the flux.

The algorithm has been demonstrated to be 4th-order accurate in both space and time for smooth solutions. We have verified the order of accuracy and validated the code using 2D transmagnetic wave, 3D plane-polarized wave, and electron acoustic wave test cases, all of which have exact solutions. The multi-fluid plasma algorithm in Chord was also used to solve classic test problems in plasma physics, a Brio-Wu style magnetic shock tube and the GEM Challenge magnetic reconnection problem. We have employed AMR to enable high-resolution, accurate solutions with a demonstrated improvement in computational efficiency. In the magnetic shock tube problem, the utilization of AMR leads to a 70% reduction in compute time, and in the plasma explosion case, AMR reduces the solution time by 90%.

7.2 Original Contributions

This research has resulted in novel contributions to the field of plasma modeling, namely:

- Established a multi-fluid plasma solver in a fourth-order, finite-volume numerical framework.
- Combined a fourth-order, finite-volume method using the PPM limiter and AMR to solve Maxwell's equations.
- Integrated a multi-fluid plasma model with AMR, and an investigation of AMR settings and performance improvements from AMR have been characterized for common plasma test problems.
- Tested solution-stabilizing methods when applying the fourth-order, multi-fluid plasma modeling algorithm to problems involving under-resolved gradients, shocks, and other strong discontinuities.
- Applied the new multi-fluid plasma modeling algorithm to solve challenging problems; for example, the GEM magnetic reconnection challenge problem, a magnetic shock tube, and a plasma blast problem.

7.3 Future Work

For most of the current work, a reduced version of our full, multi-fluid plasma model is uesd; the model has been simplified to handle more basic, two-fluid, fully-ionized, collision-less plasmas. An obvious next step in this research will be to apply our model to more complex plasmas and include collision mechanisms between the various species. This will open the door for many applications and allow us to compare simulations in Chord with experimental results from real plasmas. To enable the solution of practical problems, more advanced boundary conditions and mesh handling capabilities should be explored. Chord has the ability to handle mapped structured grids to accommodate complex geometries, but this functionality is not yet implemented for the electromagnetics module. Furthermore, it is very compelling to compile the multi-fluid algorithm

in Chord in an optimized, production type environment and perform very large, highly parallelized simulations to better understand the scaling performance.

Bibliography

[1] *Plasma Science: Advancing Knowledge in the National Interest*. National Academies Press, Washington, D.C., December 2007. ISBN 9780309109437. URL http://www.nap.edu/catalog/11960.

[2] H. Alfvén. Existence of Electromagnetic-Hydrodynamic Waves. *Nature*, 150(3805):405–406, October 1942. ISSN 0028-0836, 1476-4687. doi: 10.1038/150405d0. URL https://www.nature.com/articles/150405d0.

[3] J. Birn, J. F. Drake, M. A. Shay, B. N. Rogers, R. E. Denton, M. Hesse, M. Kuznetsova, Z. W. Ma, A. Bhattacharjee, A. Otto, and P. L. Pritchett. Geospace Environmental Modeling (GEM) Magnetic Reconnection Challenge. *Journal of Geophysical Research: Space Physics*, 106(A3):3715–3719, March 2001. ISSN 01480227. doi: 10.1029/1999JA900449. URL https://onlinelibrary.wiley.com/doi/10.1029/1999JA900449.

[4] Phillip Colella, Milo R Dorr, and Daniel D Wake. Numerical solution of plasma fluid equations using locally refined grids. *Journal of Computational Physics*, 152(2):550–583, July 1999. ISSN 0021-9991. doi: 10.1006/jcph.1999.6245. URL http://www.sciencedirect.com/science/article/pii/S0021999199962459.

[5] C. P. T. Groth, D. L. De Zeeuw, T. I. Gombosi, and K. G. Powell. A Parallel Adaptive 3D MHD Scheme for Modeling Coronal and Solar Wind Plasma Flows. *Space Science Reviews*, 87(1/2):193–198, 1999. ISSN 00386308. doi: 10.1023/A:1005136115563. URL http://link.springer.com/10.1023/A:1005136115563.

[6] Clinton P. T. Groth, Darren L. De Zeeuw, Tamas I. Gombosi, and Kenneth G. Powell. Global three-dimensional MHD simulation of a space weather event: CME formation, interplanetary propagation, and interaction with the magnetosphere. *Journal of Geophysical Research: Space Physics*, 105(A11):25053–25078, November 2000. ISSN 01480227. doi: 10.1029/2000JA900093. URL http://doi.wiley.com/10.1029/2000JA900093.

[7] T.I. Gombosi, D.L. DeZeeuw, C.P.T. Groth, and K.G. Powell. Magnetospheric configuration for Parker-spiral IMF conditions: Results of a 3D AMR MHD simulation. *Advances in Space Research*, 26(1):139–149, January 2000. ISSN 02731177. doi: 10.1016/S0273-1177(99)01040-6. URL https://linkinghub.elsevier.com/retrieve/pii/S0273117799010406.

[8] Dinshaw S. Balsara. Divergence-Free Adaptive Mesh Refinement for Magnetohydrodynamics. *Journal of Computational Physics*, 174(2):614–648, December 2001. ISSN 00219991. doi: 10.1006/jcph.2001.6917. URL https://linkinghub.elsevier.com/retrieve/pii/S0021999101969177.

[9] S. Fromang, P. Hennebelle, and R. Teyssier. A high order Godunov scheme with constrained transport and adaptive mesh refinement for astrophysical magnetohydrodynamics. *Astronomy & Astrophysics*, 457(2):371–384, October 2006. ISSN 0004-6361, 1432-0746. doi: 10.1051/0004-6361:20065371. URL http://www.aanda.org/10.1051/0004-6361:20065371.

[10] I. A. Kryukov, S. N. Borovikov, N. V. Pogorelov, and G. P. Zank. A New, Three-dimensional, Adaptive Mesh Refinement Code for Modeling Flows of Partially Ionized Plasma. In N. V. Pogorelov, E. Audit, and G. P. Zank, editors, *Numerical Modeling of Space Plasma Flows*, volume 385 of *Astronomical Society of the Pacific Conference Series*, page 265. Astronomical Society of the Pacific Conference Series, April 2008.

[11] J. H. Malmberg and J. S. deGrassie. Properties of Nonneutral Plasma. *Physical Review Letters*, 35(9):577–580, September 1975. ISSN 0031-9007. doi: 10.1103/PhysRevLett.35.577.

[12] H. Alfvén. Existence of Electromagnetic-Hydrodynamic Waves. *Nature*, 150(3805):405–406, October 1942. ISSN 0028-0836, 1476-4687. doi: 10.1038/150405d0. URL http://www.nature.com/articles/150405d0.

[13] J. P. Freidberg. Ideal magnetohydrodynamic theory of magnetic fusion systems. *Reviews of Modern Physics*, 54(3):801–902, July 1982. ISSN 0034-6861. doi: 10.1103/RevModPhys.54.801. URL https://link.aps.org/doi/10.1103/RevModPhys.54.801.

[14] W. Park, E. V. Belova, G. Y. Fu, X. Z. Tang, H. R. Strauss, and L. E. Sugiyama. Plasma simulation studies using multilevel physics models. *Physics of Plasmas*, 6(5):1796–1803, May 1999. ISSN 1070-664X, 1089-7674. doi: 10.1063/1.873437.

[15] Eric C. D'Avignon, Philip J. Morrison, and Manasvi Lingam. Derivation of the Hall and extended magnetohydrodynamics brackets. *Physics of Plasmas*, 23(6):062101, June 2016. ISSN 1070-664X, 1089-7674. doi: 10.1063/1.4952641.

[16] E. A. Witalis. Hall Magnetohydrodynamics and Its Applications to Laboratory and Cosmic Plasma. *IEEE Transactions on Plasma Science*, 14(6):842–848, 1986. ISSN 0093-3813. doi: 10.1109/TPS.1986.4316632.

[17] Mark J. Kushner. Hybrid modelling of low temperature plasmas for fundamental investigations and equipment design. *Journal of Physics D: Applied Physics*, 42(19):194013, 2009. ISSN 0022-3727. doi: 10.1088/0022-3727/42/19/194013. URL http://stacks.iop.org/0022-3727/42/i=19/a=194013.

[18] U. Shumlak and J. Loverich. Approximate Riemann solver for the two-fluid plasma model. *Journal of Computational Physics*, 187(2):620–638, May 2003. ISSN 00219991. doi: 10.1016/S0021-9991(03)00151-7. URL https://linkinghub.elsevier.com/retrieve/pii/S0021999103001517.

[19] John Loverich, Ammar Hakim, and Uri Shumlak. A Discontinuous Galerkin Method for Ideal Two-Fluid Plasma Equations. *Communications in Computational Physics*, 9(2):240–268, February 2011. ISSN 1815-2406, 1991-7120. doi: 10.4208/cicp.250509.210610a. URL http://arxiv.org/abs/1003.4542. arXiv: 1003.4542.

[20] A. Hakim, J. Loverich, and U. Shumlak. A high resolution wave propagation scheme for ideal Two-Fluid plasma equations. *Journal of Computational Physics*, 219(1):418–442, November 2006. ISSN 00219991. doi: 10.1016/j.jcp.2006.03.036. URL https://linkinghub.elsevier.com/retrieve/pii/S0021999106001707.

[21] Remi Abgrall and Harish Kumar. Robust Finite Volume Schemes for Two-Fluid Plasma Equations. *Journal of Scientific Computing*, 60(3):584–611, September 2014. ISSN 0885-7474, 1573-7691. doi: 10.1007/s10915-013-9809-6. URL http://link.springer.com/10.1007/s10915-013-9809-6.

[22] Dinshaw S. Balsara, Takanobu Amano, Sudip Garain, and Jinho Kim. A high-order relativistic two-fluid electrodynamic scheme with consistent reconstruction of electromagnetic fields and a multidimensional riemann solver for electromagnetism. *Journal of Computational Physics*, 318:169–200, aug 2016. doi: 10.1016/j.jcp.2016.05.006. URL https://doi.org/10.1016/j.jcp.2016.05.006.

[23] Zhenguang Huang, Gábor Tóth, Bart van der Holst, Yuxi Chen, and Tamas Gombosi. A six-moment multi-fluid plasma model. *Journal of Computational Physics*, 387:134–153, June 2019. ISSN 00219991. doi: 10.1016/j.jcp.2019.02.023. URL https://linkinghub.elsevier.com/retrieve/pii/S0021999119301408.

[24] D. Ghosh, T.D. Chapman, R.L. Berger, A. Dimits, and J.W. Banks. A multispecies, multifluid model for laser–induced counterstreaming plasma simulations. *Computers & Fluids*, 186:38–57, May 2019. ISSN 00457930. doi: 10.1016/j.compfluid.2019.04.012. URL https://linkinghub.elsevier.com/retrieve/pii/S0045793019301227.

[25] X. Gao, S. M. J. Guzik, and P. Colella. A fourth-order boundary treatment for viscous fluxes on cartesian grid finite-volume methods. AIAA 2014-1277, 52nd AIAA Aerospace Sciences Meeting, 2014.

[26] X Gao and S. M. J. Guzik. A fourth-order scheme for the compressible Navier-Stokes equations. AIAA 2015-0298, 53rd AIAA Aerospace Sciences Meeting, 2015.

[27] S. M. Guzik, X. Gao, L. D. Owen, P. McCorquodale, and P. Colella. A freestream-preserving fourth-order finite-volume method in mapped coordinates with adaptive-mesh refinement. *Computers and Fluids*, 123:202–217, 2015.

[28] S. M. Guzik, X. Gao, and C. Olschanowsky. A high-performance finite-volume algorithm for solving partial differential equations governing compressible viscous flows on structured grids. *Computers and Mathematics with Applications*, 72:2098–2118, 2016.

[29] X. Gao, L. D. Owen, and S. M. J. Guzik. A parallel adaptive numerical method with generalized curvilinear coordinate transformation for compressible Navier-Stokes equations. *International Journal for Numerical Methods in Fluids*, 82:664–688, 2016.

[30] X. Gao, L. D. Owen, and S. M. Guzik. A high-order finite-volume method for combustion. AIAA 2016-1808, 54th AIAA Aerospace Sciences Meeting, 2016.

[31] Francis F. Chen. *Introduction to Plasma Physics and Controlled Fusion Third Edition*. Springer, third edition, 2016.

[32] M. A. Lieberman and Allan J. Lichtenberg. *Principles of plasma discharges and materials processing*. Wiley-Interscience, Hoboken, N.J, 2nd ed edition, 2005. ISBN 978-0-471-72001-0. OCLC: ocm56752658.

[33] U. Shumlak, R. Lilly, N. Reddell, E. Sousa, and B. Srinivasan. Advanced physics calculations using a multi-fluid plasma model. *Computer Physics Communications*, 182(9): 1767–1770, September 2011. ISSN 0010-4655. doi: 10.1016/j.cpc.2010.12.048. URL http://www.sciencedirect.com/science/article/pii/S001046551100004X.

[34] E.M. Sousa and U. Shumlak. A blended continuous-discontinuous finite element method for solving the multi-fluid plasma model. *Journal of Computational Physics*, 326:56–75, December 2016. ISSN 00219991. doi: 10.1016/j.jcp.2016.08.044. URL http://linkinghub.elsevier.com/retrieve/pii/S0021999116304016.

[35] C.-D. Munz, P. Omnes, and R. Schneider. A godunov-type solver for the maxwell equations with divergence cleaning. In E. F. Toro, editor, *Godunov Methods*, pages 647–654. Springer US, 2001. ISBN 978-1-4613-5183-2 978-1-4615-0663-8. doi: 10.1007/978-1-4615-0663-8_64. URL http://link.springer.com/chapter/10.1007/978-1-4615-0663-8_64.

[36] C.-D. Munz, P. Ommes, and R. Schneider. A three-dimensional finite-volume solver for the maxwell equations with divergence cleaning on unstructured meshes. *Computer Physics Communications*, 130(1-2):83–117, July 2000. ISSN 00104655. doi: 10.1016/S0010-4655(00)00045-X. URL http://linkinghub.elsevier.com/retrieve/pii/S001046550000045X.

[37] C.-D. Munz, P. Omnes, R. Schneider, E. Sonnendrücker, and U. Voß. Divergence correction techniques for maxwell solvers based on a hyperbolic model. *Journal of Computational Physics*, 161(2):484–511, July 2000. ISSN 00219991. doi: 10.1006/jcph.2000.6507. URL http://linkinghub.elsevier.com/retrieve/pii/S0021999100965070.

[38] Su Yan and Jian-Ming Jin. A continuity-preserving and divergence-cleaning algorithm based on purely and damped hyperbolic maxwell equations in inhomogeneous media. *Journal of Computational Physics*, 334:392–418, apr 2017. doi: 10.1016/j.jcp.2017.01.012. URL https://doi.org/10.1016/j.jcp.2017.01.012.

[39] P. L. Bhatnagar, E. P. Gross, and M. Krook. A model for collision processes in gases. i. small amplitude processes in charged and neutral one-component systems. *Physical Review*, 94(3):511–525, May 1954. doi: 10.1103/PhysRev.94.511. URL http://link.aps.org/doi/10.1103/PhysRev.94.511.

[40] K. S. Yee and J. S. Chen. The finite-difference time-domain (fdtd) and the finite-volume time-domain (fvtd) methods in solving maxwell's equations. *IEEE Transactions on Antennas and Propagation*, 45(3):354–363, Mar 1997. ISSN 0018-926X. doi: 10.1109/8.558651.

[41] A. Mignone and G. Bodo. An hllc riemann solver for relativistic flows - ii. magnetohydrodynamics. *Monthly Notices of the Royal Astronomical Society*, 368(3):1040–1054, 2006. doi: 10.1111/j.1365-2966.2006.10162.x. URL http://dx.doi.org/10.1111/j.1365-2966.2006.10162.x.

[42] P. McCorquodale and P. Colella. A high-order finite-volume method for conservation laws on locally refined grids. *Communications in Applied Mathematics and Computational Science*, 6(1):1–25, 2011.

[43] E. F. Toro, M. Spruce, and W. Speares. Restoration of the contact surface in the HLL-Riemann solver. *Shock Waves*, 4(1):25–34, July 1994. ISSN 0938-1287, 1432-2153. doi: 10.1007/BF01414629. URL http://link.springer.com/10.1007/BF01414629.

[44] A. Mignone and G. Bodo. An hllc riemann solver for relativistic flows - i. hydrodynamics. *Monthly Notices of the Royal Astronomical Society*, 364(1):126–136, 2005. doi: 10.1111/j.1365-2966.2005.09546.x. URL http://dx.doi.org/10.1111/j.1365-2966.2005.09546.x.

[45] S Miranda-Aranguren, M A Aloy, and T Rembiasz. An HLLC riemann solver for resistive relativistic magnetohydrodynamics. *Monthly Notices of the Royal Astronomical Society*, 476 (3):3837–3860, feb 2018. doi: 10.1093/mnras/sty419. URL https://doi.org/10.1093/mnras/sty419.

[46] P. Colella, D. T. Graves, N.D. Keen, T. J. Ligocki, D. F. Martin, P.W. McCorquodale, D. Modiano, P.O. Schwartz, T.D. Sternberg, and B. Van Straalen. *Chombo Software Package for AMR Applications - Design Document*. Lawrence Berkeley National Laboratory, 2009. `https://seesar.lbl.gov/anag/chombo/ChomboDesign-3.0.pdf`.

[47] J.J Gottlieb and C.P.T Groth. Assessment of riemann solvers for unsteady one-dimensional inviscid flows of perfect gases. *Journal of Computational Physics*, 78(2):437–458, October 1988. ISSN 00219991. doi: 10.1016/0021-9991(88)90059-9. URL https://linkinghub.elsevier.com/retrieve/pii/0021999188900599.

[48] M. Adams, P. Colella, D. T. Graves, J. N. Johnson, N. D. Keen, T. J. Ligocki, D. F. Martin, P. W. McCorquodale, D. Modiano, P. O. Schwartz, T. D. Sternberg, and B. Van Straalen. Chombo software package for amr applications - design document. Lawrence Berkeley Na-

tional Laboratory Technical Report LBNL-6616E, Lawrence Berkeley National Laboratory, December 2015. URL http://crd.lbl.gov/assets/pubs_presos/chomboDesign.pdf.

[49] M. J. Berger and P. Colella. Local adaptive mesh refinement for shock hydrodynamics. *J. Comput. Phys.*, 82(1):64–84, May 1989.

[50] Joshua Christopher, Stephen M. Guzik, and Xinfeng Gao. High-order implicit-explicit additive runge-kutta schemes for numerical combustion with adaptive mesh refinement. *International Journal for Numerical Methods in Fluids*, 2022. doi: https://doi.org/10.1002/fld.5084. URL https://onlinelibrary.wiley.com/doi/abs/10.1002/fld.5084.

[51] L. D. Owen, S. M. Guzik, and X. Gao. A fourth-order finite-volume algorithm for compressible flow with chemical reactions on mapped grids. In *23rd AIAA Computational Fluid Dynamics Conference*. AIAA Aviation Forum, 2017. AIAA 2017-4498.

[52] L. D. Owen, X. Gao, and S. M. Guzik. Techniques for improving monotonicity in a fourth-order finite-volume algorithm solving shocks and detonations. *Journal of Computational Physics*, 415, 2020.

[53] N. Overton-Katz, H. Johansen, X. Gao, and S. M. Guzik. Adaptive clipping-and-redistribution algorithms for bounded and conservative high-order interpolations applied to discontinuous and reactive flows. Accepted for publication, 2022.

[54] P. Colella and M. Sekora. A limiter for PPM that preserves accuracy at smooth extrema. *J. Comput. Phys.*, 227(15):7069–7076, 2008.

[55] E. G. Broadbent. One-dimensional acoustic wave propagation in a plasma fluid in the near field of an electrical disturbance. *Proceedings of the Royal Society of London. Series A, Mathematical and Physical Sciences*, 311(1505):211–243, 1969. ISSN 00804630. URL http://www.jstor.org/stable/2416317.

[56] Eleuterio F. Toro. *Riemann Solvers and Numerical Methods for Fluid Dynamics*. Springer-Verlag Berlin Heidelberg, 3 edition, 2009. URL //www.springer.com/us/book/9783540252023.

[57] Ciprian Dumitrache. *Novel Laser Ignition Technique Using Dual-Pulse Pre-Ionization*. Dissertation, Colorado State University, 2017.

[58] S. Gordon and B. J. McBride. Computer program for calculation of complex chemical equilibrium compositions, rocket performance, incident and reflective shocks, and chapman-jouget detonations. Reference Publication 1311, NASA, 1994.

[59] Jerrold M. Yos. Transport Properties of Nitrogen, Hydrogen, Oxygen, and Air to 30,000 K. Technical Memorandum RAD-TM-63-7, Research and Advanced Development Division, AVCO Corporation, Wilmington, Massachusetts, March 1963.

[60] M. Kono, K. Niu, T. Tsukamoto, and Y. Ujiie. Mechanism of flame kernel formation produced by short duration sparks. *Symp. Combust.*, 22:1643–1649, 1988.

[61] Dinshaw S. Balsara, Allen Taflove, Sudip Garain, and Gino Montecinos. Computational electrodynamics in material media with constraint-preservation, multidimensional riemann solvers and sub-cell resolution – part i, second-order FVTD schemes. *Journal of Computational Physics*, 349:604–635, nov 2017. doi: 10.1016/j.jcp.2017.07.024. URL https://doi.org/10.1016/j.jcp.2017.07.024.

[62] M Brio and C.C Wu. An upwind differencing scheme for the equations of ideal magnetohydrodynamics. *Journal of Computational Physics*, 75(2):400–422, April 1988. ISSN 00219991. doi: 10.1016/0021-9991(88)90120-9. URL https://linkinghub.elsevier.com/retrieve/pii/0021999188901209.

[63] Dinshaw S. Balsara, Takanobu Amano, Sudip Garain, and Jinho Kim. A high-order relativistic two-fluid electrodynamic scheme with consistent reconstruction of electromagnetic fields and a multidimensional Riemann solver for electromagnetism. *Journal of Computational Physics*,

318:169–200, August 2016. ISSN 00219991. doi: 10.1016/j.jcp.2016.05.006. URL https://linkinghub.elsevier.com/retrieve/pii/S0021999116301334.

[64] S. Polak and X. Gao. Fourth-order accurate numerical modeling of the multi-fluid plasma equations with adaptive mesh refinement. *Journal of Computational Physics*, 2022. In review for publication.

[65] M. A. Potter, P. K. Browning, and M. Gordovskyy. Forced magnetic reconnection and plasmoid coalescence: I. Magnetohydrodynamic simulations. *Astronomy & Astrophysics*, 623: A15, March 2019. ISSN 0004-6361, 1432-0746. doi: 10.1051/0004-6361/201833565. URL https://www.aanda.org/10.1051/0004-6361/201833565.

[66] A. Alvarez Laguna, N. Ozak, A. Lani, H. Deconinck, and S. Poedts. Fully-implicit finite volume method for the ideal two-fluid plasma model. *Computer Physics Communications*, 231:31–44, October 2018. ISSN 00104655. doi: 10.1016/j.cpc.2018.05.006. URL https://linkinghub.elsevier.com/retrieve/pii/S0010465518301590.

[67] Andrew L. Zachary, Andrea Malagoli, and Phillip Colella. A Higher-Order Godunov Method for Multidimensional Ideal Magnetohydrodynamics. *SIAM Journal on Scientific Computing*, 15(2):263–284, March 1994. ISSN 1064-8275, 1095-7197. doi: 10.1137/0915019. URL http://epubs.siam.org/doi/10.1137/0915019.

Appendix A

Numerical Algorithm Data Structure

To reiterate the description of the data structure formation from Chapter 3, when the electromagnetic physics are solved-of, the length of the solution vector is the same regardless of the number of spatial dimensions modeled. This treatment is used because of the cross-product operations in the momentum equation (2.2) and Maxwell's equations (2.12) and (2.14) reference perpendicular vector components. In three dimensions, flux is computed in each direction, x, y, and z. In two dimensions, flux is only computed in the x and y directions; the z-components of the vector-based solution terms may still evolve due to influence from their source terms, but there is no flux computed in the z-direction. Finally, in one dimension, flux is computed in the x direction only, and the y and z components of the vector based solution terms are influenced only by their source terms.

A.1 Conservation Equation Terms, Multi-Fluid Plasma Model

Conserved solution terms for fluid species α, where $\alpha = 1 \ldots N$:

$$\mathbf{U} = \begin{bmatrix} \rho_\alpha \\ \rho_\alpha u_{\alpha\, x} \\ \rho_\alpha u_{\alpha\, y} \\ \rho_\alpha u_{\alpha\, z} \\ \rho_\alpha e_\alpha \\ \vdots \\ E_x \\ E_y \\ E_z \\ \Psi \\ B_x \\ B_y \\ B_z \\ \Phi \end{bmatrix} \tag{A.1}$$

Hyperbolic flux dyad for fluid species α, where $\alpha = 1 \ldots N$:

$$\vec{\mathbf{F}} = \left[\begin{bmatrix} \rho_\alpha u_{\alpha\,x} \\ \rho_\alpha u_{\alpha\,x}^2 + p_\alpha \\ \rho_\alpha u_{\alpha\,x} u_{\alpha\,y} \\ \rho_\alpha u_{\alpha\,x} u_{\alpha\,z} \\ \left(e_1 + \frac{p_\alpha}{\rho_\alpha}\right) \rho_\alpha u_{\alpha\,x} \\ \vdots \\ \frac{\chi_E\,\Phi}{\epsilon_0\,\mu_0} \\ \frac{B_z}{\epsilon_0\,\mu_0} \\ -\frac{B_y}{\epsilon_0\,\mu_0} \\ \frac{\chi_B\,B_x}{\epsilon_0\,\mu_0} \\ \chi_B\,\Psi \\ -E_z \\ E_y \\ \chi_E\,E_x \end{bmatrix}, \begin{bmatrix} \rho_\alpha u_{\alpha\,y} \\ \rho_\alpha u_{\alpha\,x} u_{\alpha\,y} \\ \rho_\alpha u_{\alpha\,y}^2 + p_\alpha \\ \rho_\alpha u_{\alpha\,y} u_{\alpha\,z} \\ \left(e_1 + \frac{p_\alpha}{\rho_\alpha}\right) \rho_\alpha u_{\alpha\,y} \\ \vdots \\ -\frac{B_z}{\epsilon_0\,\mu_0} \\ \frac{\chi_E\,\Phi}{\epsilon_0\,\mu_0} \\ \frac{B_x}{\epsilon_0\,\mu_0} \\ \frac{\chi_B\,B_y}{\epsilon_0\,\mu_0} \\ E_z \\ \chi_B\,\Psi \\ -E_x \\ \chi_E\,E_y \end{bmatrix}, \begin{bmatrix} \rho_\alpha u_{\alpha\,z} \\ \rho_\alpha u_{\alpha\,x} u_{\alpha\,z} \\ \rho_\alpha u_{\alpha\,y} u_{\alpha\,z} \\ \rho_\alpha u_{\alpha\,z}^2 + p_\alpha \\ \left(e_1 + \frac{p_\alpha}{\rho_\alpha}\right) \rho_\alpha u_{\alpha\,z} \\ \vdots \\ \frac{B_y}{\epsilon_0\,\mu_0} \\ -\frac{B_x}{\epsilon_0\,\mu_0} \\ \frac{\chi_E\,\Phi}{\epsilon_0\,\mu_0} \\ \frac{\chi_B\,B_z}{\epsilon_0\,\mu_0} \\ -E_y \\ E_x \\ \chi_B\,\Psi \\ \chi_E\,E_z \end{bmatrix} \right]. \quad \text{(A.2)}$$

The viscous (elliptical) flux dyad, for fluid species α, where $\alpha = 1 \ldots N$:

$$\vec{\mathbf{G}} = \left[\begin{bmatrix} 0 \\ \tau_{\alpha_{xx}} \\ \tau_{\alpha_{xy}} \\ \tau_{\alpha_{xz}} \\ \vec{u_\alpha} \cdot \vec{\tau_{\alpha_x}} - \phi_{\alpha_x} \\ \vdots \\ 0 \\ 0 \\ 0 \\ 0 \\ 0 \\ 0 \\ 0 \\ 0 \end{bmatrix}, \begin{bmatrix} 0 \\ \tau_{\alpha_{yx}} \\ \tau_{\alpha_{yy}} \\ \tau_{\alpha_{yz}} \\ \vec{u_\alpha} \cdot \vec{\tau_{\alpha_y}} - \phi_{\alpha_y} \\ \vdots \\ 0 \\ 0 \\ 0 \\ 0 \\ 0 \\ 0 \\ 0 \\ 0 \end{bmatrix}, \begin{bmatrix} 0 \\ \tau_{\alpha_{zx}} \\ \tau_{\alpha_{zy}} \\ \tau_{\alpha_{zz}} \\ \vec{u_\alpha} \cdot \vec{\tau_{\alpha_z}} - \phi_{\alpha_z} \\ \vdots \\ 0 \\ 0 \\ 0 \\ 0 \\ 0 \\ 0 \\ 0 \\ 0 \end{bmatrix} \right]. \tag{A.3}$$

Source terms for fluid species α, where $\alpha = 1 \ldots N$:

$$\mathbf{S} = \begin{bmatrix} \left(\frac{\partial \rho_\alpha}{\partial t}\right)_c \\ q_\alpha \frac{\rho_\alpha}{m_\alpha} \left(E_x + B_z u_{\alpha\, y} - B_y u_{\alpha\, z}\right) - \sum_\beta R_{\alpha\beta_x} + \left(\frac{\partial \rho_\alpha u_{\alpha\, x}}{\partial t}\right)_c \\ q_\alpha \frac{\rho_\alpha}{m_\alpha} \left(E_y + B_x u_{\alpha\, z} - B_z u_{\alpha\, x}\right) - \sum_\beta R_{\alpha\beta_y} + \left(\frac{\partial \rho_\alpha u_{\alpha\, y}}{\partial t}\right)_c \\ q_\alpha \frac{\rho_\alpha}{m_\alpha} \left(E_z + B_y u_{\alpha\, x} - B_x u_{\alpha\, y}\right) - \sum_\beta R_{\alpha\beta_z} + \left(\frac{\partial \rho_\alpha u_{\alpha\, z}}{\partial t}\right)_c \\ q_\alpha \frac{\rho_\alpha}{m_\alpha} \left(\vec{u}_\alpha \cdot \vec{E}\right) + m_\alpha \vec{u_\alpha} \sum_\beta \vec{R}_{\alpha\beta} + \left(\frac{\partial \rho_\alpha e_\alpha}{\partial t}\right)_c \\ \vdots \\ \frac{-1}{\epsilon_0} \sum_\alpha q_\alpha j_{\alpha_x} \\ \frac{-1}{\epsilon_0} \sum_\alpha q_\alpha j_{\alpha_y} \\ \frac{-1}{\epsilon_0} \sum_\alpha q_\alpha j_{\alpha_z} \\ 0 \\ 0 \\ 0 \\ 0 \\ \frac{\chi_E}{\epsilon_0} \sum_\alpha q_\alpha n_\alpha \end{bmatrix}. \tag{A.4}$$